David Tumpold

Modeling and Optimization Methods of an Electrostatically driven MEMS Speaker

DISSERTATION

To obtain the Academic Degree

Doctor of Technical Sciences

Vienna University of Technology

Institute of Mechanics and Mechatronics

Measurement and Actuator Division

1st Assesor:
Univ.Prof. Dipl.-Ing. Dr.techn. Manfred Kaltenbacher
Institute of Mechanics and Mechatronics
Technical University of Vienna

2nd Assesor:
Univ.Prof. Dipl.-Phys. Dr.rer.nat. Ulrich Schmid
Institute of Sensor and Actuator Systems
Technical University of Vienna

Janurary/2014

Acknowledgements

I would like to thank my thesis advisor Univ.-Prof. Dr. techn. Dr.-Ing. Habil Manfred Kaltenbacher for his continuous help and assistance.

I also want to express my thanks to all colleagues at the **Vienna University of Technology** at the **department of Mechanics and Mechatronics** for their great support while working on my thesis. Particularly, I want to thank Klaus Bergkirchner, Paul Finsterwalder and Manfred Neumann for their inputs and help during the development process of the demonstrator hardware. Andreas Hüppe, Stefan Zörner and Hendrik Husstedt for their contributions finding new solving strategies and result interpretations. Dominik Perchtold for his great support in MATLAB. Till Knifka for his expertise in solid mechanics and modal analysis. Many thanks also to all namely not mentioned colleagues for their great time, the pleasant working atmosphere and their contribution to the work. I also appreciate Alfons Dehé, Mohsin Navaz and Christoph Glacer for their industrial support and teamwork at Infineon Munich, as well as Andreas Kenda and Martin Lenzhofer from CTR AG in Villach.

I also want to thank my family for their unconditional support, at any time and any place.

Finally, I would like to thank everybody who was important to the successful realization of this thesis, as well as expressing my apology that I could not mention personally one by one.

"The task is...not so much to see what no one has yet seen; but to think what nobody has yet thought, about that which everybody sees."

Erwin Schrödinger
1887 - 1961

This project has been supported within the COMET - Competence Centers for Excellent Technologies Programs by BMVIT, MBWFJ and the federal provinces of Carinthia and Styria.

Abstract

The market for battery powered devices, such as smart-phones or tablets increases rapidly. The trend goes towards smaller and thinner cases. The main challenge is to decrease the power consumption by coincidently shrinking the device size and increasing the efficiency. Micro-electro-mechanical-systems (MEMS) manufactured of silicon, merge cost effective and space saving features as an energy efficient and innovative product. In this work, reversible operated silicon microphones are modeled and optimized towards sound pressure level and total harmonic distortion. The models are described by coupled partial differential equations and solved by the help of the finite element method. Due to the small dimensions of a single acoustic transducer of approximately one millimeter in diameter and two micrometer in thickness, the loudspeaker is manufactured as an eight bit array. The array arrangement opens up the opportunity to drive the speaker in conventional analog driving mode or apply digital sound reconstruction. Geometric nonlinearities such as large deformation, pre-stress or mechanical contact are reflected in the mechanical model and excited electrostatically. By applying the virtual displacement method, the influence of the insulation layer is mapped to the electrostatic force computation. The electrostatic force interacts with the structural mechanics and the membrane starts to oscillate. The electrostatically actuated membrane is coupled to the acoustic model, where the sound pressure level is computed. The challenge in the acoustic propagation computation is on the one hand, the number of unknowns, which can be minimized by using Mortar FEM (non-conforming grids), and on the other hand, in the reflections caused by the bounds of truncating the propagation region. These reflections are minimized with absorbing boundary conditions or a perfectly matched layer surrounding the propagation region. Acoustic results on the single transducer were computed by the finite element method, where for the full speaker array a specially developed wave field computation software was used based on the Kirchhoff-Helmholtz integral. In addition, two optimization strategies towards increasing the sound pressure level were presented. The first deals with stress-induced self raising of the back plate structure, to increase the volume flow and sound pressure level. The second deals with the digital sound reconstruction, investigating the non-reset, with-reset and latched method.

Kurzfassung

Der Markt an Batterie betriebenen Geräten wie Smartphones oder Tabletts nimmt stark zu. Der Trend geht immer mehr in Richtung schlanker und dünner Gehäuse. Um die Laufzeit dieser Geräte bei gleichbleibender, oder sogar schlankerer, Gehäuseform zu verlängern, ist es wichtig energieeffiziente Bauteile zu verbauen. Silizium gefertigte mikro-elektro-mechanische Systeme (MEMS) verbinden kostengünstige und platzsparende Eigenschaften als energieeffizientes und innovatives Produkt. In dieser Arbeit werden reversibel betriebene Silizium-Mikrophone modelliert und hinsichtlich Schalldruckpegel und Signalqualität optimiert. Die Modelle werden mit Hilfe von gekoppelten partiellen Differentialgleichungen beschrieben und mit der Methode der Finiten Elemente gelöst. Auf Grund der geringen Dimensionen eines Einzelwandlers von zirka einem Millimeter Durchmesser und zwei Mikrometer dicke, werden die Lautsprecher in einem acht Bit Array betrieben. Der Array-Betrieb ermöglicht zusätzlich neben analogen Betriebsmoden, auch Untersuchungen der digitalen Schall-Rekonstruktion. Geometrische Nichtlinearitäten, wie große Verformung, Vorspannungen oder mechanischer Kontakt werden im mechanischen Model abgebildet und elektrostatisch angeregt. Mit Hilfe der virtuellen Verschiebung wird der Einfluss von Isolationsschichten auf den elektrostatischen Kraftbeitrag abgebildet. Die elektrostatisch angeregte Membran resultiert in einer mechanischen Bewegung und koppelt in ein akustisches Model. Die Herausforderung im akustischen Ausbreitungsgebiet liegt einerseits in der Anzahl der Unbekannten, welche durch Anwendung von Mortar FEM (nichtkonforme Gitter) minimiert werden können, und andererseits in den Reflexionen an den Randbereichen der Ausbreitungsregion. Diese Reflexionen werden mit absorbierenden Randbedingungen oder einem zusätzlichem Gebiet mit dämpfenden Eigenschaften minimiert. Für akustische Berechnungen am Einzelwandler, werden die Finite Elemente Methode angewendet, wobei für akustische Berechnungen des gesamten acht Bit Arrays wird ein eigens entwickeltes Wellen-Feld-Berechnungs-Tool, basierend auf dem Kirchhoff-Helmholtz Integral angewendet. Zusätzlich werden zwei Optimierungsstrategien vorgestellt. Die Erste beschäftigt sich mit Stress induzierten Buckeln der Gegenelektrode, was eine flache kostengünstige Fertigung ermöglicht und gleichzeitig den Schalldruck optimiert. Die Zweite beschäftigt sich mit der digitalen Schallerzeugung.

Contents

1 Introduction **1**
- 1.1 Motivation . . . 1
- 1.2 Current Status of Research . . . 2
- 1.3 Thesis Specification . . . 4
- 1.4 Structure of the Thesis . . . 4

2 Electrostatically Actuated MEMS Speaker **7**
- 2.1 MEMS Speaker Modes of Operation . . . 7
  - 2.1.1 Single Ended Driving Principle . . . 7
  - 2.1.2 Push-Pull or Pull-Pull Driving Principle . . . 9
- 2.2 Sound Reconstruction . . . 10
  - 2.2.1 Analog Sound Reconstruction . . . 10
  - 2.2.2 Digital Sound Reconstruction . . . 10
- 2.3 Membrane Movement Characteristics . . . 11
  - 2.3.1 Non-Snap-In Operation Mode . . . 12
  - 2.3.2 Snap-In Operation Mode . . . 14
- 2.4 MEMS Speaker Modeling Chain . . . 16

3 Electrostatic - Mechanical Modeling **19**
- 3.1 Mechanical Basics . . . 19
  - 3.1.1 Stress-Strain Relation . . . 19
  - 3.1.2 Mechanical PDE . . . 21
- 3.2 Nonlinearities . . . 22

3.2.1 Large Deformation . . . 22
3.2.2 Stress Stiffening . . . 26
3.2.3 Contact Case . . . 27
3.3 Nonlinear Finite Element Solver . . . 30
3.3.1 Linear versus Nonlinear Behavior . . . 30
3.3.2 Newton Raphson . . . 32
3.3.3 Arc-Length Method for Snap-In Instabilities . . . 34
3.4 Electrostatic Force Computation . . . 35
3.4.1 Electrostatic Force - Coulomb's Method . . . 36
3.4.2 Electrostatic Force - Virtual Work . . . 38
3.5 Electromechanical Transducer (EMT) Element Model . 42
3.5.1 Transducer Element TRANS126 . . . 42
3.5.2 Implementation and Working Principle . . . 43
3.5.3 The EMT Model . . . 46
3.6 Multi-Field Model . . . 49
3.6.1 Multi-Field Coupling . . . 50
3.6.2 Implementation and Working Principle . . . 51
3.6.3 The Model . . . 54
3.7 Results . . . 56
3.7.1 Analytic vs. EMT vs. Multi-Field Model . . . 56
3.7.2 Snap-In of EMT and Multi-Field Model . . . 59

4 Acoustic Field Modeling 61
4.1 Acoustic Basics . . . 61
4.1.1 Acoustic Wave Equation . . . 63
4.1.2 One Dimensional Example . . . 64
4.2 Mechanical-Acoustic Coupling . . . 65
4.3 Single Speaker Modeling with FEM . . . 67
4.3.1 Mech.-Acou. Interface and Propagation Region . . 68
4.3.2 Open Domain Modeling (ABC/PML) . . . 70
4.4 Speaker Array Modeling with Kirchhoff Helmholtz . . . 79
4.4.1 Huygens Principle of Wave Computation . . . 79
4.4.2 Harmonic Computation with Rayleigh Integrals . . 80
4.4.3 Transient Computations with Rayleigh Integral . . 83
4.5 Wave Field Calculation Tool . . . 84
4.5.1 Input Module . . . 87
4.5.2 Computational Module . . . 89
4.5.3 Output Module . . . 90
4.5.4 WFCT Verification . . . 90
4.5.5 Snap-In and Audio Quality . . . 92

5 Optimization I: Buckling Back Plate 95
5.1 Buckling Back Plate Functional Principle . . . 95
5.1.1 Reduced Stiffness . . . 97
5.2 The Reference System . . . 100
5.2.1 Verification . . . 102
5.3 Parameter Variations and Optimization . . . 104
5.3.1 Parameter Variation Results . . . 106
5.4 Tradeoff between Volume and Stiffness . . . 108
5.5 Multi-Snap-In with Electrostatic Actuation . . . 110
5.6 Theoretical Sound Pressure Level Increase . . . 113

6 Optimization II: Digital Sound Reconstruction 115
6.1 Functional Principle . . . 115
6.1.1 Speaker Array and Bit Grouping . . . 118
6.2 Driving Patterns . . . 119
6.2.1 With Reset . . . 119
6.2.2 Without Reset . . . 124
6.3 DSR Simulation Results . . . 128
6.3.1 Amount Cells Available and Quantification . . . 128
6.3.2 Acceleration Based Speaker System . . . 130
6.4 DSR Optimization Approaches . . . 134
6.4.1 Bit-Pattern Optimization . . . 134
6.4.2 Hybrid Stroke Level Modes: . . . 135
6.4.3 Silence-Set-Reset Mode (SSR): . . . 136
6.5 Digital vs. Analog Measurement . . . 137

7 Summary and Outlook 139
7.1 Summary . . . 139
7.2 Outlook . . . 141

A Human Auditory 143
A.1 The Hearing Process: Ear . . . 143
A.1.1 Parts of the Ear . . . 143
A.2 Psychoacoustics . . . 152
A.2.1 Critical Band Rate . . . 152
A.2.2 Level and Specific Loudness . . . 155
A.2.3 Temporal Masking . . . 156

B Demonstrator Setup 159
B.1 Demonstrator Hardware . . . 159

B.1.1 Demonstrator Hardware Features 161
B.2 Demonstrator Software 166
B.2.1 Demonstrator Software Modes 167
B.3 Demonstrator 169

C BBP – Parameter Details **171**
C.1 SiN4 Thickness Variation 171
C.2 Poly-Silicon Thickness Variation 173
C.3 Beam Height Variation 175
C.4 SiN4 Pre-Stress Variation. 177
C.5 Poly-Silicon Thickness Variation 179

D Numerical Integration with Gauss Legendre **183**
D.1 Solver with Gauss Legendre 183

Bibliography **187**

CHAPTER 1

1 Introduction

This research topic is originated from a cooperation between *Infineon Technologies AG Munich*, *Carinthian Tech Research (CTR) GmbH* and the *University of Technology Vienna*. The purpose of this thesis is the development of a MEMS speaker derived from the inversely driven silicon microphone (MEMS microphone E2120M; can be found in final product with package and ASIC: SMM310).

1.1 Motivation

The market for mobile devices like laptops, tablets or mobile phones is increasing rapidly. Device housings get thinner and energy efficiency is more and more important for battery powered devices. E.g., Micro-Electro- Mechanical- Systems (MEMS) loudspeakers, fabricated in complementary metal oxide semiconductor (CMOS) compatible technology merge energy efficient driving technology with cost economical fabrication processes. The major disadvantages of conventional electro-dynamic speaker systems like size in dimension, complexity in fabrication and efficiency are the advantages of the electrostatically actuated MEMS speaker. The design and evaluation process of such electrostatic CMOS MEMS speakers is time consuming and expensive, but can be supported and optimized with computer aided engineering methods. The accurate modeling of such MEMS devices results in a system of coupled partial differential equations (PDEs) describing the interaction between the electrostatic, mechanical

and acoustic field. By applying the finite element method (FEM) the physical domains and their interactions can be solved.

Sound pressure level can be increased by increasing surface area, membrane stroke level and frequency. The limitation of stroke level is given by manufacturer side, due to etching processes. The limitation in surface area is given by consumer, because the smaller the MEMS speaker, the easier to apply to new products. The third limitation is given by frequency directly by human auditory. The challenge is now to combine these three factors within their bounds and optimize it towards sound pressure level and total harmonic distortion.

The main goal of this thesis is finding an accurate model, describing the physical behavior of the E2120M silicon microphone and optimize it towards generating high sound pressure level and total harmonic distortion. By the help of computer aided engineering, the fabrication and manufacturing of new structures and ideas towards a MEMS speaker system should be supported. All models have to be optimized primary for accuracy and physical field interactions and secondary on computational time and amount of memory. Hence, driving concepts, like the digital sound reconstruction of snap-in can be trimmed towards increasing the sound pressure level.

1.2 Current Status of Research

In the field of MEMS micro- speakers a differentiation between in ear applications and free field applications can be done. Requirements of in ear applications are focused on low total harmonic distortion with coincidently small physical dimensions and low energy consumption, while free field applications are designed to obtain high sound pressure levels allowing larger surface areas.

Conventional free field applications are mostly based on the electro dynamically driving principle, hence they constitute quasi state of the art in MEMS speaker for mobile applications. It is called “quasi state of the art”, because integrated solutions based on electrostatic driving principle are a rapidly growing field on a new market of MEMS speakers. Some examples for electro-dynamic MEMS speakers can be found in [1-7] for circular shaped membranes and in [8] for rectangular membrane designs. Going towards integrated speakers, opens up the opportunity to design small transducer arranged is arrays, as described by [5, 7, 9, 10]. As mentioned before, the electrostatic MEMS speaker is an increasing driving technology, therefore papers and patents about

various fabrication and processing steps can be found in [11-17], but no marked-ready products are available yet. Basic information on research of standard electrostatic speakers can be found in [18-20], in the range of human auditory (20 Hz to 20 kHz [21]), or in [22] for an ultrasonic transducer CMUT application in the frequency range of 60 kHz to 160 kHz. Since standard electrostatic speaker systems with single ended composition are highly nonlinear, signal pre-distortion is an important point, as discussed in [23] generally on single speakers and in [24] specialized on speaker arrays, taking wave propagation properties into account. In 2003 the idea of integrated speaker arrays came up by [25, 26] and [27], followed by basic working principle of digital sound reconstruction [28, 29]. Piezoelectric speakers form the third MEMS speaker driving technology, for single frequency buzzers, up to wide frequency speaker systems. Wide frequency in this context is referred to human auditory. Most actuators show square shaped membranes [30-32], oscillating cantilevers [33] or octagonal shaped structures [34], but all of them are single speaker investigations.

The second field of application is represented by in ear applications. The in ear micro speaker has to fill a small cavity of sound, which represents the in ear volume of the human ear canal, called the auditory meatus. Therefore, the emitted sound pressure level of these speaker systems have not to be as high as the free field applications. Dedicated research on in ear applications or hearing aids can be found in [35-39].

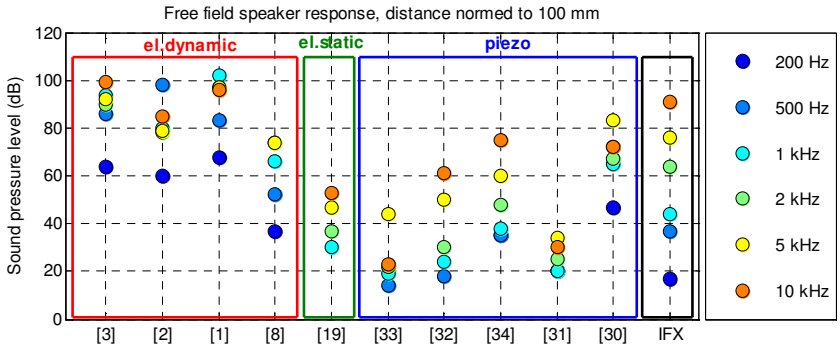

Figure 1-1: SPL comparison of electrostatic, electrodynamics and piezo MEMS speakers at a distance of 100 mm [40].

A detailed overview and comparison of the three driving technologies (electrostatic, electro-dynamic and piezo) is given in [40]. A comparison of the maximum sound pressure level on free field MEMS speakers at a distance of 100 mm, is depicted in Figure 1-1. IFX is our MEMS speaker array, consisting of 255 speaker elements.

1.3 Thesis Specification

In this thesis models have to be developed to describe the working principle of the current MEMS micro speaker used. The current micro speaker is a micro electro mechanical capacitive microphone, which is used as an inverse transducer to generate sound. Focus of this thesis is the evaluation of mechanical and acoustic behavior and describing these physical components within a finite element model (FEM). In addition investigations have to be done for analogue and digital sound reconstruction (DSR) used in single speaker cells or aligned in arrays. The leading thought behind an array usage is the increase of sound pressure level by increasing the active area, so the array method is a fundamental way for digital sound reconstruction. The inverse operated microphone is an electro statically driven MEMS which can be fabricated in CMOS technology easily, cheap and in big lots, therefore it is a very interesting technology for semiconductor industry. Focus of this work will be the evaluation of a model beginning at a control voltage up to the output sound pressure level (SPL) at any distance. Additionally, an analog eight channel MEMS speaker driver called "demonstrator" has to be developed, to be able to investigate digital sound reconstruction, sound pressure levels, total harmonic distortion and pre-distortion in the input voltage.

1.4 Structure of the Thesis

Chapter 1: An introduction on the field of MEMS speakers is given, with respect to electro-dynamic, electrostatic and piezo speaker systems.

Chapter 2: This chapter introduces basic terms regarding driving principle like single ended and push-pull or pull-pull systems, followed by the difference between analog and digital sound reconstruction. In addition to this the advantages and disadvantages of the snap-in mode

are explained. This knowledge is of importance for understanding the MEMS speaker models. Finally, the full transducer model is explained by its modules.

Chapter 3: The focus of this chapter is on the electrostatic-mechanical coupling. First, mechanical basics are treated, to be able to understand the nonlinearities considered in the mechanical model. Nonlinear solving strategies and mechanical contact states are explained subsequently. Derivations and computations of the electrostatic force introduce the correct implementation with TRANS126 elements and a multi-field model.

Chapter 4: This chapter starts with basics of acoustics and the mechanical acoustic coupling. Open domain modeling methods like perfectly matched layers and absorbing boundary conditions are utilized in combination with non-conforming grids in the propagation region, applying Mortar FEM. Acoustical investigations are made on the single speaker cell with FEM and on the eight-bit speaker array with Kirchhoff Helmholtz integral solution of the wave equation.

Chapter 5: This chapter deals with the first optimization stage, where the mechanical properties of the MEMS speaker are optimized towards increasing the volume between back plate and membrane. The buckling back plate is introduced as a self raising structure, where stress stiffening effects of various parallel layered materials are applied.

Chapter 6: This chapter deals with the second optimization stage, where digital sound reconstruction is applied. First the functional principle is explained, followed by introducing digitally weighted speaker arrays. By the help of this digital speaker array, three driving patterns are investigated, relating to sound pressure level and total harmonic distortion – theoretically and by measurements.

Chapter 7: This chapter summarizes the results of the thesis and gives a brief outlook of future work and possibilities of the MEMS speaker.

Appendix A: The MEMS speaker is an acoustical device, therefore the importance of understanding human auditory is high. First, the outer or external ear is explained, where the ear canal model is derived.

Second, the middle ear and third the inner ear working principle is treated. Finally, psychoacoustic effects dealing with critical band rate, loudness and masking are discussed.

Appendix B: This chapter explains the developed demonstrator or amplifier of the MEMS speaker, used for digital sound reconstruction investigations and measurements. Printed circuit board layouts, electrical circuits, software flow-charts and a feature overview can be found.

Appendix C: This chapter includes the raw data of the in chapter 5 explained buckling back plate parameter investigations.

Appendix D: This chapter describes the numerical integration method according to Gauss Legendre, as it is used in the Kirchhoff Helmholtz wave field computation tool.

CHAPTER 2

2 Electrostatically Actuated MEMS Speaker

This chapter introduces the main terms which are used to describe and model the MEMS speaker. At the beginning, the functional principle of an electrostatically actuated MEMS speaker is treated. The advantages and disadvantages of a single ended system are compared to the push-pull or pull-pull system. In the next section, the difference between analog and digital sound reconstruction techniques are explained, where speaker arrays are introduced too. Next the stable and instable operation modes, referring to the snap-in and release movement are discussed. Finally, a model simplification strategy and the full MEMS speaker modeling chain are explained.

2.1 MEMS Speaker Modes of Operation

Two parallel electrodes are needed to drive a MEMS speaker with the electrostatic driving principle in the simplest setup. There are two commonly used systems, first the single ended system and second the push-pull or pull-pull system.

2.1.1 Single Ended Driving Principle

Single ended setups work very stable in comparison to the push-pull or pull-pull electrostatic speaker. This is a direct result of the simple mechanical setup, where two electrodes are used in parallel. The top electrode (stator or back plate) is mechanically fixed, while the second

electrode representing the membrane is flexible (see Figure 2-1). By applying a voltage between both electrodes, the electrostatic attracting force (see section 3.4) pulls the flexible membrane towards the stator, which is called forcing state. If the membrane is already attracted or electrically loaded and the supply is switched off, the stored potential energy in the membrane is transferred into kinetic energy and flips away in opposite direction; hence this state is called release state. Both forces, first the electrostatic attracting force caused by the voltage between the electrodes and second the mechanical restoring force of the membrane are in equilibrium state. The restoring force can be adjusted by tensile pre-stress in the membrane due to fabrication process and must be computed nonlinearly due to large deformations (see section 3.2 and section 3.3). The operation point of the membrane can be adjusted by a bias voltage. By applying a modulated voltage, the membrane starts to move forth and back, depending on which force is stronger (mechanical or electrical). Both forces are in equilibrium state for this operation mode (non snap-in mode). The quadratic relation between electrical force and voltage applied, results in a low-distorted system only for small membrane displacements. The voltage to displacement relation increases nonlinearly up to the snap-in point, where the electrical force and the mechanical pull-back force are out of balance and the system jumps onto an instable mode (snap-through characteristic – see section 3.7.2). At the snap-in point the membrane is abruptly pulled towards the back plate until mechanical contact occurs. Figure 2-1 displays the driving principle of the single ended speaker system with its three states.

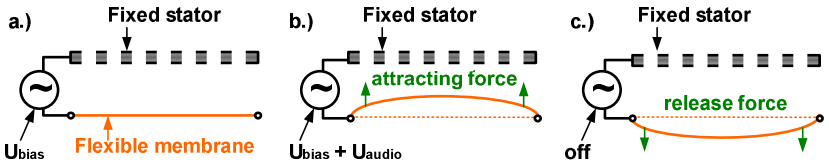

Figure 2-1: Working principle of single ended electrostatic speaker systems with its three states: a.) operation point with pre-supplied bias voltage, b.) force state with electrostatic force of modulated voltage and c.) release state with mechanically set back force of membrane.

The advantage of this method is the ease of fabrication in CMOS technology. However, the disadvantages are the strong nonlinear force versus displacement relation, as well as the only attracting force possible in this setup which results in a small stroke level. Furthermore, gap deviations in etching processes show quadratic impact on the movement characteristics due to quadratic linkage between gap and force.

2.1.2 Push-Pull or Pull-Pull Driving Principle

The improvement of the single ended system is known as push-pull or pull-pull system. Both disadvantages like gap size and nonlinear force to voltage relation can almost be compensated by the mechanical setup. Simulations in this thesis are based on the single ended system, because the single ended system describes the working principle with all effects and can be adapted easily to the push-pull or pull-pull system. For this setup the membrane (electrode two) is located between both stators (electrode one and three). Both stators are perforated to achieve acoustically transparent stators and minimize squeeze film damping [41, 42]. The basic working principle is depicted in Figure 2-2.

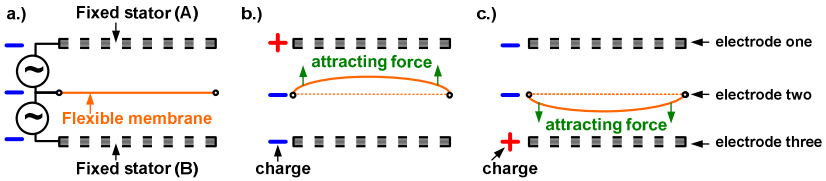

Figure 2-2: Working principle of a push-pull or pull-pull electrostatic speaker system with its three states: a.) operation point with bias voltage as idle state b.) attracting force linked to bias and a modulated voltage on the side of stator B and c.) towards stator A.

At the idle mode, all electrodes have the same charge level. By increasing the charge on one back plate, the membrane starts to attract in that direction as shown in Figure 2-2 b.) and c.). Based on the mechanical setup, the stroke level of the membrane is doubled, compared to the single ended setup. All simulation data and measurements in this thesis are based on the single ended system, if not mentioned explicitly.

2.2 Sound Reconstruction

Sound reconstruction methods deal with techniques to generate audible sound pressure levels. The following sections give an overview about the difference between analog and digital sound reconstruction.

2.2.1 Analog Sound Reconstruction

By utilizing analog sound reconstruction, the membrane ideally oscillates at the same frequency and amplitude as the desired audio signal. If a 500 Hz sinusoidal signal with an arbitrary amplitude is applied on the speaker, the membrane follows these oscillations with an corresponding stroke level. As a result, the audio signal is a direct consequence of the applied voltage regarding frequency and stroke level. The functional principle is depicted in Figure 2-3.

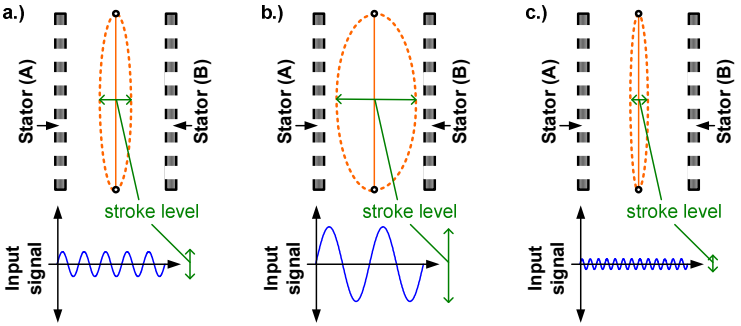

Figure 2-3: Analog sound reconstruction, where membrane stroke level follows the applied voltage.

Thus, the applied voltage results in a change in stroke level.

2.2.2 Digital Sound Reconstruction

In this context, digital sound reconstruction (DSR) has nothing to do with digital audio signals as used in MP3 or compact discs. The DSR in this context is based on the membrane excitation and therefore differs significantly from the analog sound reconstruction principle. As mentioned before, the applied voltage results in an change in stroke level for the analog method, while in the digital method stroke level is driven at full amplitude, while the surface area varies corresponding to

the input signal. Hence, the digital principle requires a large amount of single speaker cells, which are interconnected in arrays (see section 6.1.1). In most cases, the addressing of the individual cells is weighted bitwise, therefore the least significant bit (LSB) is linked with a single cell, while the most significant bit (MSB) is linked with the half amount of all speaker cells in the array. In our case the MEMS speaker is an eight bit speaker, which can be controlled digital and analog. In the digital sound reconstruction, as the name implies, each membrane is operated either with full amplitude (digitally true/one) or remains in its bias or idle position (digitally false/zero). In general, the audio input signal is digitalized and the corresponding amplitude is allocated with the related speaker bit groups. A simplified working principle of the eight bit speaker is displayed in Figure 2-4. There is also the possibility to combine digital and analog techniques, which are called hybrid mode (see section 6.4.2).

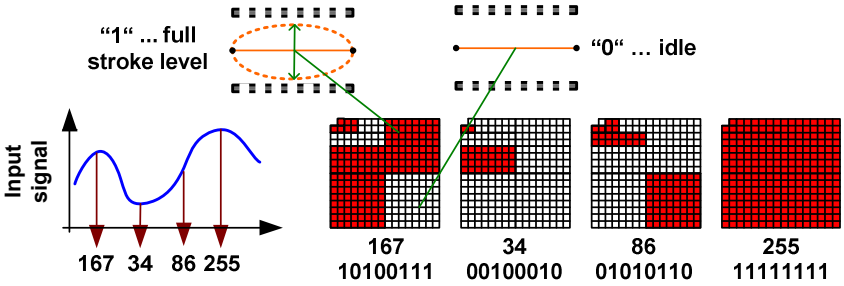

Figure 2-4: Amount of simultaneously oscillating speaker cells corresponds with digitally sampled audio input signal at digital sound reconstruction.

It has to be mentioned, that only integrated solutions, such as MEMS, are feasible for digital sound reconstruction. Arrays with small physical dimensions can be seen as point sources, while large physical arrays within the range of audible wavelengths, have to consider wave propagation effects (see section 6.1.1).

2.3 Membrane Movement Characteristics

The membrane movement characteristic is defined with two modes. First, the non-snap in mode, where the membrane follows the applied

acoustical voltage signal. In this driving state the system is in equilibrium of forces (restoring mechanical force and electrostatic attracting force), the membrane stroke level is low and the distortion is quadratic. The second mode is the snap-in mode, where the restoring force is lower than the electrostatic attracting force and the membrane is pulled abruptly towards the stator, where mechanical contact occurs. In this state the stroke level is higher compared to the non-snap in mode. Below the snap-in point, the membrane can be controlled directly via supply voltage, while above the snap-in point the membrane is forced rapidly towards the back plate. Figure 2-5 displays the stroke level of the membrane versus applied voltage. The left side shows the center point stroke level where the quadratic distortion can be seen below the snap-in point. The right side displays the membrane versus displacement over the radius.

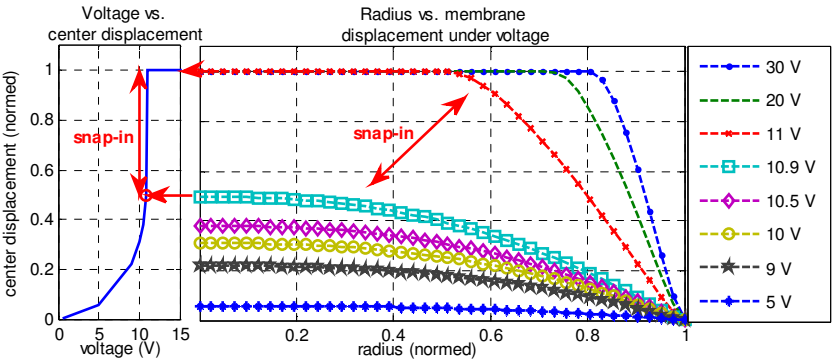

Figure 2-5: Voltage driven MEMS speaker in snap-in mode. Membrane center displacement (left) and axis rotational overview (right).

Since the electrostatic force is only an attractive force, the membrane has to be loaded with a DC voltage. Therefore, the membrane oscillates around the bias point with a forth and back movement.

2.3.1 Non-Snap-In Operation Mode

As already mentioned, applying a voltage below the snap-in point results in a quadratically distorted membrane movement. In our case the snap-in point was determined at about eleven volt, hence the speaker was driven up to ten volt, including a bias voltage, for the

following investigation. In the first test, depicted in Figure 2-6, the speaker was driven between one volt and ten volt, with a triangular shaped stimuli. As can be seen, the membrane stroke level is nonlinear and corresponds to a quadratic function. Sinusoidal stimuli and movement characteristics are of interest from the acoustical point of view, since they define the clearance of a tonal signal with respect to the total harmonic distortion. In the second investigation the membrane was loaded with a sinusoidal stimuli. The result is depicted in Figure 2-7, where the applied voltage is displayed on top and the resulting membrane stroke level on bottom.

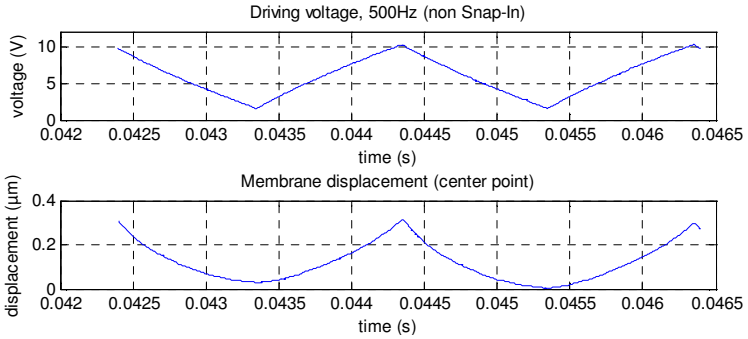

Figure 2-6: Voltage driven membrane between one volt and ten volt with triangular shaped stimuli (top) results in quadratically distorted membrane stroke level (bottom).

Both results outline the quadratic distortion of the transducer, hence a pre-distortion of the applied signal must be implemented to improve the total harmonic distortion. Additional information on acoustic pre-distortion can be found in [23, 24, 43, 44].
Increasing the voltage over the snap-in point results in an abrupt attraction towards the second electrode until mechanical contact occurs.

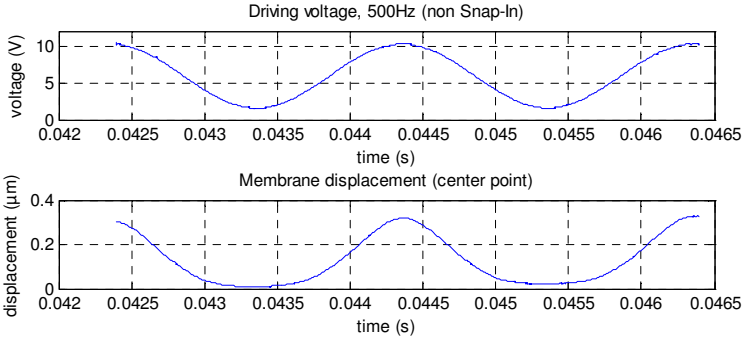

Figure 2-7: Voltage driven membrane between one volt and ten volt with sinusoidal shaped stimuli (top) results in quadratically distorted membrane stroke level (bottom).

2.3.2 Snap-In Operation Mode

To investigate the snap-in behavior, the investigations of section 2.3.1 were used with a higher voltage applied. Figure 2-8 displays the linear input as triangular voltage.

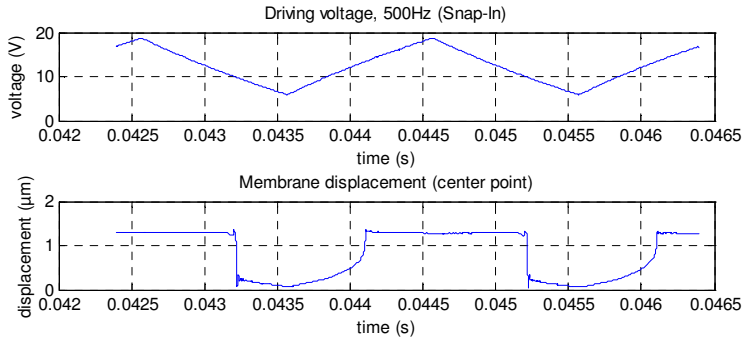

Figure 2-8: Voltage driven membrane between six volt and 20 volt with triangular shaped stimuli (top) results in quadratically distorted membrane stroke level with snap-in at about 13 volt and release at about nine volt (bottom).

As can be seen, the membrane movement represents rather a rectangular characteristic, than a triangular one. In comparison to the non snap-in driving mode, the full stroke level is used, which results in maximum sound pressure level possible for the MEMS speaker system. Due to the fast acceleration in the snap-in and release point, the audio signal is hardly distorted and useless for high fidelity audio or signals with low total harmonic distortions. The second investigation is based on a sinusoidal stimuli and depicted in Figure 2-9. From acoustical point of view, there is no difference at the membrane movement characteristics between the sinusoidal and triangular stimuli. The marginally variation between both movements can be found in the non snap-in stroke levels range, where the amplitude is that small, that the amount in sound pressure level can be neglected. The overall signal distortion is defined first by the release characteristics and second by the snap-in characteristics. The snap-in and release points have different voltage levels, hence there is a hysteretic behavior of the membrane, which is displayed in Figure 2-10.

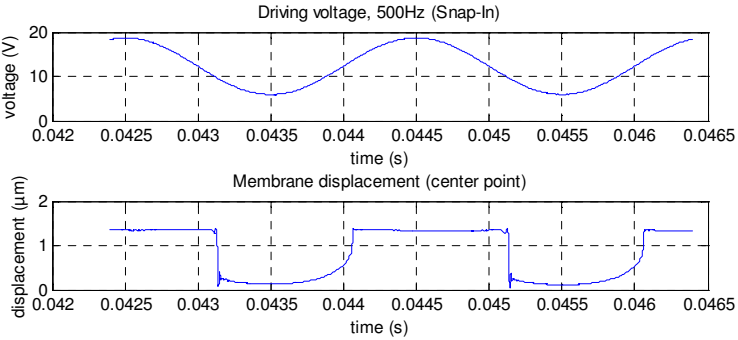

Figure 2-9: Voltage driven membrane between six volt and 20 volt with sinusoidal shaped stimuli (top) results in quadratically distorted membrane stroke level with snap-in at about 13 volt and release at about nine volt (bottom).

The measurement was performed with a single point laser vibrometer, hence the measurement point was not ideal aligned at the center position. Therefore, the amplitude of the measurement is smaller compared to the simulated results of Figure 2-10. Comparing the static

FEM results with measurements is only valid for electrical stimuli up to 33 kHz. Increasing the driving frequency over 33 kHz leads to inertial effects and transient mechanical behavior, which is not modeled in the static FE model.

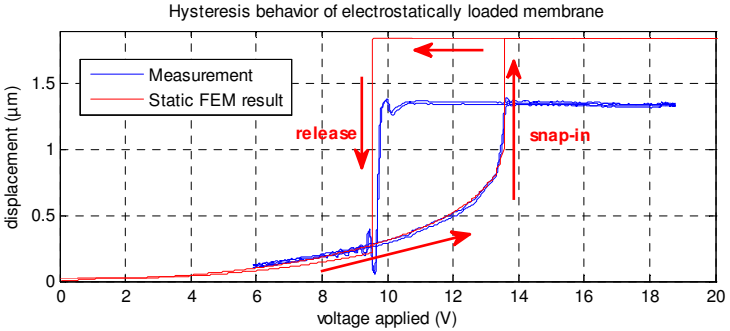

Figure 2-10: Comparison between FEM result und measurement of hysteretic behavior of the membrane driven in snap-in mode.

2.4 MEMS Speaker Modeling Chain

The speaker modeling chain is separated into an electrostatic-mechanical and a mechanical-acoustic model, where the first model transforms an input voltage into a membrane movement with the help of the electrostatic attracting force. The second part of the model will project the membranes movement into a propagating sound wave to compute the sound pressure level at the point of interest (POI). The modeling approach for designing the MEMS speaker is depicted in Figure 2-11. The electrostatic mechanical model is totally modeled with ANSYS in APDL. The acoustic block is modeled with CFS++ (see [45]) for single transducer investigations and small speaker arrays up to 16 elements. Additionally, a MATLAB tool solving the integral form of the wave equation is used to compute large arrays and investigate digital sound reconstruction.

Both models, firstly the electrostatic-mechanical and secondly the mechanical-acoustical model are separated at the membrane displacement, because the counteracting force of the surrounding air can be neglected [46]. To optimize computational time and amount of

memory, the complex three dimensional structure was reduced into a two dimensional axis symmetric model. Material parameters for modeling the perforated back plate in axis rotational domains and characterization of fabrication processes was determined by Füldner [47] in a prior work on MEMS microphone.

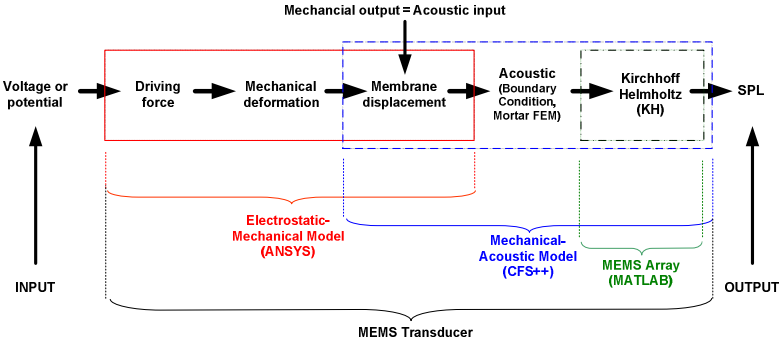

Figure 2-11: Major parts for modeling the MEMS speaker. Starting on the left side with an applied voltage resulting in a sound pressure level on the right side of the modeling chain.

Additional information about the modeling process can be found in [48-51].

CHAPTER 3

3 Electrostatic - Mechanical Modeling

This chapter gives an overview about mechanical basics, which have to be considered to model the electrostatic MEMS speaker system. The nonlinearities considered, like large deformation, stress stiffening, and contact, as well as the nonlinear electrostatic mechanical coupling are discussed. Additionally, the solution strategy for nonlinear systems are described. Subsequently, the electrostatic mechanical interaction is modeled by reduced order elements (TRANS126) and by a multi-field approach. Both methods are compared to an analytical solution derived from electrostatic force computation of a capacitance with layered permittivities. Finally, the results computed, are compared to measurement data of the snap-in characteristic.

3.1 Mechanical Basics

In this section, the basics about stress-strain relations are explained, to understand the mechanical partial differential equation(PDE) solved by FEM. The definition of stress and strain is not treated in detail, all necessary information can be found in [46, 52-54].

3.1.1 Stress-Strain Relation

The stress-strain relations are represented by Hookes law and describe the elasticity of a material. The linear and isotropic m-aterial tensor is defined by two Lamé parameters

$$\begin{pmatrix}\sigma_{xx}\\ \sigma_{yy}\\ \sigma_{zz}\\ \sigma_{yz}\\ \sigma_{xz}\\ \sigma_{xy}\end{pmatrix} = \begin{bmatrix}\lambda_L+2\mu_L & \lambda_L & \lambda_L & 0 & 0 & 0\\ \lambda_L & \lambda_L+2\mu_L & \lambda_L & 0 & 0 & 0\\ \lambda_L & \lambda_L & \lambda_L+2\mu_L & 0 & 0 & 0\\ 0 & 0 & 0 & \mu_L & 0 & 0\\ 0 & 0 & 0 & 0 & \mu_L & 0\\ 0 & 0 & 0 & 0 & 0 & \mu_L\end{bmatrix} \cdot \begin{pmatrix}S_{xx}\\ S_{yy}\\ S_{zz}\\ 2S_{yz}\\ 2S_{xz}\\ 2S_{xy}\end{pmatrix} \tag{3.1}$$

or, written in tensor notation

$$\boldsymbol{\sigma} = [c]\mathbf{S}\,. \tag{3.2}$$

Equation (3.1) is only valid for a linear dependency of stress and strain. As mentioned before, stress is defined by a force acting on a surface, which is Newton per square meter. The material tensor [c] is determined by the Lamé parameters (λ_L, μ_L) and includes the Poisson ratio and the Young's modulus (see [54]). These parameters characterize the stiffness of the material and usually are determined by measurements and fitting processes [55, 56].

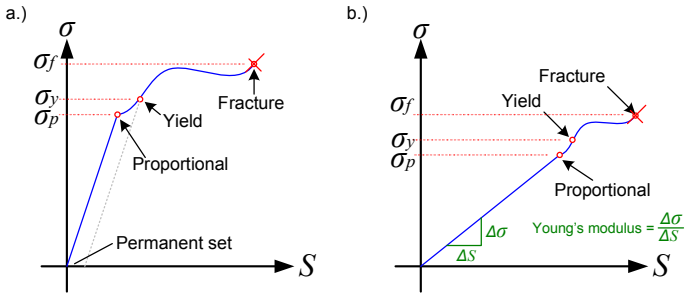

Figure 3-1: Stress-strain relation of stiff material (a) and soft material (b).

In Figure 3-1, three relevant stress-strain points and the difference between a stiff material and a soft material can be seen. Up to the proportional stress point (σ_p), the material behaves linearly. If an internal or external force acts on the body, a proportional deformation occurs. By reducing that force, the body returns back into its initial state. Increasing the force up to the yield stress point (σ_y), results in nonlinear or non proportional behavior. No plastic deformation occurs, the body is able to return into its initial state. If the force increases

over the yield stress point, a plastic deformation is the result. Removing the force leads to a permanent deformation. The last characteristic point is the maximum stress (σ_f). At this point the molecules begin to separate; as a result the body cracks or breaks. The MEMS speaker is driven in the linear mode for small membrane displacements, while nonlinearities must be considered for large membrane displacements as occurring in the buckling back plate system (see chapter 5 – Buckling Back Plate).

3.1.2 Mechanical PDE

At the equilibrium the sum of all acting forces, external and internal, have to be zero to achieve a state of rest

$$\int_{\Omega} \vec{f}_v \, d\Omega + \oint_{\Gamma(\Omega)} \boldsymbol{\sigma} \cdot d\boldsymbol{\Gamma} = \int_{\Omega} \rho \frac{\partial^2 \vec{u}}{\partial t^2} \, d\Omega \,. \tag{3.3}$$

In (3.3) the first term represents the forces acting inside the body, which are called inner forces. The second term represents the external forces acting on the surface of the body or structure. The right hand side is defined by the inertial force. These transient forces are in equilibrium state of both external and internal forces. By applying Gauss' divergence theorem on (3.3), we arrive at the PDE

$$\vec{f}_v + \nabla \cdot \boldsymbol{\sigma} = \rho \, \ddot{\vec{u}} \,. \tag{3.4}$$

The first term describes volume forces, which are transferred with mechanical fields. The second term describes surface forces, which are transferred with pressure and traction as described in [57]. The divergence operator on the symmetric Cauchy stress tensor σ is replaced by the $\boldsymbol{B}$ operator

$$B^{\mathrm{T}} = \begin{pmatrix} \frac{\partial}{\partial x} & 0 & 0 & 0 & \frac{\partial}{\partial z} & \frac{\partial}{\partial y} \\ 0 & \frac{\partial}{\partial y} & 0 & \frac{\partial}{\partial z} & 0 & \frac{\partial}{\partial x} \\ 0 & 0 & \frac{\partial}{\partial z} & \frac{\partial}{\partial y} & \frac{\partial}{\partial x} & 0 \end{pmatrix}. \tag{3.5}$$

Hence, the final partial differential equation for mechanical field, describing the physical quantities can be written as

$$B^{\mathrm{T}}[c]B\vec{u} + \vec{f}_v = \rho\ddot{\vec{u}} \,. \tag{3.6}$$

For the FE model, (3.6) will be multiplied by a test function and integrated over the computational domain. The benefit of this integration is the order reduction by one of the spatial derivative, obtained by an integration by parts. Furthermore, problems with discontinuous material parameters can be considered. An detailed derivation of this method can be found in [46]. The semi-discrete Galerkin formulation can be given as follows

$$\mathbf{M}\ddot{\mathbf{u}} + \mathbf{C}\dot{\mathbf{u}} + \mathbf{K}\mathbf{u} = RHS \,. \tag{3.7}$$

In (3.7), **M** is the mass matrix, **C** the damping matrix, **K** the stiffness matrix and *RHS* stands for right hand side. *RHS* represents all known values like boundary conditions and loads. The unknowns here are displayed with **u**, for displacement, and their first derivative for velocity and second derivative for acceleration. A damping can be introduced to the system, if **C** is computed via a linear combination of mass matrix **M** and stiffness matrix **K**. Further information about the so called Rayleigh damping model can be found in [46] and [58].

3.2 Nonlinearities

3.2.1 Large Deformation

For small deformations the difference between deformed state and initial state is not relevant and can be neglected as described in [59]. If the deformation or displacement comes into the scale of a designated structural dimension, the deformation can not be neglected anymore [52, 53, 60]. In this case, computations must be done, on the deformed (updated) geometry. In Figure 3-2 a.) the linear case for deformation is depicted. Stress is directly proportional to strain, because the material is in an elastic state. So a defined force results in a defined displacement. In Figure 3-2 b.) the geometry shows a large displacement in comparison to the membrane thickness, so a non-linear behavior has to be considered. Hence, if a force is implied, the membranes deflection is not directly proportional to this force as in case a.), the local deformation of the structure must be considered to compute correct displacements.

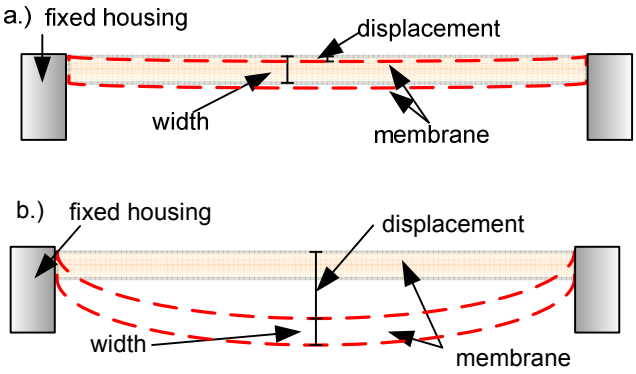

Figure 3-2: Comparison between a.) small displacement and b.) large displacement of a structure.

By using ANSYS as FEM tool, the nonlinear switch "nlgeom,on" must be used, to enable nonlinear mechanical behavior on membrane structure. From Lagrange point of view, the updated geometry must be used to compute the nonlinear iteration steps. For large deformation, the nonlinear rates on displacement have to be considered at the expansion of the membrane. Therefore, the deformation tensor must be re-computed. Large deformation can result in distorted elements. To avoid these problem, re-meshing the structure is suggested, if the element length to height ratio increases over factor ten. Additional information can be found in [61].
Since we are using FEM, the structure is discretized with elements, as shown in Figure 3-3. By applying a force, a deformation of the finite element side, which is defined in this figure from A to B, occurs. There is a change in position and length of the finite element shape and in addition a plastic deformation can occur. This mechanical curvature over the finite element edge can cause inaccurate results. As can be seen very well, if there is a bending deformation, the linear side A to B of the finite element would change to an arbitrary shape (depending on the deformation). This is a discretization error. In this case a finer mesh or high order FE should be used.

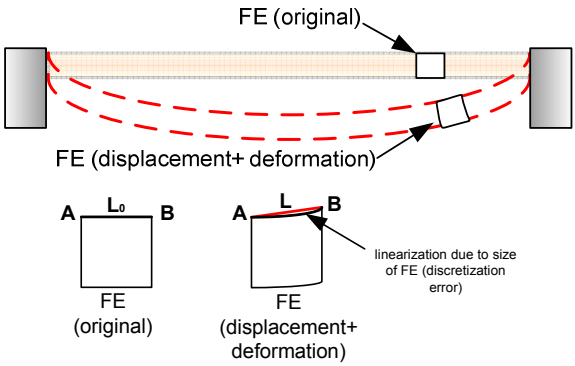

Figure 3-3: Calculation of large displacement on deformed and displaced FE.

To describe the mathematical model more accurate, the initial side L_0 and the deformed side L are assumed to be infinitely small, to get rid of this discretization error. Now, we denote with $d\omega_0$, the infinitely small part of L_0 and $d\omega$, the infinitely small part of the displaced and deformed length L.

$$\begin{pmatrix} X_{A_0} - X_{B_0} \\ Y_{A_0} - Y_{B_0} \\ Z_{A_0} - Z_{B_0} \end{pmatrix} = \begin{pmatrix} dX_0 \\ dY_0 \\ dZ_0 \end{pmatrix} = d\bar{\omega}_0 \quad \text{and} \quad \begin{pmatrix} X_A - X_B \\ Y_A - Y_B \\ Z_A - Z_B \end{pmatrix} = \begin{pmatrix} dX \\ dY \\ dZ \end{pmatrix} = d\bar{\omega} \tag{3.8}$$

By the help of Pythagoras' law, the length of the initial configuration and the length of the deformed configuration can be computed. Hence, we get the following relation for the initial length

$$dL_0^2 = dX_0{}^2 + dY_0{}^2 + dZ_0{}^2 = d\bar{\omega}_0{}^T \cdot d\bar{\omega}_0 \tag{3.9}$$

and for the deformed length

$$dL^2 = dX^2 + dY^2 + dZ^2 = d\bar{\omega}^T \cdot d\bar{\omega}\,. \tag{3.10}$$

The deformation gradient has to be introduced to describe the deformation of a point, located at the initial state (X_0, Y_0, Z_0), to its deformed configuration, defined by (X, Y, Z).

$$\vec{\omega}_0 = \begin{pmatrix} \frac{\partial X}{\partial X_0} & \frac{\partial X}{\partial Y_0} & \frac{\partial X}{\partial Z_0} \\ \frac{\partial Y}{\partial X_0} & \frac{\partial Y}{\partial Y_0} & \frac{\partial Y}{\partial X_0} \\ \frac{\partial Z}{\partial X_0} & \frac{\partial Z}{\partial Y_0} & \frac{\partial Z}{\partial Z_0} \end{pmatrix} \vec{\omega} = [F_d]\,\vec{\omega}. \tag{3.11}$$

The deformation gradient can be compared with the mapping function used in FEM. This mapping function uses the determinant of the Jacobi-matrix **J** to transform an arbitrary deformed finite element into its reference element. Green's law of elongation is used to describe the difference between the initial condition and the deformed condition related on length variation. Therefore (3.9), (3.10) and (3.11) results in the Green-Lagrangian strain tensor [V].

$$dL^2 - dL_0^2 = d\vec{\omega}^T d\vec{\omega} - d\vec{\omega}_0{}^T d\vec{\omega}_0\,, \tag{3.12}$$

$$dL^2 - dL_0^2 = d\vec{\omega}_0{}^T\, 2[\mathrm{V}]\, d\vec{\omega}_0\,. \tag{3.13}$$

As can be seen the Green-Lagrangian strain tensor combines the linear and nonlinear properties. A more detailed description of the derivation can be found in [46].
As a result, the strain tensor can be written as a decomposition into a linear and nonlinear part - see (3.14). The first term (blue) represents the linear part and the second term (red) describes the non-linear part.

$$S_{xx} = \frac{\partial u_x}{\partial x} + \frac{1}{2}\left[\left(\frac{\partial u_x}{\partial x}\right)^2 + \left(\frac{\partial u_y}{\partial x}\right)^2 + \left(\frac{\partial u_z}{\partial x}\right)^2\right], \tag{3.14}$$

$$S_{yy} = \frac{\partial u_y}{\partial y} + \frac{1}{2}\left[\left(\frac{\partial u_x}{\partial y}\right)^2 + \left(\frac{\partial u_y}{\partial y}\right)^2 + \left(\frac{\partial u_z}{\partial y}\right)^2\right],$$

$$S_{zz} = \frac{\partial u_z}{\partial z} + \frac{1}{2}\left[\left(\frac{\partial u_x}{\partial z}\right)^2 + \left(\frac{\partial u_y}{\partial z}\right)^2 + \left(\frac{\partial u_z}{\partial z}\right)^2\right],$$

$$2S_{yz} = 2S_{yz} = \frac{\partial u_y}{\partial z} + \frac{\partial u_z}{\partial y} + \frac{1}{2}\left[\left(\frac{\partial u_x}{\partial y}\frac{\partial u_x}{\partial z}\right) + \left(\frac{\partial u_y}{\partial y}\frac{\partial u_y}{\partial z}\right) + \left(\frac{\partial u_z}{\partial y}\frac{\partial u_z}{\partial z}\right)\right],$$

$$2S_{xz} = 2S_{yz} = \frac{\partial u_x}{\partial z} + \frac{\partial u_z}{\partial x} + \frac{1}{2}\left[\left(\frac{\partial u_x}{\partial x}\frac{\partial u_x}{\partial z}\right) + \left(\frac{\partial u_y}{\partial x}\frac{\partial u_y}{\partial z}\right) + \left(\frac{\partial u_y}{\partial x}\frac{\partial u_y}{\partial z}\right)\right],$$

$$2S_{xy} = 2S_{yx} = \frac{\partial u_x}{\partial y} + \frac{\partial u_y}{\partial x} + \frac{1}{2}\left[\left(\frac{\partial u_x}{\partial x}\frac{\partial u_x}{\partial y}\right) + \left(\frac{\partial u_y}{\partial x}\frac{\partial u_y}{\partial y}\right) + \left(\frac{\partial u_z}{\partial x}\frac{\partial u_z}{\partial y}\right)\right].$$

3.2.2 Stress Stiffening

Another very important effect to be taken into account in MEMS modeling, is stress stiffening. Large displacement results in a redistribution of internal strains, because the system has the ability to stay in equilibrium of forces. As described before, the speaker consists of different layers with various intrinsic pre-stress values. Figure 3-4 displays an external force applied to the center of the membrane or back plate where a redistribution of the stresses occurs and counteracts the external force as depicted in Figure 3-4 b.) to reach the equilibrium state of forces. It has to be mentioned, that Figure 3-4 is depicted as an angular flexible body, to optically demonstrate the effect.

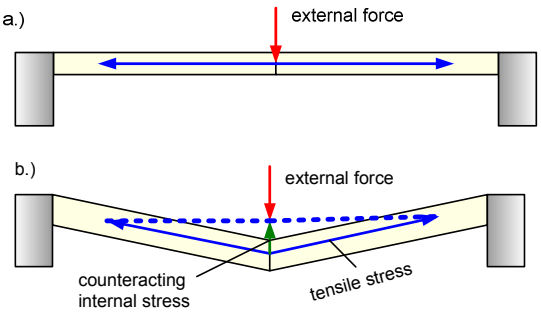

Figure 3-4: Stress stiffening effect, a.) external force applied on a membrane with tensile pre-stress, b.) resulting counteracting force.

3.2.3 Contact Case

In the most general contact case, two solid bodies, like membrane and back plate touch with their surfaces. This is called multi-body contact, since two or more bodies are in contact. There is also the possibility of a single body to get into contact, if the deformation is large enough to achieve single body contact. An example can be given with a beverage can, where an additional body is used to crush the can. The contact region, where the additional body hits the can is treated as a multi-body contact, but the regions where the sidewall of the can is in contact with itself due to large deformations, is treated as single body contact. From the point of FE modeling, the differentiation is important, since for the multi body case one body is the contact body and the other body is the target body. At the single body case, exactly this split of target and contact definition is the challenge. Additional information can be found in [62-64]. In an ideal contact case, there is no penetration and forces are transferred from one body to the other. Force transmission and penetration avoidance conditions have to be taken into account to model the contact case proper. Figure 3-5 displays the contact states of two bodies, starting at the two body model as can be seen in Figure 3-5 a.). As a result, gap (Figure 3-5 b.)), penetration (Figure 3-5 c.)), or contact (Figure 3-5 d.)) are defining the states.
According to [65] the contact condition itself basically does not depend on time, but on geometry, therefore the displacement based matrices of (3.7) can be reduced to

$$\mathbf{K}\,\mathbf{u} = \mathbf{f}\ . \tag{3.15}$$

There are to commonly used mathematical models as described by [66], the pure penalty method and the Lagrange multiplier method. Both methods have advantages and disadvantages, strongly depending on the physical behavior. A well documented description or guideline for obtaining contact convergence, is given in [62].

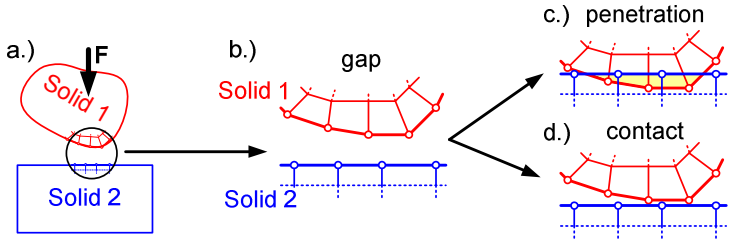

Figure 3-5: Two solid bodies a.) with gap state b.) leading to body penetration c.) or contact state d.).

Latest formulations for contact problems use a semi-smooth Newton method combined with a Mortar approach can be found in [67, 68].

Pure Penalty Method:

For the pure penalty method, (3.15) is modified by

$$\mathbf{K}_{\text{contact}}\Delta\mathbf{u}_{\text{penetration}} = \Delta\mathbf{f}_{\text{contact}} \tag{3.16}$$

where $\mathbf{K}_{\text{contact}}$ represents the contact stiffness, $\Delta\mathbf{u}_{\text{penetration}}$ the penetration depth or gap between the finite element nodes and the contact surface, and $\Delta\mathbf{f}_{\text{contact}}$ is the transmitted force from one body to the other. The penetration depth in this model is zero, if both surfaces are perfectly contacted. Figure 3-6 displays the iterative process to achieve a contact condition, where no contact force occurs in the first iteration due to the gap. In the second iteration the computed displacement is too large, hence penetration occurs. Based on this penetration depth a counteracting force is computed to realize the contact state, which is reached in the third step.

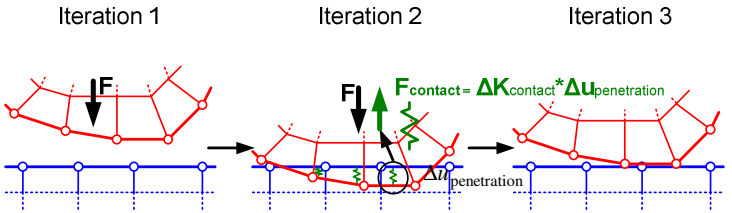

Figure 3-6: Iteration process of two solid bodies in contact state.

The contact stiffness matrix can be added to the global stiffness matrix, because of the same relation of displacement and stiffness. This is also valid for the resulting contact force, which will be represented by an external pressure or stress. For the penalty method, normal and tangential contact stiffnesses are fitted until the contact case is within the user specified accuracy. Hence, allowing a larger penetration depth, leads to fast but more inaccurate results, than low penetration depths. Caution must be kept on overlapping elements. A penetration depth of zero can not be achieved, since the contact stiffness tends to an infinite value in this case. Another problem for solving (3.16) is the ill-conditioned global stiffness matrix $\mathbf{K}$ caused by the extremely stiff contact stiffness matrix $\mathbf{K}_{\text{contact}}$. The ill-conditioned matrices can lead to problems for specific solvers as explained in [69].

Lagrange Multiplier Method:

In comparison to the penalty method, the Lagrange multiplier method does not compute a new stiffness matrix. In this method the contact force is added to the existing force as a new degree of freedom (DOF)

$$\begin{pmatrix} \mathbf{K}(\mathbf{u}) & \mathbf{K}(\mathbf{u},\boldsymbol{\lambda}) \\ \mathbf{K}(\mathbf{u},\boldsymbol{\lambda})^{\mathrm{T}} & 0 \end{pmatrix} \begin{pmatrix} \mathbf{u} \\ \boldsymbol{\lambda} \end{pmatrix} = \mathbf{K}\,\mathbf{u} = \mathbf{f} + \mathbf{f}_{\text{contact}} \,. \tag{3.17}$$

As a result, the contact condition is independent on contact stiffness and penetration depth. A disadvantage of this method is the increase of the stiffness matrix size. Because of the additional DOFs, the stiffness matrix slightly increases and the diagonal entries become zero. As a direct consequence the computational time is longer compared to the penalty method. At the Lagrange multiplier method, a sparse solver should be chosen, as mentioned in [66, 70]. Based on the sudden change in contact case, numerical oscillations can occur. These oscillations can be described with the penetration tolerance, the smaller the tolerance, the longer is the computational time, but the result is more stable for smaller penetration tolerances. In theory this method should yield for zero penetration depth (perfect contact) and zero tensile stress in contact case. But in practice the computational time would be infinite long, because of infinite amount of iteration steps.

3.3 Nonlinear Finite Element Solver

The choice of the nonlinear solver algorithm is important for convergence and it depends on the modeled system. This part of the thesis gives an overview about the linear and nonlinear solving possibilities and is not intended as a general detailed discussion.

3.3.1 Linear versus Nonlinear Behavior

The main difference between a linear and a nonlinear system is depicted in Figure 3-7.

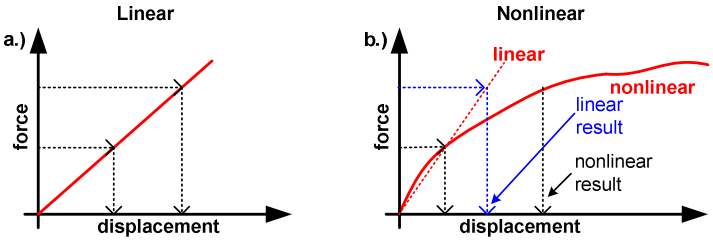

Figure 3-7: a.) Linear force displacement relation and b.) nonlinear force displacement relation.

As can be seen, in the linear case the unknown displacement is computed in a single step. In the nonlinear case, the result after the first solution step does not achieve the correct result. Hence, the nonlinear force displacement relation must be computed with a suitable algorithm. In most cases a sum of linearized computations are used to approximate the nonlinear behavior piecewise. The challenge is to minimize the error between the correct and the approximated (linearized) solution. Additionally the nonlinear force displacement relation is partitioned into load-steps (or sub-steps in ANSYS), to ensure convergence of the nonlinear method – see Figure 3-8. For the nonlinear force displacement relation, the external forces $\mathbf{f}_{ext}$ applied on the structure and the internal forces in the structure, have to be in equilibrium state. Since the internal forces are unknown, the FE method uses the internal displacements $\mathbf{u}$ to describe the nonlinear behavior

$$\mathbf{f}_{ext} = \mathbf{f}_{int}(\mathbf{u}) \,. \tag{3.18}$$

Therefore, the first stopping criterion is defined by minimizing the residuum

$$\mathbf{f}_{\text{ext}} - \mathbf{f}_{\text{int}}(\mathbf{u}) = \mathbf{R} \to 0 \tag{3.19}$$

which is zero at the exact solution. The numerical scheme approximates the exact solution by employing the tolerance bound

$$\left\|\mathbf{R}\right\| = \varepsilon_{\text{user}} \mathbf{R}_{\text{ref}} , \tag{3.20}$$

where $\| \ \|$ defines the vector norm. There are three available norms to choose in ANSYS [71], first the infinite norm

$$\left\|\mathbf{R}\right\|_{\infty} = \max\left|\mathrm{R_i}\right| \tag{3.21}$$

second, the L_1-norm

$$\left\|\mathbf{R}\right\|_{1} = \sum_{\mathrm{i}} \left|\mathrm{R_i}\right| \tag{3.22}$$

and third, the L_2-norm

$$\left\|\mathbf{R}\right\|_{2} = \sqrt{\sum_{\mathrm{i}} \mathrm{R_i^2}} \ . \tag{3.23}$$

The infinite norm is the maximum value of the residual vector, the L_1-norm is the sum the absolute values and the L_2-norm is the square root of the sum of the squares.
The second stopping criterion is a failsafe, limiting the number of iterations and aborting the simulation. Causes for reaching the failsafe may be too large load-steps, too small tolerance bounds in combination with too little allowed maximum iterations. As mentioned before, the nonlinear system is partitioned in load-steps and the correct solution is approximated directly or iteratively.

At the direct solving procedure, the Gaussian elimination method is applied. With this method, the system of equations is solved exactly within numerical accuracy. The advantage of this procedure is the fixed amount of computational steps, which lead to an easy estimation of computational time. For small problems the advantages dominate like robustness and solver simplicity. One disadvantage of this procedure are the high memory costs. Iterative methods start at an initial guess and improve the approximation until an absolute error reaches the pre-

defined tolerance. Additional information about direct and indirect solving procedures can be found in [72, 73].

The following sections deal with Newton Raphson and modifications as iterative solving routines.

3.3.2 Newton Raphson

The Newton Raphson (NR) algorithm works as follows; The input for the NR is the applied external force ${}^{m}\mathbf{f}_{ext}$ (load-step start value), where index ${}^{(m)}$ defines the actual load-step increment counter. This value must fulfill the equilibrium condition ${}^{m}\mathbf{f}_{ext} = {}^{m}\mathbf{f}_{int}$ including a defined tolerance, inside the load-step. As a consequence, the added load increment ${}^{m+1}\mathbf{f}_{ext}$ breaks the equilibrium condition and the new displacement increment ${}^{m+1}\mathbf{u}$ must be computed iteratively. In this way, the force displacement relation

$$\mathbf{K}\,\mathbf{u} = \mathbf{f}\,, \tag{3.24}$$

can be written as

$$\mathbf{K}^{(i)}\left[\mathbf{u}^{(i+1)} - \mathbf{u}^{(i)}\right] = {}^{(m+1)}\mathbf{f}_{ext} - {}^{(m+1)}\mathbf{f}_{int}^{(i)}\,, \tag{3.25}$$

where ${}^{(i)}$ represents the iteration step. The procedure is depicted in Figure 3-8 for an arbitrary load step in more detail on the left side and multiple load steps on the right side.

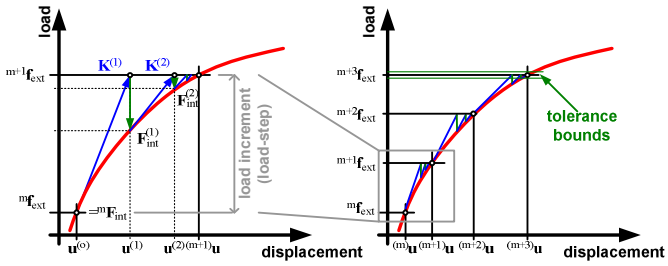

Figure 3-8: Standard Newton-Raphson method with load-steps (right) and iteration scheme of arbitrary load-step (left).

As can be seen, the tangential stiffness matrix $\mathbf{K}^{(i)}$ changes for each displacement step $\mathbf{u}^{(i)}$ in each iteration. This requires a re-computation of the stiffness matrix for each iteration step, up to the convergence

criterion, where the displacement change is within tolerance bounds (3.20).

An optimization of the standard Newton Raphson algorithm can be found in the re-computation of the tangential stiffness matrix for each step. For instance, the frozen Newton Raphson (FNR) computes the tangential stiffness matrix only for the first iteration step and re-uses it for the following iteration steps in the actual load-step. The functional principle of the frozen Newton Raphson method is depicted in Figure 3-9.

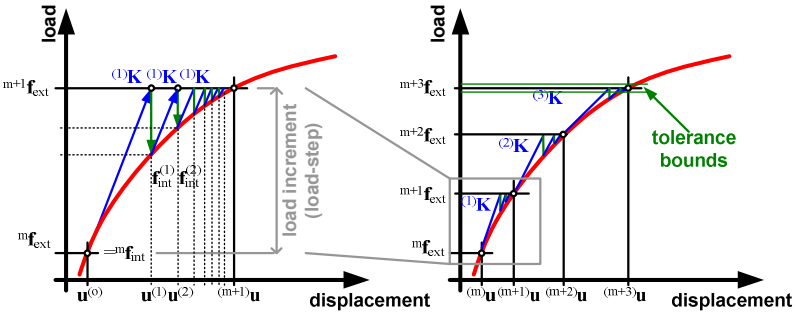

Figure 3-9: Frozen Newton-Raphson (FNR) method.

As can be seen in Figure 3-9, the tangential stiffness matrix is not recomputed for each iteration-step, but only once for each load-step. Using the first tangential stiffness matrix in each iteration for each load-step can also be used for weak nonlinear systems, but is not advisable for strong nonlinear behavior. Hence,

$$\mathbf{K}^{(0)} = {}^{m}\mathbf{K} = \mathbf{K}({}^{m}\mathbf{u}) \tag{3.26}$$

results with (3.25) in

$$\mathbf{K}^{(0)}\left[\mathbf{u}^{(i+1)} - \mathbf{u}^{(i)}\right] = {}^{(m+1)}\mathbf{f}_{ext} - {}^{(m+1)}\mathbf{f}_{int}^{(i)}\,. \tag{3.27}$$

Due to the re-computation of the tangential stiffness matrix for each iteration step, the computational effort stands in tradeoff with the convergence. The rate of convergence for the standard NR method is quadratic, while the FNR has a linear convergence rate.

The main problem of both methods can be found in the load step size in combination with strong nonlinear systems. The classical textbook

example [74] deals with a von Mises framework loaded up to the snap-through point. For these nonlinear systems with snap-through characteristics, the arc-length method is suitable. A snap-through characteristic has a local maximum and a local minimum in the force displacement relation. If the load step increment size is chosen too large, divergence can occur as displayed in Figure 3-10 by applying the standard NR or FNR. In this example the third load increment was set higher than the snap through point. An infinite iterative loop is the result, stopped by the maximum number of iterations. Experiments have shown, that dynamic load step adaption algorithms fail for snap-through characteristics in combination with standard NR or FNR.

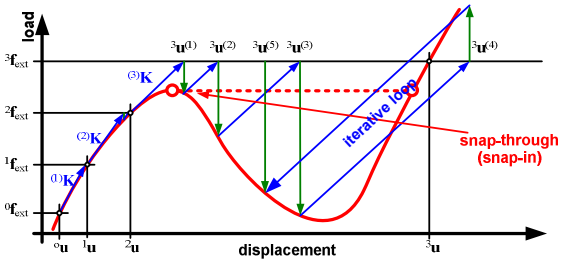

Figure 3-10: Frozen Newton-Raphson with snap-through and a divergence behavior.

3.3.3 Arc-Length Method for Snap-In Instabilities

Mechanical characteristics like snap-through instabilities can be computed by using an additional improvement of the Newton Raphson method, which is known as the arc-length method. As depicted schematically according to Riks Wempner in Figure 3-11, the tangential stiffness matrix is computed for the first iteration step and extended with an circular constraint. In the n-dimensional case the circle changes to a hyper-sphere.

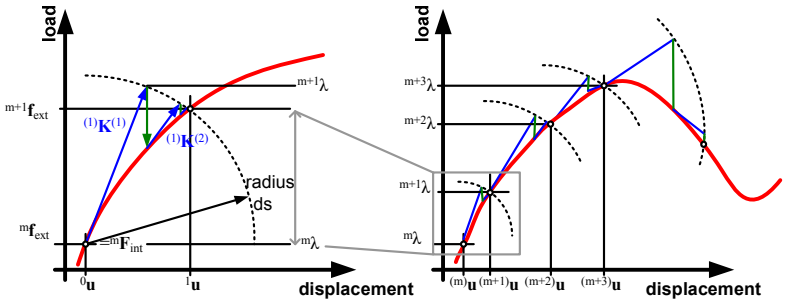

Figure 3-11: Arc-length method with standard Newton-Raphson algorithm for snap-through instabilities for one load step (left) and multiple load steps (right).

Since the circular constraint is a nonlinear term, the load increment is computed with a scaling factor according to a reference load

$$ {}^{m}\mathbf{f}_{\text{ext}} = {}^{m}\lambda \mathbf{f}_{\text{ref}} \, . \tag{3.28} $$

The arc-length constraint for the hyper-sphere can be written as

$$ [\mathbf{u}^{(i+1)} - \mathbf{u}^{(0)}]^{T} [\mathbf{u}^{(i+1)} - \mathbf{u}^{(0)}] + ({}^{m}\lambda - {}^{m-1}\lambda)^{2} = ds^{2} \tag{3.29} $$

hence, (3.25) results in

$$ \mathbf{K}^{(i)} \left[\mathbf{u}^{(i+1)} - \mathbf{u}^{(i)} \right] = \lambda^{(i+1)} \mathbf{f}_{\text{ref}} - \mathbf{f}_{\text{int}}^{(i)} \, . \tag{3.30} $$

Information about the modified Riks Wempner, using a hyper-plane and the Risk Wempner Ramm method, using an alternative computation of the tangential stiffness matrix, can be found in [58, 75] as well as [76].

3.4 Electrostatic Force Computation

The electrostatic force computation can be performed with Coulomb's method or with the principle of virtual work. Both methods are described briefly. A more detailed derivation of both methods is given in [77] and [51].

3.4.1 Electrostatic Force - Coulomb's Method

Coulomb's method assumes a capacitor without electric fringe fields. This can be achieved by using guard rings around the electrodes or large diameter to distance ratios. The guard ring keeps the electric field between both electrodes homogeneous, while it is located around the top electrode and loaded with the same potential as the bottom electrode. The guard ring setup was developed at the electrometer in 1880 [78] and is also commonly used in CMOS technology to avoid crosstalk nowadays. Figure 3-12 displays the electrometer on the left side and the plate type capacity analogy on the right side.

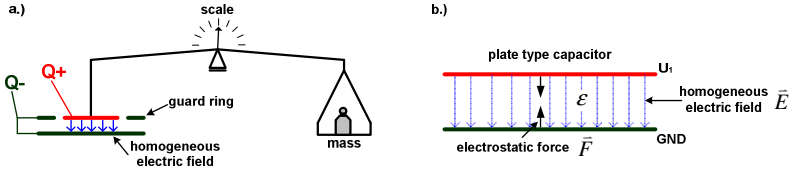

Figure 3-12: a.) Electrometer according to [79] and b.) plate type capacitor setup with single permittivity and homogeneous electric field.

The electrostatic attraction derives from Coulombs law [77] and reads as follows

$$\vec{F}_{12} = \frac{Q_1 Q_2}{4\pi\varepsilon r^2}\vec{r}\,, \tag{3.31}$$

where $\vec{F}_{12}$ represents the force between charge Q_1 and Q_2 and it decreases with the factor $4\pi\varepsilon$ and the square of distance r. The electric field of a single point source can be represented by

$$\vec{E} = \frac{Q}{4\pi\varepsilon r^2}\vec{r}\,. \tag{3.32}$$

As a result, the total electrostatic force on a charge Q in an electric field $\vec{E}$ according to Coulomb by

$$\vec{F}_{\mathrm{el}} = Q\vec{E}\,. \tag{3.33}$$

The relation between charge Q, voltage U and the capacitance C is known by

$$C = QU \,. \tag{3.34}$$

The electric field is the negative gradient of the scalar potential φ simplified by the potential difference, which is the electric voltage, over a distance d

$$\vec{E} = -\nabla\varphi = \frac{U}{d} \,. \tag{3.35}$$

Hence, the total electrostatic force that pulls one plate towards the other can be computed by substituting with (3.34) and (3.35) into (3.33)

$$F_{\mathrm{el}} = \frac{\varepsilon A U^2}{2d^2} = \frac{1}{2d} C U^2 \,. \tag{3.36}$$

The factor one half comes from the fact, that each charge is surrounded by its own electric field. As depicted in Figure 3-13, two charged plates generate two electric fields in the volume between them. The upper plate is charged positively and induces the blue electric field and the lower plate is charged negatively and induces the red electric field. As defined in (3.31) the force is acting between both plates (charges), hence the two times higher electric field is taken into account. This computation is only valid with a single permittivity between the plates, based on the fact that various permittivities along the gap results in interface forces not included in (3.36). Layered capacity forces can be accurately computed by applying the virtual work method (see section 3.4.2).

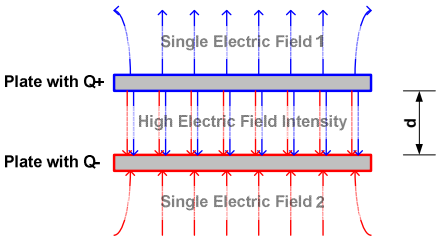

Figure 3-13: Electric field of tow surfaces with distance d.

3.4.2 Electrostatic Force - Virtual Work

In capacitors with layered dielectric materials between two electrodes, the electrostatic force cannot be computed with the Coulomb's method, because between these layers interface forces occur. The virtual work method for force computation uses the electric energy stored in the capacitor and takes permittivity changes into account. The electric field intensity and flux are used to determine Coulomb's force and interface force. Figure 3-14 displays the plate type capacitor of Figure 3-12 with an additional dielectric layer. In our case the material used is silicon nitride with a relative permittivity of 7.5 [80]. We assume homogeneous electric field between both electrodes. As a result, the normal component of the electric flux $\vec{D}$ is constant over the total volume (see Figure 3-14a.)), and can be linked with the electric field intensity $\vec{E}$ by

$$\vec{D} = \varepsilon \vec{E} \tag{3.37}$$

Therefore, the electric field changes with the rate of permittivity (see Figure 3-14b.)). The air gap and the insulation layer result in two capacitances in series. First, the insulation capacitance, which is mechanically stiff and therefore constant over the back-plate. Second the gap capacitance, which is represented by air and changes with the gap distance. The analogue circuit diagram is displayed in Figure 3-14c.), where both dielectric layers (air and insulation) can be modeled as capacitances, one fixed for the insulation layer and a variable one for the air gap. This implies the resulting forces, first the Coulomb force and second the interface force as depicted in Figure 3-14d.).

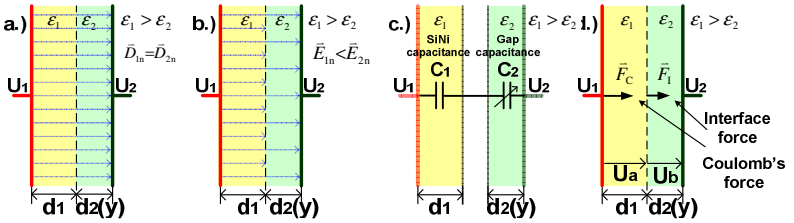

Figure 3-14: a.) El. displacement D, b.) el. field intensity E, analog circuit c.) and Coulomb's and interface force in d.).

From this context, we can compute the capacitances according to Figure 3-14c.), where the maximum capacitance occurs at the contact

case. In this case the air gap is closed and the membrane is in contact with the insulation layer

$$C_1 = C_{\text{fix}} = C_{\max} = \frac{\varepsilon_1 A}{d_1} . \tag{3.38}$$

In (3.28) ε_1 is $\varepsilon_0 \cdot \varepsilon_r$, A is the surface of the conducting back plate or membrane and d_1 the thickness of the insulation layer. Additionally, the variable air gap capacitance can be computed with

$$C_2 = C_{\text{var}} = \frac{\varepsilon_2 A}{d_2 - y} . \tag{3.39}$$

Hence, the total capacitance between the plates computes by

$$C = \frac{C_1 C_2}{C_1 + C_2} = \frac{\varepsilon_1 \varepsilon_2 A}{\varepsilon_1 d_2 + \varepsilon_2 d_1 - \varepsilon_1 y} \tag{3.40}$$

A moving electrode, towards the back plate results in a change in energy. A virtual displacement $\delta \vec{r}$, based on a force $\vec{F}_{\text{el}}$ results in a variation of the electrostatic energy $\delta \text{W}_{\text{el}}$

$$\delta \text{W}_{\text{el}} = \vec{F}_{\text{el}} \cdot \delta \vec{r} . \tag{3.41}$$

The energy density is computed via electric field intensity and the electric flux

$$\delta \text{w}_{\text{el}} = \frac{1}{2} \vec{D} \cdot \vec{E} . \tag{3.42}$$

The total electric energy is obtained, by integrating the energy density over the considered volume

$$W_{\text{el}} = \frac{1}{2} \int_{\Omega} \vec{D} \cdot \vec{E} \, d\Omega . \tag{3.43}$$

The total electrostatic force is the derivative of the electric energy in the gap and results in [46]

$$F_{\text{el}} = \frac{dW_{\text{el}}}{dy} . \tag{3.44}$$

The total electrostatic force can be split up to Coulomb's rate and the interface rate, where Coulomb's rate is derived by (3.33) and substituted with (3.34) and(3.37), which results in

$$F_{\mathrm{C}} = \frac{1}{2}\frac{Q^2}{\varepsilon_1 A} = \frac{1}{2}C^2U^2\frac{1}{\varepsilon_1 A}. \tag{3.45}$$

To obtain the total electro-static force we have to include the interface force between the insulation layer and air, where the permittivity changes. A comfortable way to compute this force is the use of the electrostatic pressure on this interface, which is represented with the normal component of the electric displacement vector and scales with the reciprocal rate of the difference of permittivity and the surface area

$$\sigma_{\mathrm{int}}^{\mathrm{el}} = \frac{1}{2}D_{\mathrm{n}}^2\left(\frac{1}{\varepsilon_1}-\frac{1}{\varepsilon_2}\right)A + \underbrace{\frac{1}{2}E_{\mathrm{t}}^2(\varepsilon_1-\varepsilon_2)}_{E_{\mathrm{t}}=0}. \tag{3.46}$$

The electric field intensity is homogeneous along the plate and tangential components do not appear, hence the second term cancels out. Therefore, if both permittivities are the same, the electrostatic pressure is zero and no interface forces occur. The electrostatic pressure is the ratio between interface force and surface

$$\sigma_{\mathrm{int}}^{\mathrm{el}} = \frac{F_{\mathrm{I}}}{A}. \tag{3.47}$$

Therefore, substituting (3.46), (3.37) and (3.47), we obtain the interface force

$$F_{\mathrm{I}} = \frac{1}{2}C^2U^2\left(\frac{1}{\varepsilon_1 A}-\frac{1}{\varepsilon_2 A}\right). \tag{3.48}$$

As a result, the total electrostatic force acting on the plate type capacitor can be written as the sum of Coulomb's force and interface force

$$F_{\mathrm{el}} = F_{\mathrm{C}} + F_I = \frac{1}{2}C^2U^2\left(\frac{\varepsilon_1-2\varepsilon_2}{\varepsilon_1\varepsilon_2 A}\right). \tag{3.49}$$

Figure 3-15 displays a parameter variation of the permittivity in the insulation layer versus a variable gap distance up to the contact case. As depicted in Figure 3-15 c.) the interface force is zero for insulation layers with the same permittivity values. For higher permittivity ratios, the ratio between Coulomb's force and interface force increases rapidly. Particularly for small gap distances near contact case the total force is almost exclusively defined by the interface force. Therefore, the computation of the electrostatic force according to Coulomb's method is not valid for permittivity changes along the gap, but can be used for single layered capacitances. In the case of various dielectric layers between the electrodes, the virtual work method must be used in order to include the interface forces acting on the structure.

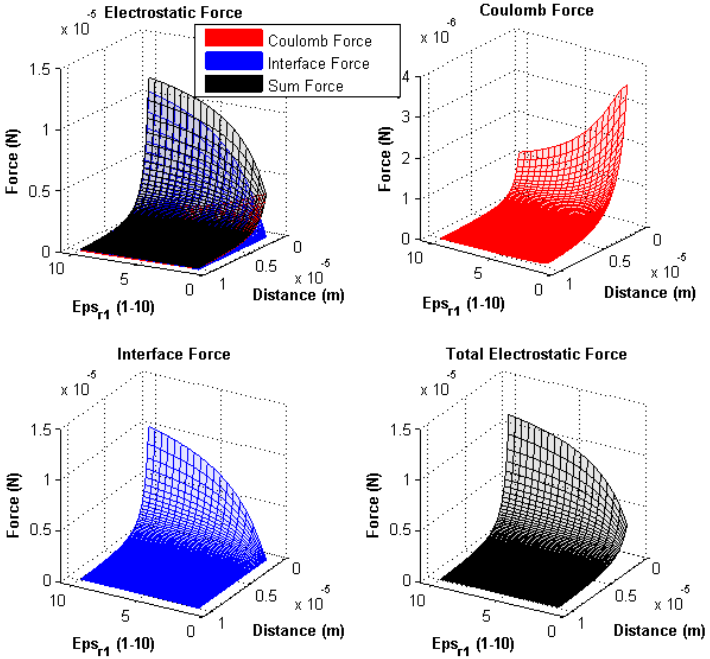

Figure 3-15: Electrostatic force components a.) with Coulomb force b.) interface force c.) and total electrostatic force d.).

3.5 Electromechanical Transducer (EMT) Element Model

This section deals with the implementation of the electromechanical transducer element TRANS126 of ANSYS. In the first part the element properties and functional principle is treated. The following part is about the implementation and the working principle. Finally the model used to investigate the electromechanical transducer is discussed in more detail.

3.5.1 Transducer Element TRANS126

The TRANS126 element is a reduced-order line element with two degrees of freedom for each node, translation for mechanical movements in x, y or z axis and the electric potential. It represents the capacitive response of the MEMS speaker as a function of deflection. According to the reduced-order element, the coupling takes part in the mechanical partial differential equation (PDE) directly on the right hand side via force. The transducer converts energy from an electrostatic domain into the mechanical domain. The input of this element is the gap between the nodes and the pre defined capacity, the output is an analog force based on the electrostatic force; hence it represents the capacitive response to a motion in one direction.
Assuming the single ended driving technology with an insulated back plate, the implementation is as follows.

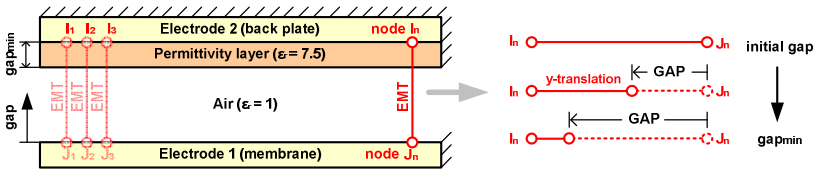

Figure 3-16: Electromechanical transducer element TRANS126 implementation principle.

Figure 3-16 displays an electrostatic speaker cell with the membrane as electrode one and back plate as electrode two. The EMT is connected between a node “J” on the membrane and a node “I” on the back plate. Hence, these are the two electrodes in the analogue electrostatic circuit diagram of the capacitor. As can be seen, the back plate is mechanically fixed and the membrane can move. The gap is defined along the y-axis starting at the initial gap where the membrane

is at initial state, to the minimum gap where the membrane is in contact with the insulation layer of the back plate. Elements can be combined to describe a full three dimensional translation of the speaker. In our case the geometry diameter is large compared to the stroke level; as a result the degree of freedom in displacement used is just the one in y-direction.

3.5.2 Implementation and Working Principle

The characteristics of the line element are derived from the CMATRIX macro [81]. By the help of this macro, the capacitance is computed via virtual work principle. Since the element represents the capacitive response of a mechanical deformation, the capacity is the important input parameter. There are two approaches to find the capacity to gap relation of an arbitrary geometry in ANSYS. First the use of CMATRIX, where a deformation or displacement is applied on the body and the capacity is read out for various gap distances and second, the manual implementation of the capacity to gap relation with analytical computations. Hence, the latter is used in our model because of the simple geometry of a plate type capacitor. The evaluation process of the capacitance to gap relation is displayed in Figure 3-17.

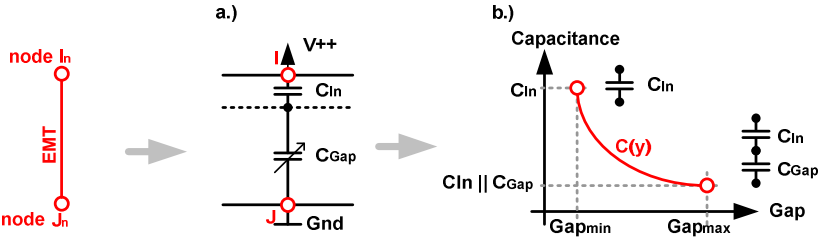

Figure 3-17: Electromechanical transducer element with a.) analogue capacity circuit diagram and b.) corresponding capacitance to gap relation (for an arbitrary element).

In a first step, a lumped element model is generated out of the defined gaps with its various dielectric layers, as depicted in Figure 3-17 b.). We see that, the insulation capacitance C_{In} is fixed and the gap capacitance C_{Gap} varies with the air gap. C_{In} can be computed with (3.38), C_{Gap} with (3.39) and the total capacitance with (3.40) as treated previously. Since the minimum capacitance occurs at $Gap_{\max}$ and the

maximum capacitance occurs at $Gap_{\min}$ as displayed in Figure 3-17c.), the capacitive response of the transducer element is defined by

$$C(y) = \frac{\lambda}{G_{\min} - G_0}, \tag{3.50}$$

where

$$G_0 = \frac{C_{\max} G_{\min} - C_{\min} G_{\max}}{C_{\max} - C_{\min}} \tag{3.51}$$

and

$$\lambda = C_{\max} (G_{\min} - G_0). \tag{3.52}$$

The initial gap or $Gap_{\max}$ value represents the initial distance between both electrodes and should fall within the range of the capacitance vs. stroke function. Since numerical derivations of polynomial functions are simpler to implement in comparison to reciprocal functions like capacitance to gap relations (3.50), the implementation in ANSYS has to be done with polynomial coefficients [81]

$$C(y) = \frac{C_0}{y} + C_1 + C_2 y + C_3 y^2 + C_4 y^3. \tag{3.53}$$

Hence, the capacitance $C(y)$ is described by displacement u_y and the five polynomial coefficients C_0 to C_4. For this purpose the coefficients are computed with

$$\begin{bmatrix} 1/U_1 & 1 & U_1^2 & U_1^3 & U_1^4 \\ 1/U_2 & 1 & U_2^2 & U_2^3 & U_2^4 \\ 1/U_3 & 1 & U_3^2 & U_3^3 & U_3^4 \\ 1/U_4 & 1 & U_4^2 & U_4^3 & U_4^4 \\ 1/U_5 & 1 & U_5^2 & U_5^3 & U_5^4 \end{bmatrix} \cdot \begin{bmatrix} C_0 \\ C_1 \\ C_2 \\ C_3 \\ C_4 \end{bmatrix} = [C(y_1) C(y_2) C(y_3) C(y_4) C(y_5)]^{\cdot} \tag{3.54}$$

or

$$\mathbf{A} \cdot \mathbf{x} = \mathbf{b}. \tag{3.55}$$

In (3.55), **x** donates the coefficients, **A** is the coefficient matrix and **b** are the analytically computed capacitances between $Gap_{\min}$ and $Gap_{\max}$ according to (3.50). As a result,

$$\mathbf{A}^{-1} \cdot \mathbf{b} = \mathbf{x} \tag{3.56}$$

returns the polynomial coefficients representing C(y). The electrostatic force of the TRANS126 element is computed by the energy stored in a linear capacitor, derived along the gap path

$$W_{\text{el}} = \frac{1}{2} C U^2 , \tag{3.57}$$

which results in [71]

$$F_{\text{el}} = \frac{\partial W_{\text{el}}}{\partial u_{\text{y}}} = \frac{1}{2} \frac{\partial C(y)}{\partial u_{\text{y}}} U^2 . \tag{3.58}$$

We see that the electrostatic force F_{el} is proportional to voltage squared U^2 and the derivative of the capacitance. To account for a correct electrostatic force result, the derivation of the fitted capacitance (according to (3.56)) and the analytical solution (according to (3.50)) must match. TRANS126 elements compute the derivative of the capacitance to gap relation, therefore the gradient is important. The gradient increases rapidly near $Gap_{\min}$ and for geometries with high permittivity or thin insulation layer. This is a direct result of a large ration between maximum and minimum capacitance.

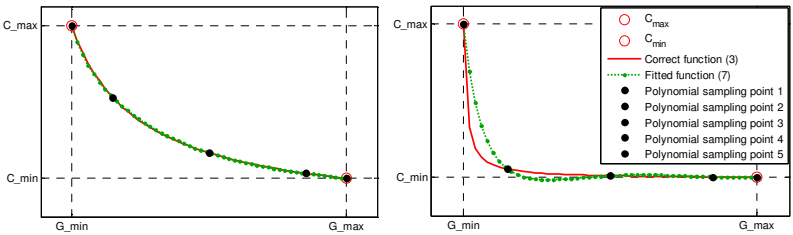

Figure 3-18: Gap versus capacitance relation of analytically computation according to (3.50) compared to the implemented polynomial response of the EMT element according to(3.53). Left side shows a valid fitting example and right side a result with oscillations.

Figure 3-18 displays the gap versus capacitance ratio according to the implemented polynomial function and the analytically function. Important to mention: Each EMT element owns an individual gap versus capacitance relation, because of the axis rotational model. The left side of Figure 3-18 displays a well fitted function with low gradient profile; the deviation between both computations is negligible. The right side of Figure 3-18 displays a large gradient near Gap_{min}, furthermore the polynomial fit starts to oscillate around the five sampling points. In this case the results must be checked carefully; hence the force is computed with the derivative of the oscillating polynomial function. The oscillations can lead to alternating signs for the attracting electrostatic force.

3.5.3 The EMT Model

This section discusses a possible TRANS126 implementation in ANSYS. The implementation process starts with the geometrical model. We used a simple plate type capacitor with two electrodes, one is the membrane and one is the back plate. The back plate is coated with a SiNi layer for electrical insulation. The electromechanical transducer (EMT) elements are defined between the conducting electrodes. The setup is displayed in Figure 3-19. The left side depicts the Gap_{max} case and the right side the Gap_{min} case, where mechanical contact occurs.

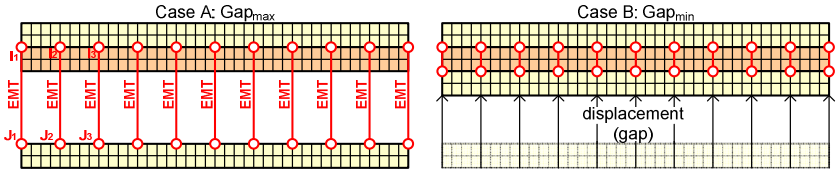

Figure 3-19: Principal setup of EMT implementation between membrane and back plate.

The degree of freedom in our case is the y-axis, therefore all EMT elements are aligned in parallel along this axis. Since the "I_n" (on top side) and "J_n" (on bottom side) nodes have to be chosen manually, the element distribution or density along the radius (x-axis) can be chosen manually too. It is not required to define the EMT on each element along the radius. Tests have shown that simple geometries can deal without worsening the results up to a factor of 50:1 – each 50th element along the radius is connected with one EMT element. But at least 20

elements are required in total. As mentioned before each element owns its specific capacitance to gap relation, which is a result of the axis rotational geometric model. The implementation loop over all elements is displayed in Figure 3-22 in detail. In the first step the area linked to the element is computed. In our case the top nodes x-axis offset is used to determine the distance between two TRANS126 elements and compute the area

$$A = \pi\left(r_2{}^2 - r_1{}^2\right). \tag{3.59}$$

As can be seen in Figure 3-20 the TRANS126 element is located in the middle of the two nodes. The offset is considered in the computation by choosing the correct radius for both nodes. In this model we use the top nodes to compute the area, because they are not mechanically deformed. In case of mechanical deformation, as it is shown for the bottom electrode in Figure 3-20, the distance between r_1 and r_2 must be computed regarding to Pythagoras. The discretization error between true deformation and linear approximation is negligible, because of the large diameter to stroke level ratio.

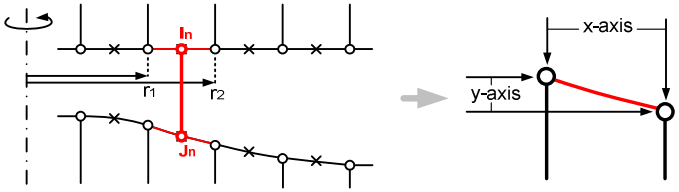

Figure 3-20: TRANS126 element with corresponding area.

In the next step the initial gap or G_{max} value is computed. In this step the distance between node I_n and J_n is determined with the nodal coordinates. Since the top node and the bottom node feature the same x-value no special case must be considered, except the bottom node J_n is located above the top node I_n, which results in an invalid element state and invalid contact state. The gap definition is displayed in Figure 3-21.

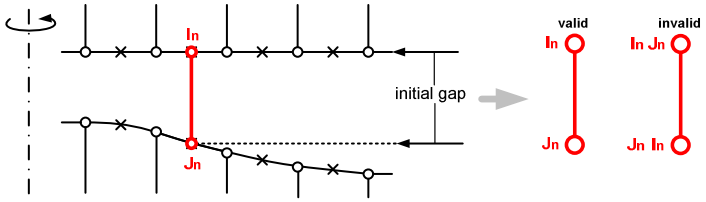

Figure 3-21: TRANS126 element with corresponding initial gap.

In the next step of the TRANS126 element implementation loop, the key capacitances are computed by (3.57) representing the maximum capacitance in contact case at Gap_{min} and (3.59) representing the minimum capacitance at Gap_{max} or initial gap. At this point all necessary capacitances and gaps are known to determine the capacity to gap relation for this element as depicted before in Figure 3-17 and Figure 3-18.

For fitting the polynomial function with the C(y) function, the sampling points are chosen with the following restriction:

- the gradient of the fitted function must be constantly negative and
- the deviation error must be as small as possible.

The sampling point computation is not treated in detail in this report; hence MATLAB fitting toolbox was used to determine these five points automatically. Investigations on our geometry have shown good fitting results with sampling points chosen manually by:

$$Gap_{min}\ (0\%),\ 40\%,\ 60\%,\ 80\%\ \text{and}\ Gap_{max}\ (100\%).$$

In the last routine the computed parameters are set to the EMT element. The loop includes each EMT except the last one ($1{:}n_{EMT\text{-}1}$). This element is not considered in our model, because it is located next to the speakers housing and can be neglected due to low mechanical deformation possible of this region.

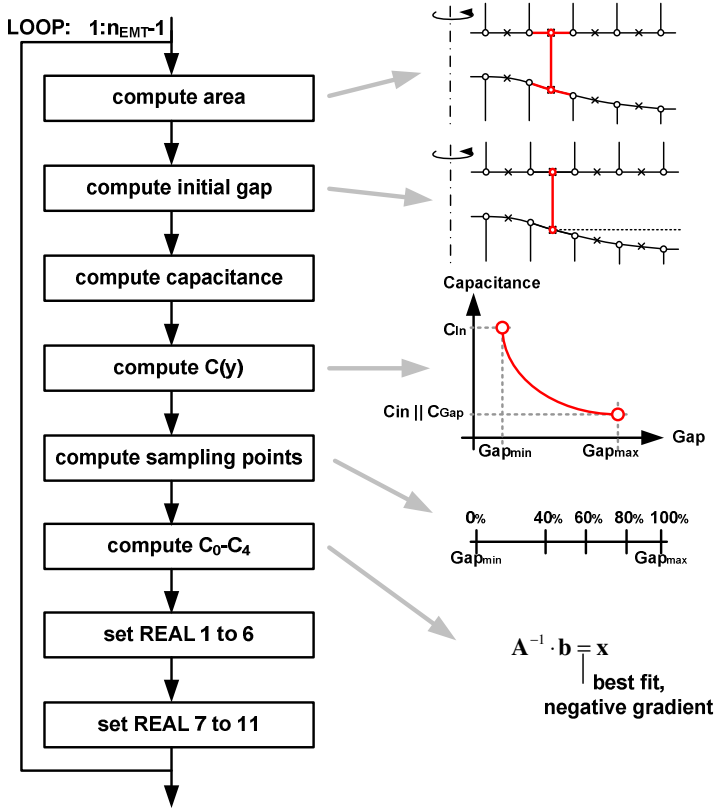

Figure 3-22: Implementation loop of EMT elements (ANSYS APDL specific).

3.6 Multi-Field Model

This section deals with the implementation of the multi-field interaction between electrostatics and mechanics. In the first part, the functional principle including the coupling and load transfer is explained. The following part is about the implementation and the

working principle. Finally the implementation on a simple model is discussed.

3.6.1 Multi-Field Coupling

The multi-field analysis combines the effects of multiple interrelated physical phenomena. In our case we couple the electrostatic field with the structural mechanical field as depicted in Figure 3-23.

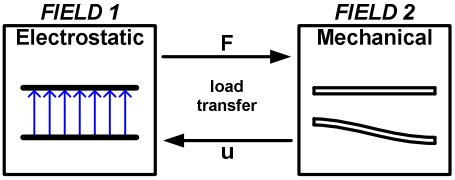

Figure 3-23: Schematically coupling between electrostatic field and mechanical field.

Each field is represented by its own physical interpretation using a partial differential equation (PDE). The strong formulation of the electrostatic field is written as

$$-\nabla \cdot \varepsilon \nabla \varphi_{\mathrm{e}} = q_{\mathrm{e}} \,, \tag{3.60}$$

where φ_{e} represents the electric scalar potential, q_{e} the electric volume charge and ε the permittivity. The strong formulation of the mechanical field is written as

$$\mathrm{B}^{T}[c]\mathrm{B}\vec{u} + f_{\mathrm{v}} = \rho \frac{\partial^2 \vec{u}}{\partial t^2} \,. \tag{3.61}$$

A detailed derivation of (3.60) and (3.61) can be found in [46]. All nonlinearities of the involved fields must be taken into account separately. The mechanical field shows nonlinearities for large deformation as well as stress stiffening and contact can occur. The coupling between these fields can be direct or sequentially, where in general the direct method uses special elements with multi-field degree of freedom and the sequential method performs multiple single field analysis with load transfer conditions between them. If the PDEs of the single fields are linear, the coupled system is still nonlinear because of the coupling mechanism. In our case the multi-field model is defined by

the electrostatic field and the structural field coupled sequentially with conservative load transfer. The semi discrete Galerkin formulation of coupling between electrostatic and mechanical field can be written as

$$\begin{bmatrix} \mathbf{K}_{11}(\mathbf{u}_m, \varphi_{el}) & 0 \\ 0 & \mathbf{K}_{22}(\mathbf{u}_m) \end{bmatrix} \begin{Bmatrix} \mathbf{u}_m \\ \varphi_{el} \end{Bmatrix} = \begin{Bmatrix} \mathbf{F}_1(\mathbf{u}_m, \varphi_{el}) \\ \mathbf{F}_2(\mathbf{u}_m, \varphi_{el}) \end{Bmatrix}, \tag{3.62}$$

where the first line represents the structural field and the second line the electrostatic field. In this case $\mathbf{K}$ represents the stiffness matrix, $\mathbf{u}_m$ the unknowns for mechanical displacements, φ_{el} the unknowns for electric potential and $\mathbf{F}$ the applied load vector. In this example the load transfer takes place on the right hand side via forces. Since conservative load transfer is modeled the equilibrium of forces is fulfilled. As can be seen in Figure 3-23, the electrostatic force results in a mechanical deformation of the structure and the deformation results in an electrostatic field change. So a two ways coupling is modeled for the MEMS speaker device.

3.6.2 Implementation and Working Principle

There are basically two loop conditions for solving a multi-field problem as depicted in Figure 3-25. The first loop solved in the simulation process is the field loop, where the PDE of the first physical field is solved initially. In our case the electrostatic field is field number one and the electrostatic force is computed according to (3.44). If the electrostatic force is computed, the result is transferred via conservative load transfer to the nodes of the second field. In our case the mechanical model represents the second field. In the mechanical model the electrostatic force results in a mechanical deformation of the membrane. The displacement characteristics are determined by the external force of the load transfer and the internal forces of the structure itself. Mechanical deformation is computed nonlinear, because of large deformation and various layers with different initial pre-stresses, which results in stress stiffening effects. The second field loop computes the mechanical deformation, therefore the mesh between the electrodes is distorted. At this point mesh morphing must be used, to avoid distorted elements, also re-meshing the computational domain for field one can be applied. Updating the electrostatic mesh with the mechanical displacements is necessary, to compute the electrostatic field on the updated geometry. If both field loops converge with their loads transferred between them, the next time step starts.

In ANSYS the equation of motion is extended with an equivalent electrostatic stiffness matrix [71],

$$\mathbf{Mu}+\mathbf{Cu}+\mathbf{Ku}=\mathbf{F}_{\mathrm{el}}\,, \tag{3.63}$$

where

$$\mathbf{F}_{\mathrm{el}}=\mathbf{K}_{\mathrm{el}}\,\mathbf{u}\rightarrow\frac{\partial F_{\mathrm{el\,i}}}{\partial u_{\mathrm{j}}}=\frac{U^2}{2}\frac{\partial^2 C_{ij}}{\partial y^2}\,. \tag{3.64}$$

Hence (3.63) can be written as

$$\mathbf{Mu}+\mathbf{Cu}+(\mathbf{K}-\mathbf{K}_{\mathrm{el}})\mathbf{u}=0\,. \tag{3.65}$$

We see that the electrostatic stiffness leads to soften the structure. Furthermore the displacements increase for a given force and the eigenfrequencies decrease.

Load are transferred between the interfaces of the mechanical and electrostatic fields. In our case we use conservative load transfer conditions where the total nodal result of field one is mapped on the interface nodes of physical field two. This process is displayed in Figure 3-24.

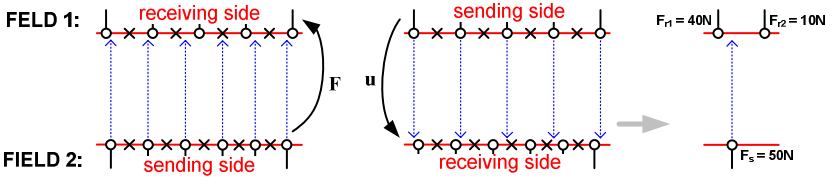

Figure 3-24: Conservative load transfer on interface between physical field one and two and schematically interpolation.

Each node in the sending side maps to an element on the receiving side. The transferred force is interpolated to the nodes of the mapped element in the receiving side, therefore a finer mesh on the sending side is recommended. The total force sent is equal to the total force received and vice versa.

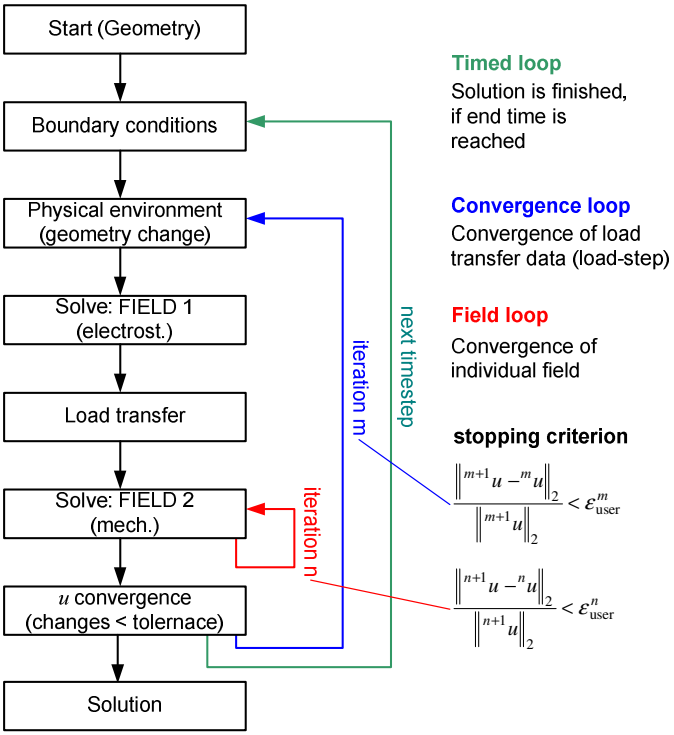

Figure 3-25: Simulation flowchart of a multi-field solving process.

Another important point is the mesh morphing method as mentioned before. A deformation of the mechanical structure in the electrostatic field will lead to wrong results, if the electric field is not adapted on the structural field interactions. Therefore, the electric field needs an additional mechanical degree of freedom to be able to handle the mechanical morphing deformation. Mechanical interactions between the mechanical properties of the morphing mesh and the mechanical field are avoided with setting the morphing stiffness very low compared to the structural body's stiffness. By the help of the mesh morphing technique the total mechanical deformation is transferred to the electric field [61, 71]. A schematically overview of this mesh morphing technique is given in Figure 3-26, where on the left side the mechanical field does not interact with the electrical field and element intersections

occur, while on the right side the mesh morphing technique is applied and the electric field matches the structural field.

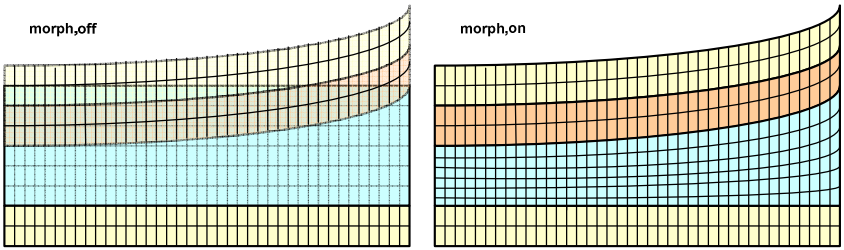

Figure 3-26: Electric field and mechanic field without (left) and with (right) mesh morphing technique.

3.6.3 The Model

For evaluation process and comparing the multi-field model to the TRANS126 element model, the same physical dimensions and material parameters were used. In this method the air between the electrodes is modeled additionally to the structural model; both PDEs are solved with FEM with a sequential algorithm. The model setup is depicted in Figure 3-27, where the top electrode is insulated with a SiNi layer. As in the EMT model, a voltage is applied between the electrodes, which results in a mechanical deformation and the gap between the insulation layer and bottom electrode gets smaller. The challenge is the snap-in case, where the membrane is in contact with the insulation layer, hence the air elements are even distorted to zero volume. This effect is described in a previous work in more detail [48]. To bypass distortional element a forward contact region must be included in the model. The normal stiffness of the contact region is a parameter, linked with the penetration depth. The higher the normal stiffness, the lower the penetration depth, but the higher the computational effort; in our case the forward contact region accomplishes the purpose of distorted air elements and not the purpose of a mechanical solid to solid contact, thus the normal stiffness can be set very low to reduce the computational time.

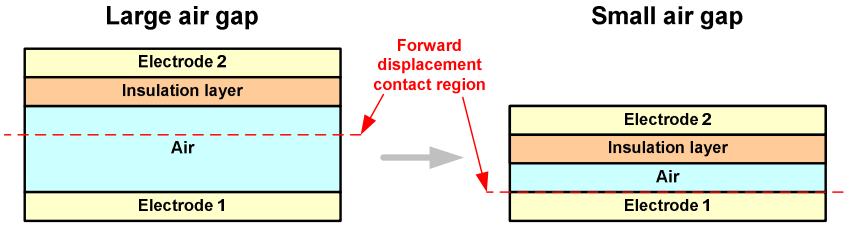

Figure 3-27: Multi-field finite element model setup with large air gap (initial state) and small air gap (contact state) at forward displacement contact region (dashed line).

In addition to the forward displacement contact region, mesh morphing technique was used to adapt the electric field mesh to the deformed structural field between the insulation layer and bottom electrode.

As depicted in Figure 3-28, there are two physical fields describing the fully coupled model. First the structural model for mechanical behavior and second the electrostatic model for computing the electrostatic field and as a result the force affecting the structural model. Force and displacement are transferred via fluid structure interaction (FSI), where the structural part is represented with the structural model and the fluid part within the electrostatic model (air and permittivity layer). The results from field one are transferred as load to field two and vice versa, hence this is a sequentially coupled field simulation with two way coupling characteristics. Electrostatic structural models typically have two ways coupling, because the structural deformation affects the electrostatic field – therefore mesh morphing is important. The huge disadvantage of the multi-field model is the snap-in case, where air elements are distorted to zero. The forward displacement contact region is a workaround of this special case, but no proper solution.

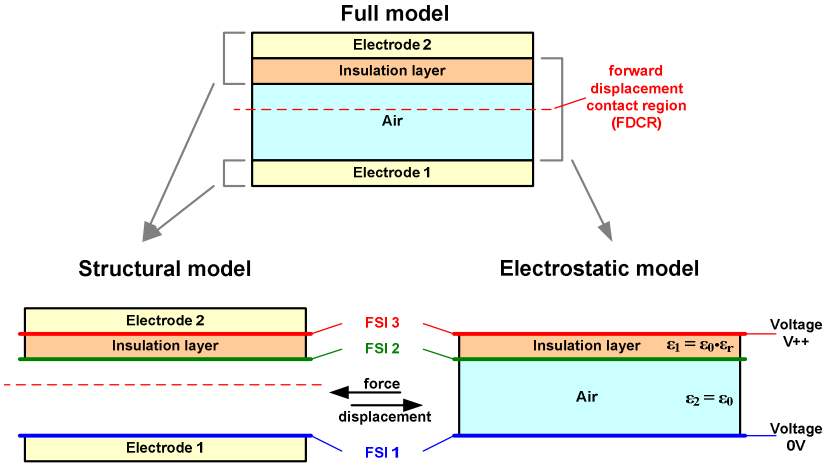

Figure 3-28: Structural model with mechanical properties of electrode one, two and insulation layer (left) and electrostatic model with electrostatic properties of insulation layer and air (right), coupled via fluid structural interaction (FSI) layer for each layer.

3.7 Results

This section deals with the simulation results of the TRANS126 element model, the multi-field model and the analytical computation. In the first part the capacitance versus gap relation and the computed electrostatic force is represented.

3.7.1 Analytic vs. EMT vs. Multi-Field Model

As described before, there are two possibilities to model the electrostatic-mechanical coupling in ANSYS. First the electro-mechanical transducer, where the capacitance to gap relation (see (3.53) or (3.55)) is used to compute the attracting electrostatic force. Second the multi-field approach, where the electrostatic force is computed according to (3.44). Both methods use virtual work method. A comparison between these two models is given in Figure 3-29, where the

analytic solution is obtained from (3.49). In the first row of Figure 3-29, the electrostatic force versus gap relation is depicted for increasing permittivity in the insulation layer. In the second row, the capacitance versus gap relation for increasing the permittivity in the insulation layer is depicted.

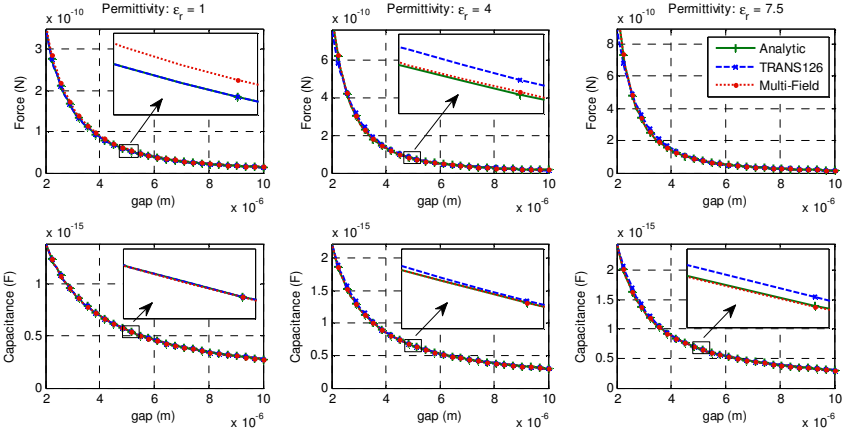

Figure 3-29: Comparison between TRANS126 model, multi-field model and analytic solution for different permittivity ratios, concerning to capacitance and electrostatic force versus gap displacement.

The gap starts at 10 µm and ends at 2 µm, exactly 1 µm above the snap-in. This is a direct result of the multi-field model in combination with the forward displacement contact region. The analytical solution and the EMT model would be able to close the gap, but the multi-field model limits this test. We see the force and capacity versus gap results, of the three models match for this setup. Due to the fact, that the maximum capacitance in this test case is smaller compared to maximum capacitance possible at the contact case, the TRANS126 polynomial fitting works very well. To outline the effect of the maximum capacitance and the polynomial fitting problem, the mechanical transducer element model was crosschecked with the analytical solution for contact case as depicted in Figure 3-30.

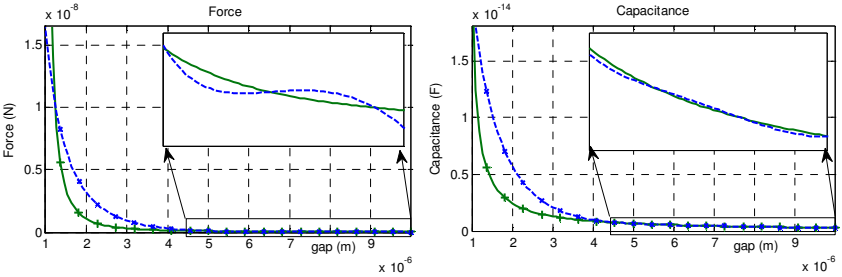

Figure 3-30: Comparison between EMT model and analytic solution for contact conditions (snap-in).

On the left side, the force versus gap relation is displayed, where the solid line represents the analytical result and the dashed line the TRANS126 output. The right side of Figure 3-30 displays the capacitance versus gap relation. For this investigation a negative slope condition was used in the fitting algorithm to avoid oscillations. Therewith, the oscillations can be strongly reduced, but are still present for the force versus gap relation due to the derivation relation. Additionally we see the gradient of force at the contact case (1 µm). This gradient is essential for modeling mechanical contact and accuracy of penetration. As mentioned before, the higher the force gradient, the higher the normal stiffness of contact properties and the higher the computational effort.

For accurate results based on complex deformations, the multi-field model is the best choice, but shows restrictions for contact case (forward displacement contact region) and the amount of elements as well as the computational time is higher compared to the TRANS126 element model. The electrostatic force is computed via virtual work method which takes permittivity variations into account. The TRANS126 model is accurate for single permittivity layers and low C_{max} to C_{min} ratios (thicker insulation layer) and can be used for simple geometries without complex nodal displacements. The resulting force is computed of the derivation of the capacity as defined with a polynomial function, which is not the best fitting option but easy to derivate numerically, hence it is implemented in ANSYS.

NOTE: There is an option at the TRANS126 element to set the capacitance to gap relation without computing the polynomial coefficients concerning to (3.56). This option can be switched with

KEYOPT(3) and the capacitance to gap relation can then be set with 20 data points. For the overall result, nothing changes; because an internal fitting algorithm computes a piece wise linearized capacitance to gap relation the missing polynomial coefficients and the electrostatic force results look the same – oscillations and different force gradient at the contact. Indeed, the manual polynomial coefficient computation yields to better electrostatic force results, because of the additional fitting options like *negative gradient* and *overall best fit*.

3.7.2 Snap-In of EMT and Multi-Field Model

For the snap-in evaluation, the multi-field model was used as reference system due to the results of Figure 3-29. The multi-field model cannot be driven in full snap-in mode with mechanical contact between the membrane and the back plate; this is a direct result of the air elements as mentioned before. For this test, the forward displacement contact region (FDCR) was placed slightly after the snap-in point (38 % of total gap) as can be seen in Figure 3-31. Therefore the EMT element minimum gap distance for the contact region was set on the same level. In this test, the voltage applied is linearly increasing from zero to snap-in voltage (100%) plus ten percent (110%).

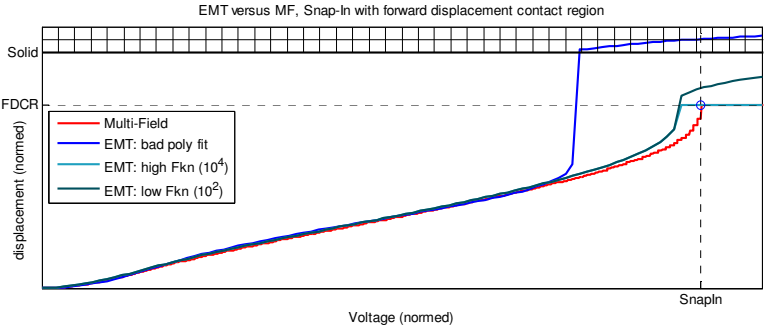

Figure 3-31: Snap-In model investigation between multi-field model (as reference) and EMT model. Membrane displacement under applied voltage up to snap-in plus 10%.

To optimize the visualization of the membrane motion and the snap-in point, mechanically tensile pre-stress was reduced to 1 % in the model – the membrane is soft. The slope named "*EMT: bad poly fit*" displays a bad polynomial fit as it was treated before in Figure 3-18 (right). The

electrostatic force of the EMT model is higher compared to the analytically derived force, at the forward displacement contact region. As a result, the snap-in occurs at lower voltage levels applied. Due to the high gradient of the capacity to gap relation and therefore high electrostatic forces at the Gap_{min} point (see Figure 3-30), penetration between the membrane and the insulation layer occurs, even the forward displacement contact region is penetrated fully. The slope named "*EMT: low Fkn (10^2)*" represents a well capacity to gap polynomial fitting as depicted in Figure 3-18 (left). As can be seen very well, the snap-in point is determined more accurately with better polynomial fitting results. In this model, we set the normal contact stiffness factor low with 10^2 and increased the voltage with ten percent. As a result, the electrostatic force and the counteracting contact spring force are in equilibrium state of forces and visible penetration occurs. By adjusting this parameter, the penetration depth can be defined. The higher the normal contact stiffness factor, the lower the penetration depth. The last slope named "*EMT: high Fkn (10^4)*" displays a high normal contact stiffness factor of 10^4, where the penetration at the forward displacement contact region is almost zero.

CHAPTER 4

4 Acoustic Field Modeling

In this chapter the acoustic field computed with FEM are discussed. The coupling between mechanical and acoustic field is treated with respect of the mesh generation for the fluid structure interface. Mortar FEM using non-conforming grids is used to adapt the fine mechanical mesh to the coarser acoustical mesh, by concurrently getting rid of distorted elements and reduce the amount of elements in total. Two methods to model open domain characteristics and truncate the propagation region are discussed. Additionally, the Kirchhoff Helmholtz integral solution of the wave equation is presented as an alternative sound pressure level (SPL) computational tool. In the last part of this section, FEM and Kirchhoff Helmholtz (KH) results are compared with measured SPLs.

4.1 Acoustic Basics

We consider linear acoustics, and therefore longitudinal waves, where the particles in the media are only able to move back and forth towards the propagation. In this case, the driving mechanism is the pressure gradient. Figure 4-1 displays a wall moving forward and backward (piston moving solid). A microphone records the particle density at the point of interest (POI).

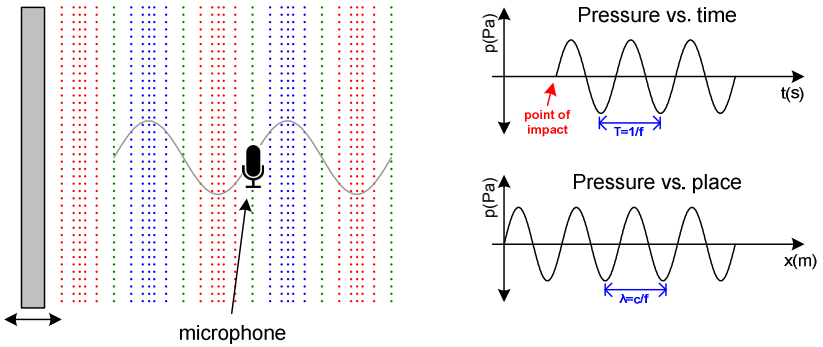

Figure 4-1: Particle density of longitudinal wave propagation.

The wavelength λ is the ratio between the speed of sound c in specific media and the frequency f of the signal. The human auditory is able to sense wavelengths between 17.15 m (20 Hz) and 17.15 mm (20 kHz)

$$\lambda = \frac{c}{f}. \tag{4.1}$$

Wave propagation is a physical property of the media; therefore it is linked with several environmental factors like temperature, density or humidity. The most influencing factor on speed of sound is the temperature as can be seen in Figure 4-2. The computations for this slope was made by a linear assumption in a temperature range of -20 °C to +40 °C by

$$c_{air} \approx 331.5 + 0.6 \cdot T_{(°C)} \tag{4.2}$$

The accuracy of (4.2) is about 0.2 % for this temperature range as described in [82]. More information of environmental factors, like humidity influencing the speed of sound can be found in [83].

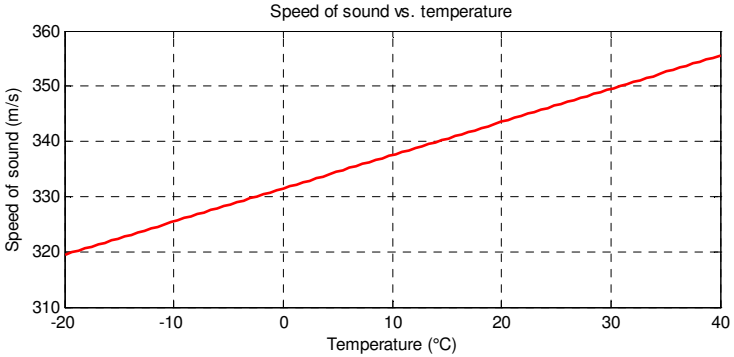

Figure 4-2: Environmental influence of temperature on speed of sound in air.

The major factors describing wave propagation are density, pressure and velocity. These quantities are the sum of a mean part and an alternating part. For linear acoustics, the alternating part is small in comparison to the mean part:

Density:	$\rho = \rho_0 + \rho'$	where:	$(\rho' << \rho_0)$
Pressure:	$p = p_0 + p'$	where:	$(p' << p_0)$
Velocity:	$\vec{v} = \vec{v}_0 + \vec{v}'$	where:	$(\vec{v}' << \vec{v}_0)$

The mean density ρ_0 value of air is about 1.2041 m³/kg [84]. The alternating pressure p' is superimposed by the atmospherically pressure p_0, which is 101325 Pa or 1013.25 mbar at sea-level [84]. The mean value of particle velocity v_0 is zero, until an ambient flow occurs or the object moves. For acoustic computations over large distances, these effects have to be taken into account by modeling the acoustic wave propagation. The MEMS micro speaker field of application is designed to fill small areas with sound; therefore the mean parts of physical quantities can be neglected and linear acoustics can be applied.

4.1.1 Acoustic Wave Equation

Acoustic waves in non-viscous media propagate as longitudinal waves. The linear acoustic computational domain is fully described by the

conservation of mass (4.3), conservation of momentum (4.4) and finally the state equation(4.5).

- Conservation of mass:

$$\nabla(\rho_0 \vec{v})' = -\frac{\partial \rho'}{\partial t} \tag{4.3}$$

- Conservation of momentum:

$$-\nabla p' = \rho_0 \frac{\partial \vec{v}'}{\partial t} \tag{4.4}$$

- State equation:

$$\frac{p'}{\rho'} = c^2 . \tag{4.5}$$

By combining (4.3), (4.4) and (4.5) the result is known as wave equation. In general expression, this equation is also known as d'Alembert equation [85, 86]

$$\frac{1}{c^2}\frac{\partial^2 \psi}{\partial t^2} = \Delta \psi . \tag{4.6}$$

The field Ψ can be replaced by pressure p' or the acoustic velocity potential φ. Hence we get the pressure (4.7) and potential (4.8) formulation of the general wave equation by

$$\frac{1}{c^2}\frac{\partial^2 p}{\partial t^2} = \Delta p \tag{4.7}$$

$$\frac{1}{c^2}\frac{\partial^2 \varphi}{\partial t^2} = \Delta \varphi . \tag{4.8}$$

4.1.2 One Dimensional Example

By assuming a wave, excited at coordinate system origin, the solution of the wave equation is a wave "a" moving in positive x-direction and a wave "b" moving in negative x-direction. All assumptions are also valid for y-direction and z-direction, if the media is homogeneous and the source is a point source. Therefore the problem can be reduced to a one dimensional case (only x-direction), for better understanding.

$$p'(x,t) = a(t - x/c) + b(t + x/c). \tag{4.9}$$

There is also the possibility to express (4.9) by an exponential ansatz as often used in literature [87].

$$p'(x,t) = \hat{p}\, e^{i(\omega t - kx)} = \hat{p}\, e^{i\omega t} e^{-ikx} \tag{4.10}$$

Here, the first term describes the space dependent solution and the second term stands for the time dependent part of the solution. The wave number k describes the relation between frequency f and sound propagation speed c by

$$k = \frac{\omega}{c} = \frac{2\pi f}{c}. \tag{4.11}$$

4.2 Mechanical-Acoustic Coupling

If a solid is moving in a fluid it generates sound, caused by the normal component of its surface vibration velocity [46]. In this case, the moving solid is the membrane and the fluid is the surrounding air. A general setup for a solid-fluid interface can be seen in Fig. 4-3. The red colored surface lines are able to generate acoustic waves by their normal components.

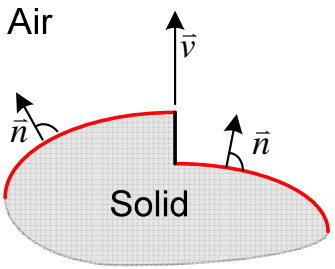

Figure 4-3: Solid-fluid interface for mechanical-acoustic coupling.

By integrating the wave equation over the computational domain Ω and multiplying it with a test function ω, we get the weak form of the PDE

$$\int_{\Omega} \omega \cdot \frac{1}{c^2} \frac{\partial^2 \varphi}{\partial t^2} d\Omega - \int_{\Omega} \omega \cdot \Delta \varphi \, d\Omega = \int_{\Omega} \omega \cdot f \, d\Omega \,. \tag{4.12}$$

To include the coupling terms and boundary conditions, (4.12) is integrated by the help of Green's theorem, which leads to

$$\int_{\Omega} \omega \cdot \frac{1}{c^2} \frac{\partial^2 \varphi}{\partial t^2} d\Omega + \int_{\Omega} \nabla \omega \cdot \nabla \varphi \, d\Omega - \oint_{\Gamma} \omega \frac{\partial \varphi}{\partial n} d\Gamma = \int_{\Omega} \omega \cdot f \, d\Omega \,. \tag{4.13}$$

Hence, the normal derivative of acoustic scalar potential represents the surface velocity of the moving membrane or in more general case, of a moving solid. This boundary condition describes the normal derivative of the acoustic potential as forward coupling and defines the natural or Neumann boundary condition

$$-\frac{\partial \varphi}{\partial n} = \vec{v} \cdot \vec{n} = v_n \,. \tag{4.14}$$

Since the acoustic particle velocity is irrotational, it can be expressed by the gradient of the scalar acoustic vector potential φ.

$$\vec{v}' = -\nabla \varphi \,. \tag{4.15}$$

Furthermore, to obtain the relation between acoustic pressure and the acoustic potential, (4.15) has to be combined with (4.4)

$$\nabla p' = \rho_0 \frac{\partial}{\partial t} \nabla \varphi \rightarrow p' = \rho_0 \frac{\partial \varphi}{\partial t} \,. \tag{4.16}$$

The result of the electromechanical simulation is the membrane displacement $\vec{u}$, which can be used directly as input parameter for acoustic simulations. As already used in (4.14), the normal component of the surface velocity is related to the acoustic potential. In a fully coupled system, the ambient air (or fluid) can cause mechanical stress, acting like a pressure load against the normal component. Hence, the backward coupling is given as

$$-\vec{\sigma}_n = \vec{n} p' = \vec{n} \rho_0 \frac{\partial \varphi}{\partial t} \,. \tag{4.17}$$

Since the surface velocity of the membrane is forcing each air particle to move with the same normal component velocity, the following relation can be assumed by considering (4.4)

$$\frac{1}{\rho_0}\frac{\partial p'}{\partial n} = -\frac{\partial^2 u_n}{\partial t^2}. \tag{4.18}$$

It can be seen that the normal component of the second derivative of the moving solid (the acceleration) is linked with the acoustic pressure. The fully coupled field formulation and derivation can be found in [46] in more detail. Just to give a brief overview the weak formulation for mechanical and acoustics are as follows:

- Weak formulation of mechanical PDE:

$$\int_{\Omega_M} \bar{\omega}_M \cdot \rho \frac{\partial^2 \vec{u}}{\partial t^2} d\Omega_M + \int_{\Omega_M} (B\bar{\omega}_M)^T [C] B\vec{u}\, d\Omega_M - \oint_{\Gamma} \bar{\omega}_M \cdot \vec{\sigma}_n\, d\Gamma = \int_{\Omega_M} \bar{\omega}_M \cdot \bar{f}_v\, d\Omega_M \tag{4.19}$$

- Weak formulation of acoustic PDE:

$$\int_{\Omega_A} \omega_A \frac{1}{c^2}\frac{\partial^2 \varphi}{\partial t^2} d\Omega_A + \int_{\Omega_A} \nabla\omega_A \cdot \nabla\varphi\, d\Omega_A + \oint_{\Gamma_{in}} \omega_A \vec{n} \cdot \nabla\varphi\, d\Gamma_{in} - \oint_{\Gamma_{out}} \omega_A \vec{n}_{out} \cdot \nabla\varphi\, d\Gamma_{out} = 0 \tag{4.20}$$

In (4.20), Γ_{in} represents the interface with solid-fluid coupling and Γ_{out} represents the outer boundary region of the acoustical domain.

4.3 Single Speaker Modeling with FEM

Only small arrays up to 16 speaker elements in total were modeled with FEM, due to computational costs. The challenge for modeling the MEMS micro speaker with FE method is given by the small membrane size and the large propagation region. Tests on the MEMS structure have shown, that at least three elements (at linear basis function) are needed to discretize the thickness of the membrane. Two elements lead to locking effects and four elements improve the accuracy only slightly. Information about locking effects in FEM can be found in [46, 88]. As a result, the membrane thickness defines the element size for the acoustic mechanical interface, because a total deformation ratio of the element should not get higher than 1:10 ratio. This directly leads to the first challenge, the amount of elements for the acoustical computational domain or a tradeoff between amount of elements and distortion rate. For acoustic domain discretization the smallest wavelength has to be

discretized at least by ten linear finite elements. Various tests have shown that a discretization of the wavelength by 20 in combination with linear basis functions show the best results. To give a thumb of rule according to [57], the discretization size should be in the range of

$$\frac{c}{f_{\max} \cdot 10} \leq h \leq \frac{c}{f_{\max} \cdot 20}. \tag{4.21}$$

For transient simulations, time steps have to be chosen in the same range as the spatial discretization

$$h = \frac{\lambda}{20} = \frac{c}{f_{\max} \cdot 20} \quad ; \quad \Delta t = \frac{T}{20} = \frac{1}{f_{\max} \cdot 20}. \tag{4.22}$$

An investigation of the ratio between time discretization and spatial discretization can be found in [46].

The second challenge is defined by truncating the acoustical computation domain. Setting the pressure level to zero at the boundary region, would lead to a soft wall condition (0 degree phase shift at reflection) and reflect the wave. Therefore perfectly matched layers (PLM) or absorbing boundary conditions (ABC) were used.

4.3.1 Mech.-Acou. Interface and Propagation Region

In the acoustic region, the membrane movement generates an acoustic wave which is propagated. As explained before in (4.21) and (4.22) the mesh size has to be adapted to the acoustic field. Since the mechanical model shows element sizes in the scale of nanometer the acoustic field discretization is in orders of magnitude larger. Therefore, we have to deal with two main problems concerning proper mesh generation. First, free meshing the MEMS speaker domain between the membrane and the point of interest, leads to extremely distorted elements in the acoustic region and second, keeping the distortion ratio below 1:10 would lead to an extraordinary amount of elements in total. By the help of Mortar FEM using non-conforming grid technology both problems can be avoided. The junction between the mechanical interface and the acoustic propagation region was realized with stepwise adapting the element size by factor 1:10 for each non-conforming grid shell. The mechanical interface defines the smallest grid and the perfectly matched layer used to model open domain characteristics (see section 4.3.2) defines the largest (coarsest) grid.

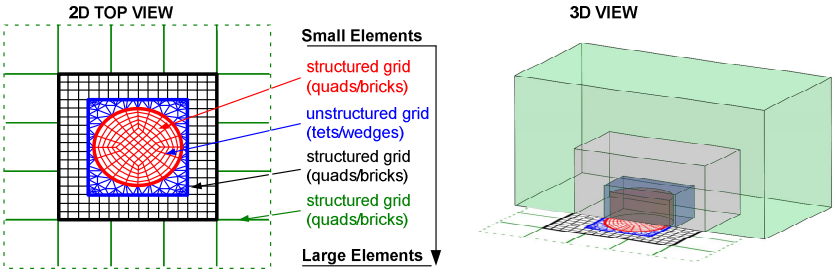

Figure 4-4: Non-conforming grids for mechanical acoustic interface.

The system can be compared to "Matryoshka" the famous Russian doll, where a larger doll is put over a smaller doll and so on. We found out that the best tradeoff between amount of elements and mesh size adaption level is at five "dolls" or encasing structures. Figure 4-4 displays the mechanical acoustic interface region of the membrane and the first three encasing structures. By the help of this method the amount of elements is reduced as well as structured grid can be used almost over the whole computational domain. As mentioned before, special boundary conditions as ABC or PML are used to truncate the acoustic propagation region. The encasing structures as well as the mechanical acoustic interface and the perfectly matched layer are displayed in Figure 4-5.

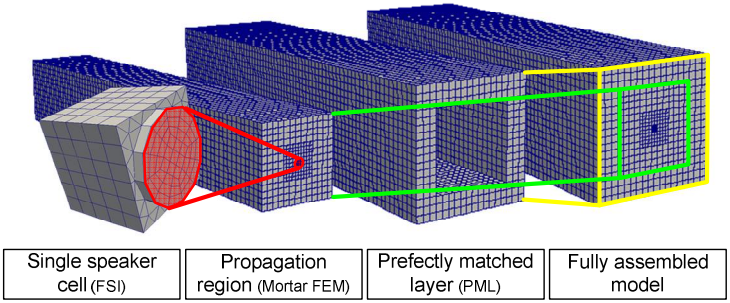

Figure 4-5: Mechanical acoustic model with single speaker cell and fluid structure interface (FSI), encasing propagation region assembled with Mortar FEM and PML to model open domain characteristics.

Further information on Mortar FEM with non-conforming grids can be found in [89, 90]. Large arrays of speaker cells as well as large propagation regions result in expensive computations. Therefore, Kirchhoff Helmholtz integral solutions are applied to compute the sound pressure level at any point of interest (POI).

4.3.2 Open Domain Modeling (ABC/PML)

As mentioned before, special boundary conditions are required to model open domain characteristics with FEM, because setting the acoustic pressure to zero results in an acoustic soft wall (Dirichlet boundary condition; pressure is zero) and reflections occur. Setting the normal derivative of the pressure to zero, leads to a natural boundary condition and an acoustically hard wall. To model open domain characteristics the following methods can be used (depending on the problem):

- Absorbing boundary conditions (ABC)
- Perfectly matched layer (PML)
- Infinite finite elements.

The infinite finite element method is mentioned here only for completeness; this method will not be discussed or treated within this thesis. More information can be found in [91].

Absorbing Boundary Condition (ABC):

Taking the analytically solution for a one dimensional plane wave the following hypothesis can be done; a wave is propagating in all directions with same speed; Hence, if the wave impinges a wall, it gets totally reflected without loosing any energy. This wall can be defined with a homogenous Dirichlet boundary condition or a Neumann boundary condition. As a result, the wave is propagating in opposite direction and can be separated into a transmitting wave propagating forward and a reflecting wave propagating backward (from source viewpoint).

In Figure 4-6 a propagating wave in positive x-direction (blue wave) is depicted. This wave gets reflected at the hard wall (red wave). Since the reflected wave propagates in inverse direction, but with the same physical nature, the following condition is true by considering (4.10)

$$\frac{\partial p'}{\partial t} = c\frac{\partial p'}{\partial x}. \tag{4.23}$$

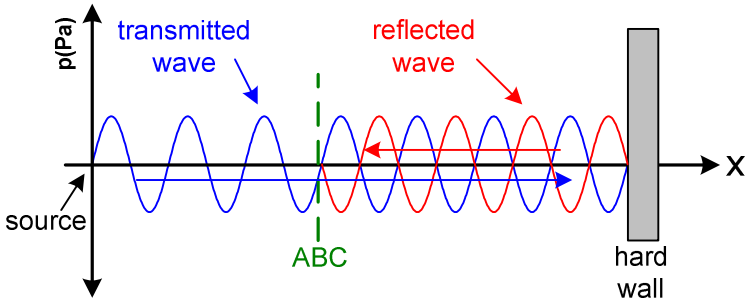

Figure 4-6: Schematic overview of absorbing boundary condition for one dimensional case.

only for the reflected part of the wave (see (4.24)). This means, that the wave propagating in positive x-direction (see (4.25)) is able to pass the ABC, but the reflected wave, which propagates in negative x-direction will not pass the ABC (cancels out). As a result the reflected wave is kept outside the computational domain.

- Wave propagating in positive x-direction (transmitting wave):

$$p(-x,t) = p_0 \cdot e^{j(\omega t - kx)} \tag{4.24}$$

- Wave propagating in negative x-direction (reflected part of wave):

$$p(+x,t) = p_0 \cdot e^{j(\omega t + kx)} \tag{4.25}$$

In one dimensional computation, waves are only able to penetrate ABCs perpendicular (with their normal component) as displayed in Figure 4-6. For higher dimensional problems, this method causes reflections, if the impinging sound wave features tangential parts from the ABC viewpoint. This is exactly the weakness of this method (for first order ABC). The ABC is only able to absorb the normal components of acoustic pressure or potential. Since only perpendicular impinging waves are absorbed, the propagation region is often spherically shaped. The radius or size of the computational domain should be in the range of the far field (wave length dependent parameter).

Figure 4-7 displays three domains with different geometries limiting the computational region. For the first example, a square shaped boundary was used. The problem in this case are the tangential components of the wave field near the edges, as mentioned before. As a result, reflections in corners occur. The second example is an octagonal shaped boundary, where almost no reflections occur, except in the edges, but less than in the square shaped boundary. For the last example, a circular shaped boundary is used. In this example almost no reflections occur, because every wave component is propagating perpendicular towards the boundaries. For this test a single 1000 Hz 1-$\cos^2$ pulse was used located at the origin of the model. For simplifications symmetries were utilized. Therefore, only the right upper corner of the whole model is depicted.

More information about open domain modeling with higher order absorbing boundary conditions can be found in [92], where improvements on other angles of incident are treated. Higher order ABCs will not be treaded in this thesis, but they have to be mentioned for completeness. Investigations on our model have shown, that PML works more stable and accurate for our computational domains. The previous explained mesh adaption technique with Mortar FEM and the enclosing regions provides an easy implementation of an additional layer or shell.

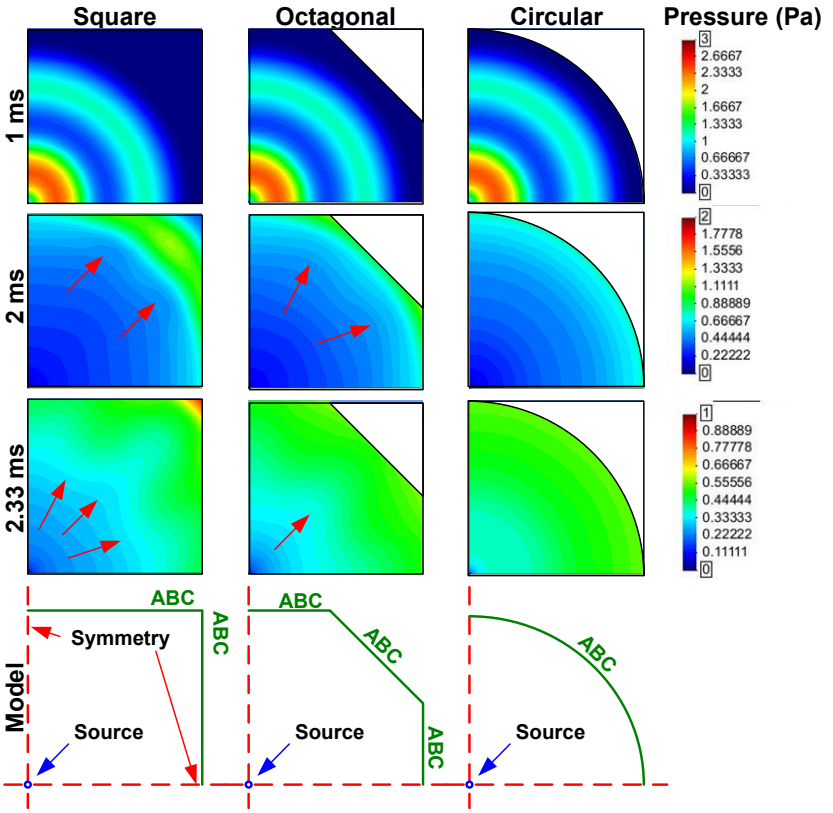

Figure 4-7: Evaluation of absorbing boundary conditions with various open domain shapes.

Perfectly Matched Layer PML:

The basic idea of the perfectly matched layer is to damp the wave within an additional layer surrounding the propagation region and matching the impedances of both layers. Hence the name "*perfectly matched layer*". Figure 4-8 displays the basic setup and working principle. The propagating region (with computational domain Ω_1) is surrounded by the perfectly matched layer region (with computational region Ω_2) to achieve zero reflections at the interface Γ_0.

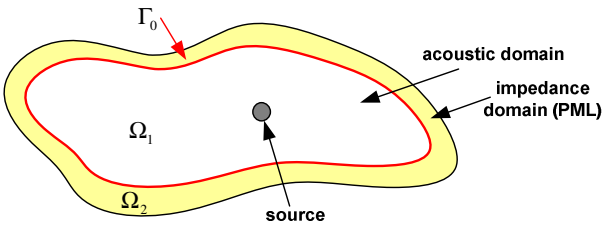

Figure 4-8: Open domain simulation with perfectly matching layer surrounding acoustic computational domain and interface in between both domains.

The complete computational domain increases for this kind of open domain modeling to $\mathbf{\Omega}_1 + \mathbf{\Omega}_2 = \mathbf{\Omega}$. Hence more computational effort is needed to solve PML systems, which is a disadvantage of this system. The procedure can be compared to wave termination in electronics, where impedances get matched, in order to decrease reflections to zero. The reflection coefficient is exactly the same as in electronics, with

$$R = \frac{Z_{\Omega 2} - Z_{\Omega 1}}{Z_{\Omega 2} + Z_{\Omega 1}}. \tag{4.26}$$

For plane waves acoustic impedances can be computed with the product of density and wave propagation speed

$$Z_a = \frac{p'}{\vec{v}' \cdot \vec{n}} \underset{\text{plane wave}}{=} \rho_0 \cdot c\,. \tag{4.27}$$

Figure 4-9 shows two regions with its acoustic properties (density and propagation speed of sound). In the region on the left side an acoustic wave is generated and propagates towards interface direction of the second media on the right side. After passing this interface, the impedance characteristics of the media changes and the wave gets damped.

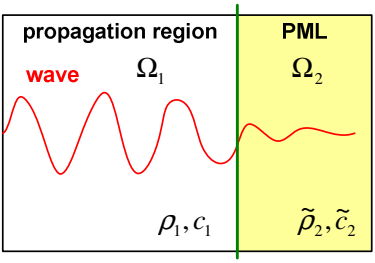

Figure 4-9: Acoustic domain with propagation region and damping region (PML).

The mathematical idea behind this principle is to make the PML density ρ_2 and speed of sound c_2 complex values; as a result the wave number k also turns into a complex value. Therefore, the acoustic pressure for a plane wave is

$$p'(x,t) = \hat{p} \cdot e^{j(\omega t - kc)} . \tag{4.28}$$

Furthermore, (4.28) can be adapted with the complex values used in the perfectly matched layer by

$$\begin{aligned} \tilde{c} &= \frac{c}{1 - j\delta_0} \\ \tilde{\rho} &= \rho_0 (1 - j\delta_0) \\ \tilde{k} &= \frac{\omega}{\tilde{c}} = k(1 - j\delta_0) \end{aligned} \tag{4.29}$$

and results in

$$p'(x,t) = \hat{p} \cdot e^{j(\omega t - kc + jk\delta_0)} = \hat{p} \cdot e^{-k\delta_0} e^{j(\omega t - kx)} . \tag{4.30}$$

This is the analytical solution for the acoustic pressure of a plane wave in the PML region. The first term of (4.30) (red) is for damping the signal, the second one (blue) represents the wave propagation. Now, for higher dimensions the impinging sound wave can be formally split into its components

$$p' \quad \rightarrow \quad p_x', p_y', p_z' . \tag{4.31}$$

Since the plane wave is not impinging the perfectly matched layer perpendicular, the impedance computation must be adapted to

$$Z_i = \frac{\rho_i \cdot c_i}{\cos(\alpha)}. \tag{4.32}$$

as depicted in Figure 4-10.

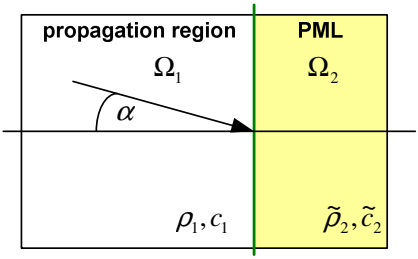

Figure 4-10: Wave hits the interface to PML with angles of incident.

In this way, the damping constants have to be adapted to their components as well

$$\eta_x = 1 - j\frac{\delta_x}{\omega}, \quad \eta_y = 1 - j\frac{\delta_y}{\omega}, \quad \eta_z = 1 - j\frac{\delta_z}{\omega}. \tag{4.33}$$

Hence, the harmonic perfectly matched layer formulation is

$$\eta_y\eta_z \frac{\partial}{\partial x}\left(\frac{1}{\eta_x}\frac{\partial \hat{p}}{\partial x}\right) + \eta_x\eta_z \frac{\partial}{\partial y}\left(\frac{1}{\eta_y}\frac{\partial \hat{p}}{\partial y}\right) + \eta_x\eta_y \frac{\partial}{\partial z}\left(\frac{1}{\eta_z}\frac{\partial \hat{p}}{\partial z}\right) + \eta_x\eta_y\eta_z k^2 \hat{p} = 0. \tag{4.34}$$

Figure 4-11 displays the comparison of both open domain models treated in this thesis, on the left side the absorbing boundary condition of first order and on the right side the perfectly matched layer. It can be seen very well that for the PML an additional layer has to be modeled around the acoustic domain (computational domain is larger). In both models, the source is located at the origin which is at the left bottom corner. As in the previous example (ABC evaluation), the same pulse with 1-cos² is used to generate a propagating wave. The wave hits the open domain region after one millisecond, therefore in the first row

no difference can be seen at all, because no reflections occur. After two milliseconds reflections can be seen very well at the absorbing boundary condition. Even at 2.33 ms no reflection occurs at the perfectly matched layer method, so by investing profitable into computational time (for the additional layer), the quality of the simulation output can be increased significantly. What also can be seen very well is the damping inside the perfectly matched layer, where the sound pressure level decreases to zero close to the surrounding outer-edge. Additional Information about PML can be found in [93-95].

In the MEMS speaker model, the recently developed time depended perfectly matched layer technique is applied. Detailed information can be found in [95].

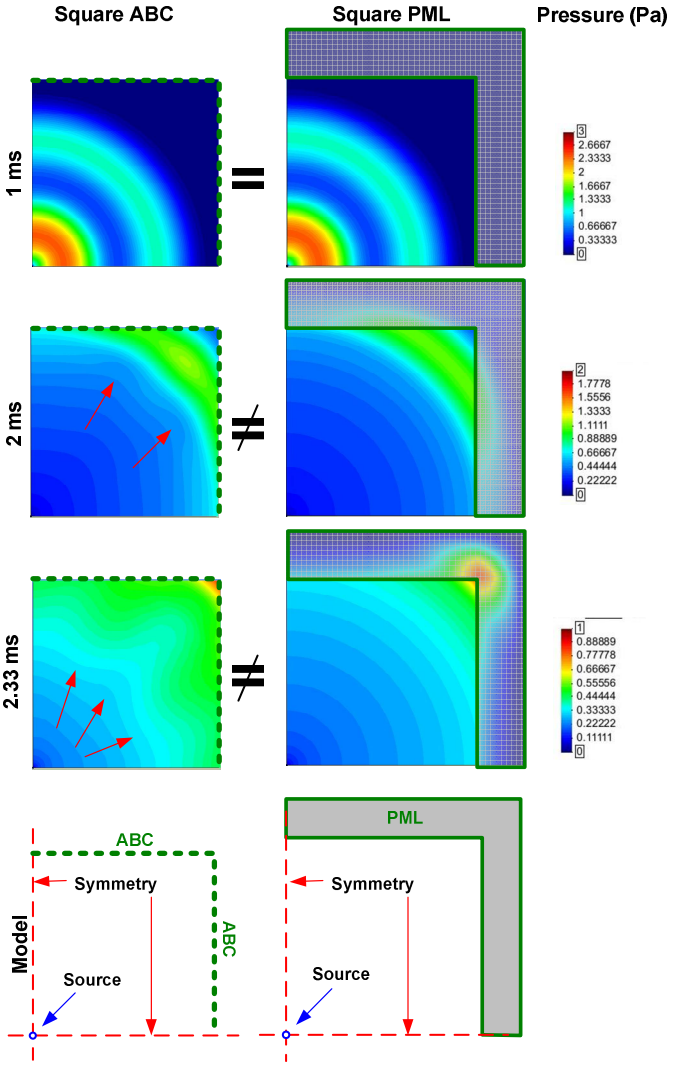

Figure 4-11: Comparison of wave field for open domain computation with perfectly matched layer (PML) at the right side and absorbing boundary condition (ABC) on the left side.

4.4 Speaker Array Modeling with Kirchhoff Helmholtz

The Kirchhoff Helmholtz method is used to compute speaker arrays larger than 16 speakers. Using the classical FE method, leads to a large amount of elements at large speaker arrays. Each speaker cell mesh must be adapted from the mechanical side to the acoustic propagation region as described before. The reason is obvious, the sub micrometer grid at the coupling interface increases the amount of elements extremely – as well as the wrapping Mortar adaption shells. Therefore, the Kirchhoff Helmholtz method is used. Exactly this is the advantage of the method. The disadvantage in our case is, that additional boundary conditions are not implemented, hence the method is only suitable for open domain computations and not applicable for speaker housing computations, where reflections occur.

4.4.1 Huygens Principle of Wave Computation

Huygens concept implies: "*If a spherical wave is emitted from a point source, through a homogeneous and isotropic media, the process of wave propagation can be explained by forces of oscillating particles, which are passing by their movement to their neighbor particles. This is also known as momentum conservation. The process is symmetric in all directions under the condition that the media is homogeneous and isotropic. This particle characteristic gives us the reason for producing spherical waves.* [96]"

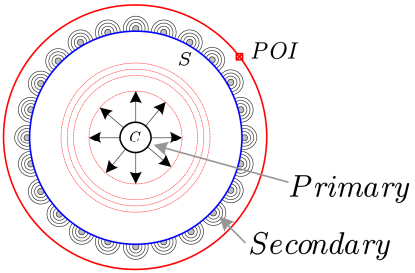

Figure 4-12: Huygen's concept of wave propagation.

Figure 4-12 describes Huygens concept of wave propagation. In point *C* a sound source, generating spherical waves is located. This point is called *primary sound source*. The wave front of this primary sound source is spread out homogeneous (without obstacles). This primary

sound source can be replaced by distributed equivalent sound sources located on the spherical surface. These sources are called *secondary sound sources*. By monitoring the waves inside the sphere no difference can be measured. It is exactly the same characteristic if the sound is created from the primary or secondary sources. Thereby, the basis of mathematics for wave field synthesis was found [97]. Later these mathematical basics were summarized in Kirchhoff Helmholtz integrals of acoustics. Two Rayleigh integrals can be derived, where the first introduces the pressure and the second the particle velocity based propagation. If the wave equation is considered at a single frequency, the harmonic ansatz combined with the wave equation (4.8), results in Kirchhoff Helmholtz's equation

$$\Delta\varphi + k^2\varphi = 0\,. \tag{4.35}$$

4.4.2 Harmonic Computation with Rayleigh Integrals

The two Rayleigh integrals are specializations of the Kirchhoff Helmholtz integral. A volume Ω is introduced to get from the homogeneous wave equation (4.35) to the integral form of Kirchhoff Helmholtz. This volume is surrounded by a surface Γ. On the surface a normal vector $\vec{n}$, is defined. The volume is depicted in Figure 4-13. In this volume there are two fields, φ_1 and φ_2 [87].

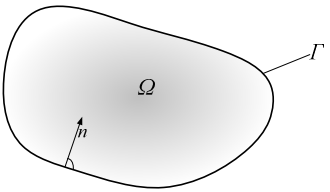

Figure 4-13: Volume Ω with surrounding surface Γ and the normal vector n.

By using Greens integral theorem, the relation between the surface Γ and volume Ω can be described

$$\int_{\Gamma}\left(\varphi_1\frac{\partial\varphi_2}{\partial\vec{n}} - \varphi_2\frac{\partial\varphi_1}{\partial\vec{n}}\right)d\Gamma = \int_{\Omega}\left(\varphi_2\Delta\varphi_1 - \varphi_1\Delta\varphi_2\right)d\Omega\,. \tag{4.36}$$

If the homogeneous equation (4.35) is solved for φ, the result is known as the Kirchhoff Helmholtz integral in frequency domain

$$\varphi_{(POI)} = -\frac{1}{4\pi}\int_{\Gamma}\frac{e^{-ikr}}{r}\frac{\partial\varphi}{\partial\vec{n}}d\Gamma + \int_{\Gamma}\varphi\frac{\partial}{\partial\vec{n}}\left(\frac{e^{-ikr}}{r}\right)d\Gamma\,. \tag{4.37}$$

By the help of this equation, each point inside the volume Ω surrounded by the surface Γ can be calculated. The first term in (4.37) represents the distribution of monopole sources specified by sound particle velocity. The second term represents the distribution of dipole sources specified by sound pressure. This implies, that the normal derivative of φ has to be known on the surface Γ, to be able to calculate the field φ. As a first approach, the loudspeaker membranes can be seen as piston moving solids (without membrane bending effects). This simplification has to be defined, in order to simplify the calculation process and is valid in our case, because of the large diameter to stroke level ratio. The membrane movement results in a normal velocity component v_n of the membrane and therewith due to the continuity of the velocity to the normal component v_n' of the particle velocity

$$-\frac{\partial\varphi}{\partial n} = -\left(\frac{\partial\varphi}{\partial x}\vec{e}_x + \frac{\partial\varphi}{\partial y}\vec{e}_y + \frac{\partial\varphi}{\partial z}\vec{e}_z\right)\cdot\vec{n} = -\vec{n}\cdot\nabla(\varphi) = v_n'\,. \tag{4.38}$$

Consequently, the Kirchhoff Helmholtz integral can be split up into two separate integrals, also known as Rayleigh integrals [97], as mentioned before. The first Rayleigh integral is used in our approach, which is about monopole sources described by acoustic particle velocity

$$\varphi_{(POI)} = -\frac{1}{4\pi}\int_{\Gamma}\frac{e^{-ikr}}{r}\frac{\partial\varphi}{\partial\vec{n}}d\Gamma\,. \tag{4.39}$$

The reason is obvious, because velocity is the derivation of the membrane movement and therefore our mechanical acoustical coupling condition. Hence, the normal derivative of φ becomes very important, because this value corresponds to the membrane movement. As a result, the sound field at any point of interest can be calculated by knowing the normal component of the membrane deflection; assuming a constant piston moving membrane, no reflections, a homogeneous medium and a surface Γ which is infinite far located, the elementary solution displayed in (4.10) is fulfilled.

For our model, (4.39) has to be adapted to the digital speaker array pattern (see section 6.1.1). At this point it is very important to mention, that each speaker cell must be fabricated identically and driven with the same frequency and stroke level, since the computations are based on harmonic computations. Equation (4.40) depicts the implemented formula for the wave field calculation tool, whereby $\partial\varphi_i/\partial\vec{n}$ denotes the normal derivative of φ_i for the i-th membrane of the speaker array. If this value is set to zero, the speaker cell is inactive (important for DSR)

$$\varphi_{(POI)} = -2\left[\frac{1}{4\pi}\int_{\Gamma}\frac{e^{-ikr}}{r}\sum_{i=1}^{N}\frac{\partial\varphi_i}{\partial\vec{n}}\,d\Gamma\right]. \tag{4.40}$$

Figure 4-14 displays the difference between the full sphere wave propagation and the sphere limited by the infinite surface located at the speaker array position. In our case the speaker array is soldered on a printed circuit board (hard wall). This fact is considered by a factor of two in (4.40).

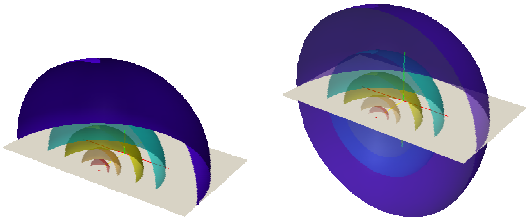

Figure 4-14: Computational domain with (right) and without (left) surface at speaker array position for reflecting sound waves.

The complex notation for harmonic ansatz therefore results in

$$p' = \rho_0\; j\omega\varphi\, e^{j\omega t}\,. \tag{4.41}$$

NOTE: Harmonic computations require harmonic membrane movements. As explained before, the system is highly nonlinear due to geometric nonlinearities and the nonlinear electrostatic force!

4.4.3 Transient Computations with Rayleigh Integral

To be able to investigate time dependent wave propagation the transient solution for Kirchhoff Helmholtz integral can be used as described in [87]. With the Fourier ansatz the sound pressure level is computed at any point of interest for any time. The Fourier transformation of the time signal can be written as (this formulation depends on frequency ω).

$$p_{(\omega)} = \frac{1}{2\pi} \int_{-\infty}^{\infty} p(\tau)\, e^{-j\omega\tau} d\tau \,. \tag{4.42}$$

Hence, the time signal can be represented as

$$p_{(t)} = \frac{1}{2\pi} \int_{-\infty}^{\infty} e^{+j\omega t} \left[\int_{-\infty}^{\infty} p(\tau) e^{-j\omega\tau} \right] d\omega \,. \tag{4.43}$$

As already discussed, in the harmonic case the exponential ansatz (4.10) represents only a single frequency. For the complete frequency spectrum a summation over all frequencies has to be utilized

$$\varphi(\vec{x},t) = \int_{-\infty}^{\infty} \varphi_{\mathbf{x}} e^{i(\omega t)} d\omega \,. \tag{4.44}$$

Furthermore, Ehrenfried [87] describes the normal derivative with respect to space is

$$\frac{d\varphi}{d\vec{n}}(\vec{x},t) = \int_{-\infty}^{\infty} \frac{d\varphi}{d\vec{n}}(\vec{x}) e^{i(\omega t)} d\omega \,, \tag{4.45}$$

and with respect to time (by replacing t with $t+\Delta t$) is

$$\frac{d\varphi}{dt}(\vec{x},t) = \int_{-\infty}^{\infty} i\omega\, \varphi_{\omega}(\vec{x}) e^{i(\omega t)} d\omega \,. \tag{4.46}$$

The retransformation at place x_0 results in a summation of monopole and dipole sources which is also known as the Rayleigh integrals

$$\varphi(x_0,t) = -\frac{1}{4\pi} \int_{\Gamma} \int_{-\infty}^{\infty} \frac{e^{-ikr}}{r} \frac{\partial \varphi_{\omega}}{\partial \vec{n}} e^{i\omega t} d\omega\, d\Gamma + \frac{1}{4\pi} \int_{\Gamma} \int_{-\infty}^{\infty} \varphi_{\omega} \frac{\partial}{\partial \vec{n}} \left(\frac{e^{-ikr}}{r} \right) e^{i\omega t} d\omega\, d\Gamma \,. \tag{4.47}$$

Due to the same reason as in harmonic case (simplification), we only consider the monopole part and neglect the dipole part. Therefore, the inverse transformation of the monopole part using (4.45) and (4.46) results in

$$\int_{-\infty}^{\infty} \frac{e^{-ikr}}{r} \frac{\partial \varphi_\omega}{\partial \vec{n}} e^{i\omega t} d\omega = \frac{1}{r} \int_{-\infty}^{\infty} \frac{\partial \varphi_\omega}{\partial \vec{n}} e^{i\omega\left(t-\frac{r}{c}\right)} d\omega = \frac{1}{r} \frac{\partial \varphi}{\partial \vec{n}}\left(\vec{x}, t-\frac{r}{c}\right). \tag{4.48}$$

The result shows the time dependent normal component of the particle velocity, decreasing with the reciprocal of the distance r, where t is the actual time, r the distance from the source to the point of interest and c the speed of sound in the media.

For calculating the pressure at the point of interest at any time, the density has to be multiplied with the time derivative of the normal component of the particle velocity, or of the normal component of the membrane acceleration

$$p' = \rho_0 \frac{\partial}{\partial t}\left(\frac{\partial \varphi}{\partial \vec{n}}\right) = \rho_0 \frac{\partial^2 u_n}{\partial t^2}. \tag{4.49}$$

Equation (4.47) has to be adapted with (4.48) and (4.49) to get the pressure formulation, which has been implemented

$$p'(\vec{x}_0, t) = \frac{1}{4\pi} \int_\Gamma \frac{\rho_0}{r} \frac{\partial^2 u_n}{\partial t^2}\left(\vec{x}, t-\frac{r}{c}\right) d\Gamma. \tag{4.50}$$

4.5 Wave Field Calculation Tool

In the following the wave field calculation tool, implemented in Matlab, is explained. First a brief overview of the tool is given, followed by a description of each module on more detail. The focus of this chapter will be the implementation of the Kirchhoff-Helmholtz integral and also the Gauss Legendre integration using a point of interest map. Finally there will be a comparison between the computed sound pressure level of the wave field calculation software (WFCS) and the FE result. In Figure 4-15 the three main modules of the WFCS can be seen. Starting at the input module, the user can set the points of interest, the characteristics of the propagation area and the array properties. In addition to this the membrane movements are set and

linked with the corresponding membranes (special for digital sound reconstruction). In the second main part, all defined inputs are used to generate the point of interest map as well as the MEMS speaker membrane activeness levels. In this step the solution of the sound pressure level according to harmonic or transient case is done. The third and last part handles the post processing, where all results are saved and visualized to the user.

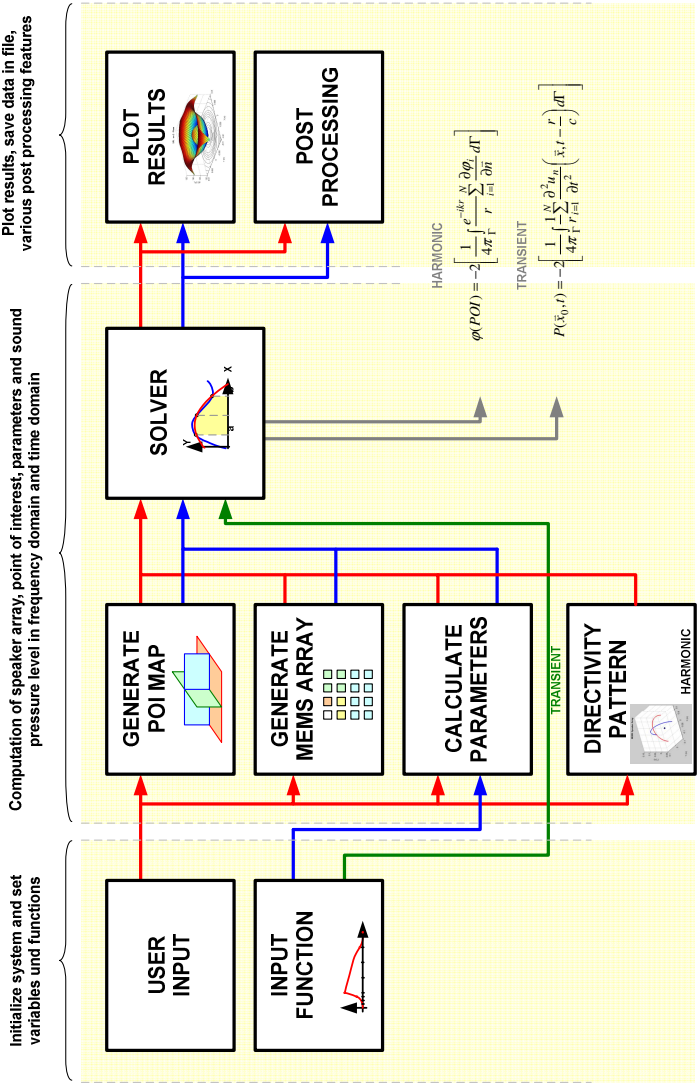

Figure 4-15: Block diagram and abstracted overview of wave field calculation software.

4.5.1 Input Module

The input module consists of two states, first the initialization and second the user input state. At the initialization state, free memory is allocated for the computational tool and all variables are set with their default values. The user input state overwrites the default values with user data and generates the MEMS speaker array. Quadrilateral membranes were used, because of Gauss Legendre integration, where the surface area must be equal to the representing circular shaped membranes to correctly compute the SPL at the POI.

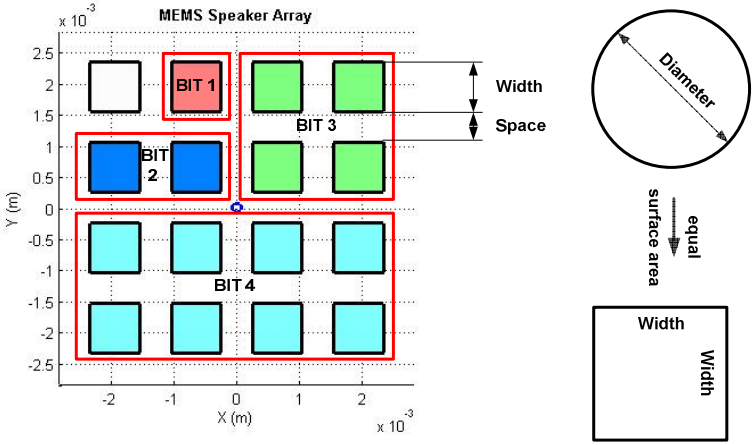

Figure 4-16: Four bit speaker cell array with default dimensions and spacings.

The tool can also be used to compute the sound pressure level of a single speaker cell including the proper membrane movement with bending features. Therefore the N by M sized array disables all electrodes on the outer region – outside the corresponding square shaped membrane as displayed in Figure 4-17. For this example a 10 by 10 array was used, where the approximated circular speaker membrane can be seen. For this example the size of the single speaker cells and the spacer in between correlates directly to the error.
For modeling the physical bending of the speaker cell, each piston is represented by its own movement characteristic including its own stroke level, but then the advantage of fast SPL computations is gone, because this would substitute the FE model discretization.

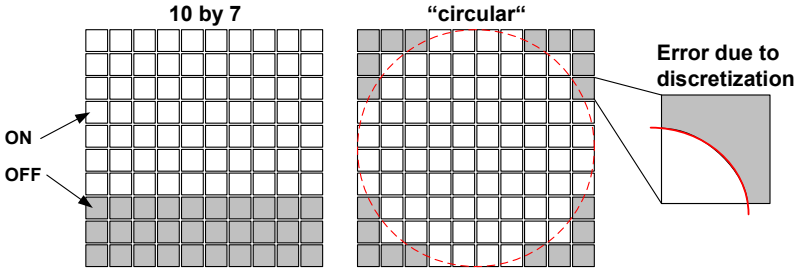

Figure 4-17: Array with 100 speaker elements, NxN to NxM and squared to circular pattern.

The second important input argument is the point of interest (POI) list or map. At the POI the SPL result is calculated. There are three basic properties for generating a point of interest map in Cartesian coordinate system in the computational tool. The start, the stop and the discretization size in x and y direction (see Figure 4-19). The discretization value can be compared to the mesh size in FE simulations. For distance variation between the POI and the speaker array (z-direction) a function depending on x and y can be applied. An example for a generated POI map with the x and y dimensions *-1 cm* to *+1 cm* and a height of *1 cm* with a total distance of *2 cm* center aligned over the speaker array is given in Figure 4-18. For this example a two by two array was used.

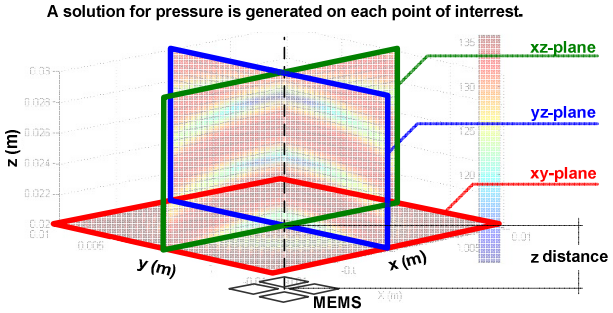

Figure 4-18: Point of interest map with dimensions *-1 cm* to *1 cm* with a height of *1 cm* and an distance of *2 cm* center aligned over the MEMS array.

The height of the xz-plane and yz-plane is taken from the positive x- and y-dimension. The step size is also taken from these two planes. with this POI map a wave propagation can be computed easily and displayed as slice view in 3D. The sound pressure level is indicated by a color map in this visualization.

4.5.2 Computational Module

First a grid in x and y dimension is generated, as explained before. An example for a one dimensional case is depicted in Figure 4-19.

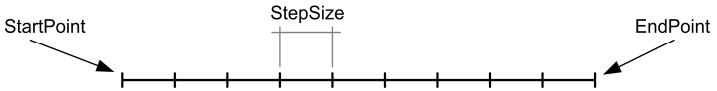

Figure 4-19: Linear discretization example for one dimensional case.

This is an example for equidistant discretization, but there is also the possibility to set the points arrangement in non-equidistant case. The third dimension (z) is applied by an user equation with respect to x and y. Figure 4-20 displays three cases of a point of interest map, where (a) represents a flat surface, often used for investigating maximum SPL, (b) a curved (quadratic) POI map and (c) a spherical surface, which is often used for directivity pattern computations.

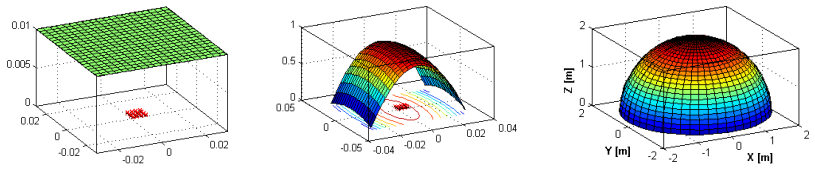

(a) (b) (c)

Figure 4-20: Point of interest map for three cases: (a) constant z-function, (b) quadratic function, (c) spherical surface.

Numerical integration is applied in many computing applications dealing with integrals. The Kirchhoff Helmholtz integral (harmonic (4.40), or transient (4.50)) features for most cases no analytical solution. As a result, a numerical solving process has to be used to get an accurate solution. A brief overview about trapezoidal and Simpson rule is given in Appendix D.

4.5.3 Output Module

The output module is the last module in the computational chain of the wave field calculation tool. In this module the calculated results are visualized to the user.

4.5.4 WFCT Verification

To verify the WFCT a FE computation is used. For this test a membrane array with a size of four by four (16 speaker cells) and a single speaker were compared. Since the membranes in FEM are circular shaped, the side length of Kirchhoff Helmholtz tool is assumed with 797.6 µm to reach the same surface area as the circular shaped membranes with a diameter of 900 µm. The electrostatic mechanical simulation results of 1 µm and 530 nm were verified with optical laser vibrometer measurements and used as input parameters in this simulation. Figure 4-21 a.) shows the results for a single speaker element between 1 kHz and 20 kHz at a distance of 1 cm. Figure 4-21 b.) shows the difference between the FE result and the Kirchhoff Helmholtz result.

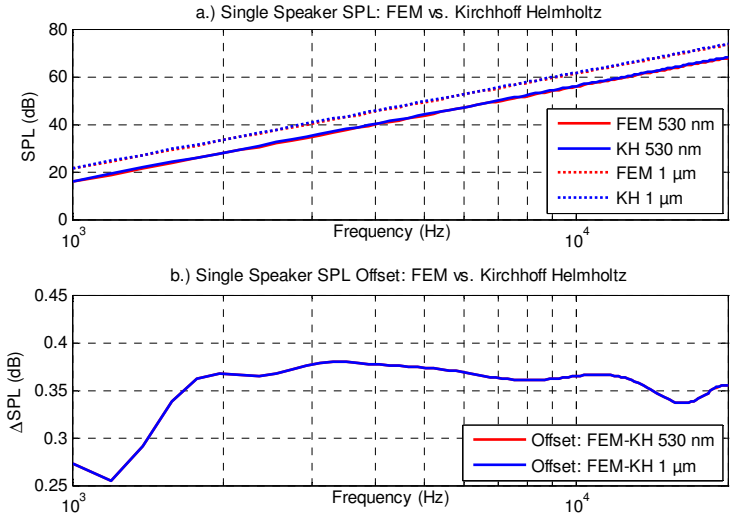

Figure 4-21: Verification of SPL between Kirchhoff-Helmholtz and FE simulation result – single speaker.

By using 16 speaker cells the sound pressure level increases with an theoretical value of +24dB, compared to the single speaker cell results. Figure 4-22 a.) shows the sound pressure level results of 16 speaker cells. It can be seen that the SPL increases by +24dB for this setup. This is a result of the larger surface (gain of +6dB for doubling the surface). In Figure 4-22 b.), the difference between the FEM result and the Kirchhoff Helmholtz result is depicted.

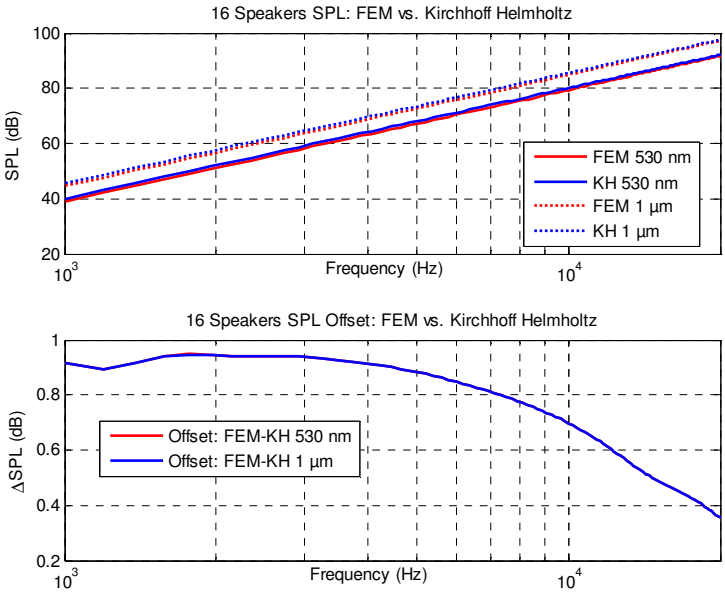

Figure 4-22: Verification of SPL between Kirchhoff-Helmholtz and FE simulation result – 16 speaker cells.

To verify both acoustic models with the fabricated speaker system, the small four by four array was driven at simultaneously sinusoidal stimulus. For this test, the initial system with the flat back plate without any optimization steps was used and loaded with a bias voltage of 10 V and an audio signal level of 1 V to 4 V. No pre-distortion of the nonlinear electrostatic mechanical coupling was implemented, hence the results in frequency domain do not show sinusoidal membrane movement. In Figure 4-23 the measured sound pressure levels are compared to the simulation results. Because of small array dimensions

and the relatively low stroke level (below snap-in), the resulting audible SPL starts at 1 kHz. In addition to this, the measurements were taken in standard laboratory setup without an acoustic box, hence the ambient noise is about 50 dB.

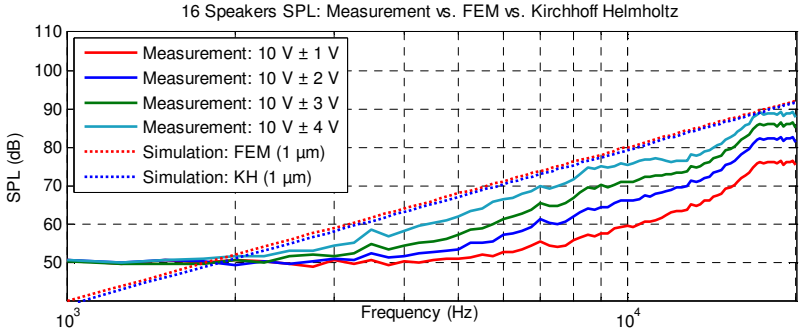

Figure 4-23: SPL measurements for non snap-in mode with sinusoidal characteristics, loaded with bias voltage and superimposed with acoustic audio signal compared to FEM and Kirchhoff Helmholtz computational results.

Transient simulation data was verified with the harmonic data of the Matlab tool. For this scenario a single speaker cell was stimulated with a 10 kHz sinusoidal motion, with an amplitude of 2 µm at a distance of 20 mm. The harmonic results show 67.5753 dB_{SPL} and the transient simulation results 67.5770 dB_{SPL}. It can be seen, that the Kirchhoff Helmholtz tool alternatively is a powerful method for SPL computations.

4.5.5 Snap-In and Audio Quality

As already introduced in section 2.3, there are two movement characteristics available for our MEMS speaker system. First, driving with voltage levels below the snap-in point, where approximately a third of the available stroke level is used and second, driving the speaker at full stroke level with a voltage higher than the snap-in point. As a result, there is a tradeoff between sound level pressure (with respect to stroke level) and total harmonic distortion. Figure 4-24 displays a non-snap in driven audio cell with the applied voltage in the first row, the second row shows the resulting membrane movement, the

third row the acoustic signal and the fourth row outlines the FFT frequency spectrum for signal quality analysis.

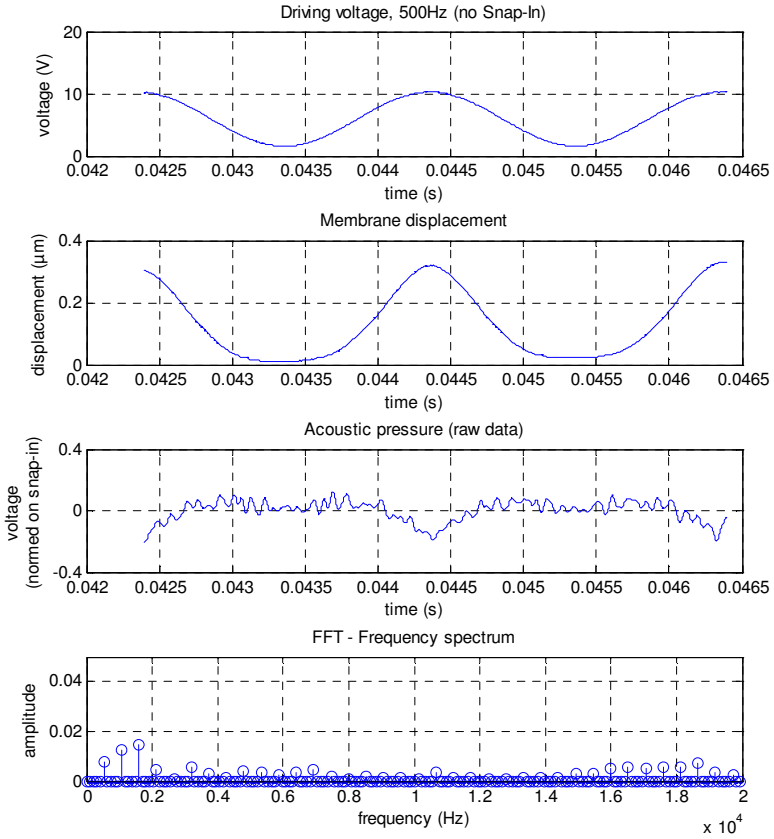

Figure 4-24: Membrane loaded below snap-in point with applied voltage a), center point of membrane stroke level b), acoustic signal c.) and FFT frequency spectrum d).

By increasing the voltage level over the snap-in point, the membrane is rapidly forced towards the stator at snap-in and released due to its mechanical spring characteristics at release state. This results in a higher harmonic distortion but larger amplitude. The measurement data are depicted in Figure 4-25, where the first row shows the applied voltage, second row the center point membrane displacement, third row

the acoustical response and fourth row outlines the signal quality as FFT frequency spectrum. Comparing results of Figure 4-24 and Figure 4-25, validates the higher sound pressure level for the snap-in case, but we have to pay the price of higher total harmonic distortion. In both investigations 500 Hz audio signal were used. The acoustic pressure was recorded at a distance of 100 mm and normed on the snap-in case.

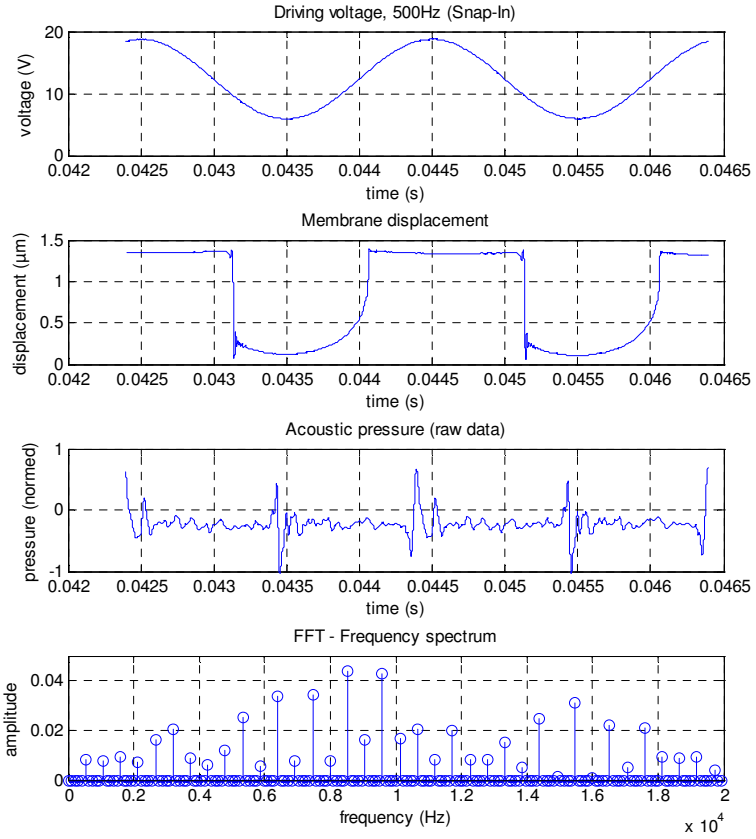

Figure 4-25: Membrane loaded over snap-in point with applied voltage a), center point of membrane stroke level b), acoustic signal c.) and FFT frequency spectrum d).

CHAPTER 5

5 Optimization I: Buckling Back Plate

There are three major parameters to increase the sound pressure level (SPL) for our MEMS speaker. First parameter is the frequency, where the limitation is given by human auditory, between 20 Hz and 20 KHz [98]. Second parameter is the surface area, where the limitation is given by dimensions and size as well as cost economical effects from the manufacturer side. Third parameter is the stroke level of the membrane, where the limitation is also given by manufacturer side due to technology restrictions. The challenge is to increase the gap size or stroke level with the same production steps to keep the device cheap from manufacturer side. This optimization is called buckling back plate (BBP), where previously explained stress stiffening effects lead to self raising structures. Since the resulting SPL is a result of volume flow, where the volume is defined by surface times stroke level, the increase in stroke level can be used to increase the SPL [15].

5.1 Buckling Back Plate Functional Principle

In a typical manufacturing process, various layers are spattered and etched in miscellaneous process steps. Spattering and etching takes on the one hand time and on the other hand multiple layers result in multiple stencils, which can be expensive and is not attractive for manufacturers. From this point of view, the spattering process is limited in thickness, which results in a maximum of stroke level for our membranes. Due to this costly and time consuming process steps a flat

and fast fabrication method is desirable. The aim is to combine layers with various intrinsic pre-stress, so that the resulting MEMS speaker can be fabricated as cost economically flat design with stress induced back plate raising – hence the name buckling back plate. The first layer used, is poly silicon with a tensile pre-stress of about 100 MPa, an elasticity module of approximately 162 GPa and a Poisson ratio of 0.26. This layer is used as electrode for the back plate as well as the membrane. The second layer used is silicon nitride (SiN4) with a tensile pre-stress of about 1 GPa, an elasticity module of approximately 300 GPa and a Poisson ratio of 0.24. These parameters were determined in a previous work on the silicon microphone by Füldner [47] and fitted with simulations on the MEMS speaker system [48]. The second layer used is an insulation layer, which is applied between the membrane and the back plate to avoid short circuits in mechanical contact case.

The basic idea behind the buckling back plate structure (BBP) is based on an increased volume flow and on a flat and cheap fabrication technology. By covering the mechanically softer poly silicon layer with the mechanically hard SiN4 layer, mechanical forces acting as levers occur, and as a result, the structure starts to bend the soft material towards the hard coating. An analogue effect can be found in bi-metal structures with various temperature expansion coefficients - one material contracts heavily, the second material less, which results in a mechanical bending motion. This effect is displayed schematically in Figure 5-1.

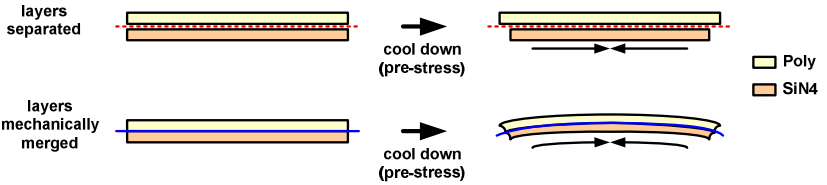

Figure 5-1: Functional principle of bi-metal or various intrinsic pre-stress layers combined.

As can be seen in the first row of Figure 5-1, the layers are mechanically separated. During the thermo cool down process, the insulation layer contracts more compared to the poly silicon layer. By mechanically merging these layers, the different tensions of both layers results in mechanical deformations. The nitride layer contracts stronger

than the poly silicon layer, which results in a bending of the structure towards the nitride layer. The flat design process of the buckling back plate system is depicted in Figure 5-2. In the first draft (a) the silicon structure (the initial microphone structure) is displayed, where the poly layer is fully covered with the nitride layer. This results in a flat structure with minimum stroke level. The second design state (b) shows incipient stages of corrugation rings. While in this case the resulting forces are too weak to bend the poly silicon layer. The third design state (c) displays an optimized structure with deep corrugation rings for softening the poly silicon layer on the one hand and increasing the lever forces on the other hand. A design process overview is given in [99].

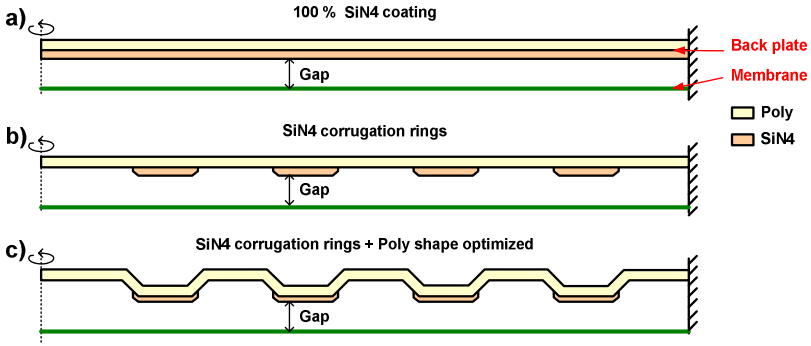

Figure 5-2: Buckling back plate design with full SiN4 coating (a), with corrugation rings (b) and optimized corrugation ring shape (c).

5.1.1 Reduced Stiffness

Advantage of the buckling back plate design, as depicted in Figure 5-2, is the increased volume compared to a flat structure. Disadvantage is the reduction of the back plate's stiffness. Because of the missing silicon nitride areas, inside the corrugation rings, the local stiffness alternates between stiff and soft. Soft properties are at the poly silicon layers and stiff properties are at the poly and nitride silicon layers. As a result, the global stiffness is reduced, compared to the MEMS microphone structure with 100% silicon nitride coating. Since the electrostatic attracting force acts on both electrodes, the back plate must be stiff compared to the membrane, to increase the stroke level of

the membrane. To outline the problem of the stiffness reduction an example is given. If both structures show same flexibility and a force is applied on them, the back plate starts to move down and the membrane up, hence they get into contact exactly at half stroke level (geometrically nonlinearities neglected). In this case the membrane loses its half stroke level. As a result, the flexibility of the back plate reduces the effective SPL, because of stroke level loss of the membrane. The back plate is perforated and acoustically transparent, which results in a silent movement without SPL generation. The question is, how can the flexibility of the buckling back plate be determined easily and accurate prior fabrication. To solve this problem, two approaches have been developed.

First approach: A modal analysis can be used to determine the stiffness of an arbitrary structure. If system one shows the lowest resonance frequency at x Hz and system two shows its lowest resonance frequency below x Hz, than system two is softer compared to system one. This model assumes a linear mass spring system with the following restrictions:

- The mass and materials of both systems must be the same (in our case they are not due to variations of thickness, lever geometries, ...)
- The system is geometrically linear (for example, large deformation is neglected)
- The stiffness is derived via a single mass spring model (this does not take various layers with various tensile pre-stresses and multidimensional effects for lever arms into account)

Second approach: A purely simulation based three stage measurement setup is used to determine the stiffness including all nonlinear effects of the buckling back plate, as can be seen in Figure 5-3. In this virtual setup, the buckling back plate is loaded with an increasing external pressure and the flexibility is computed. In the first stage, the structure is designed flat, associated with material properties and the resulting buckling back plate structure is computed statically. This stage simulates the fabrication cool down process and characterizes the buckling back plate shape. A detailed description of this process is given in chapter 5.2. In the second stage, the buckling back plate is loaded with a constant external pressure. The maximum pressure level

is derived from a previous simulation and represents the electrostatic attracting force for the flat MEMS design. The external pressure pushes the back plate towards the membrane. In the third stage, the different nodal displacements of the buckling shape (result of stage one) and the loaded buckling shape (result of stage two) result in a local flexibility information. Advantage of this method is, that all geometrical and even physical nonlinearities can fully be taken into account. Disadvantage is the multi stage model setup with complex nonlinear computations - many parameters affect the result, hence each result must be checked carefully for numerical and physical interpretations. The idea of this simulation setup is not a novel topic, since it is often used for stiffness analysis and mechanical characterization of MEMS structures. A detailed description of this idea can be found in [100]. The advantage of the FEM model used is the possibility to parameterize thickness of layers, as well as corrugation dimensions up to mechanical properties as pre-stress or Young's modulus without expensive silicon fabrication technology.

Figure 5-3 displays the three modeling stages for stiffness determination.

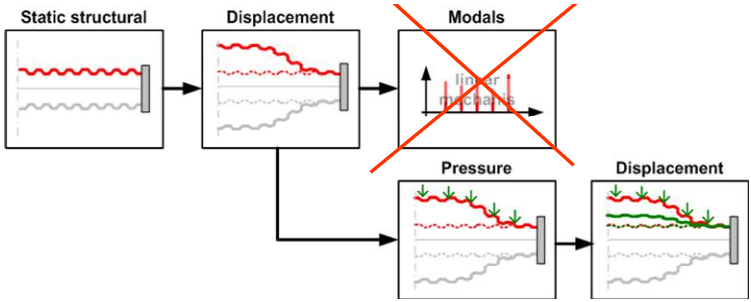

Figure 5-3: Modeling blocks for stiffness investigation.

If zero nodal displacements occur under pressure load, the structure is infinite stiff. Therefore, the relation between compliance δ and displacement difference can be written as

$$\delta = \sim \Delta u \,. \tag{5.1}$$

This parameter can be used as local information for each node or cumulatively weighted with the surface as global parameter for the total structure.

5.2 The Reference System

Because of technology limitations in fabrication processes, parameters like thickness, length, pre-stress or etching angles, can not be defined arbitrary. The first prototype or functional sample was designed with already known fabrication steps from the CMOS compatible technology processes. This functional sample is used as initial system in the following investigations and not optimized in any way. Based on this initial system, the buckling back plate is optimized referring to volume and stiffness in the bounds of feasible technology parameters.
As already mentioned, the initial system is the functional sample or first prototype of the buckling back plate. Aim of the modeling process is the accurate simulation of the mechanical behavior, starting at the flat design, including all necessary nonlinearities, up to the buckling back plate (BBP) shape. The basic functional principle was depicted in Figure 5-2. The fully implemented MEMS speaker model can be seen in Figure 5-4.

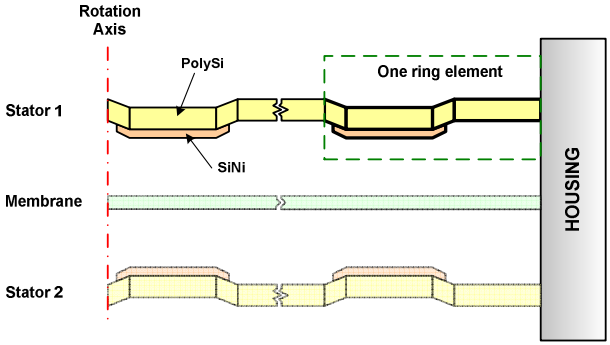

Figure 5-4: Axis rotational mechanical model of buckling back plate with top and bottom stator, membrane and housing.

The membrane and second stator are excluded from the model, because they are not influencing the static buckling back plate results. The back plates housing is simply modeled with a clamping area, where fixed support is defined. Utilizing symmetrical attributes and material parameters from previous simulations [48], an axis symmetric model was used. Very important are mechanical properties, like elasticity module, Poisson ratio, intrinsic pre-stress, as well as geometrical parameters like thickness, length and corrugation radii. By neglecting

corrugation radii from etching and spattering processes, a numerical problem in the form of singularities can occur, hence this is one of the most important parameters for local stress investigations. By the help of APDL, a script was developed, where all important design parameters can be taken into consideration and easily changed on runtime. Possible parameter changes and a schematically overview of a single corrugation ring is depicted in Figure 5-5.

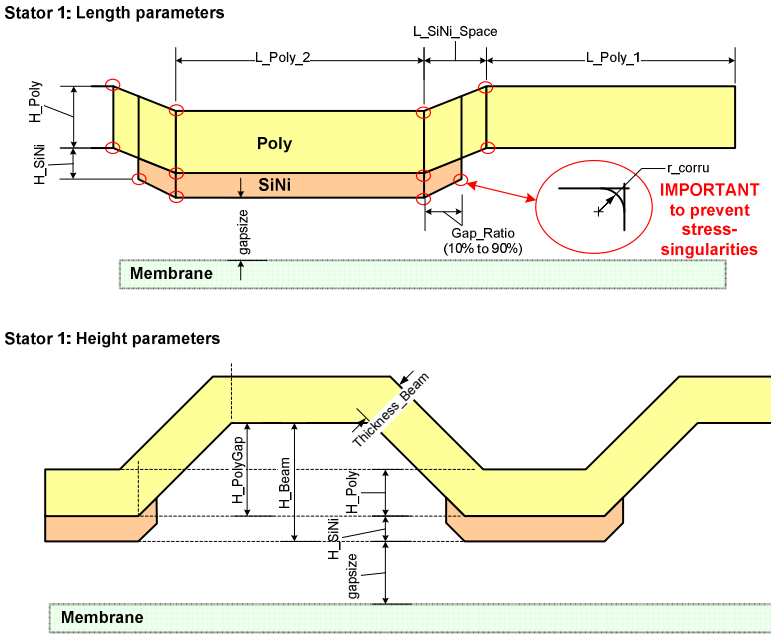

Figure 5-5: Parameter of one corrugation ring for length (top) and height (bottom).

The reference system or initial system uses data from Table 5-1. Unquoted data are not required for structural mechanical investigations. To give an example; Parameter "gapsize" of Figure 5-5, does not affect the buckling shape, but is important for electrostatic mechanical coupling.

Table 5-1: Reference parameter set of buckling back plate corrugation rings for initial or reference system.

Parameter	Dimension	Description
H_SiNi	280 nm	Silicon Nitride thickness
H_Poly	330 nm	Polysilicon thickness
H_Beam	600 nm	Beam height
H_PolyGap	H_Beam-H_SiNi	Polysilicon gap (manufacturer limitation)
Thicknes_Beam	H_Poly	Beam thickness (manufacturer limitation)
L_Poly	10 µm	Corrugation length (L_Poly1 and L_Poly2 with ratio 1:1)
Diameter	1050 µm	Buckling back plate diameter
N_corru	23	Number of corrugation rings
corru	100 nm	Corrugation radius (manufacturer process)

5.2.1 Verification

The reference system or initial buckling back plate system was characterized by measurements at CTR GmbH. A white light interferometer measurement setup was used, to determine the three dimensional shape of the buckling back plate. A x-z plane was extracted from measurement data to verify the simulated axis rotational results. Figure 5-6 displays the first buckling back plate prototype, representing the reference system and the x-z plane to verify the axis symmetric model.

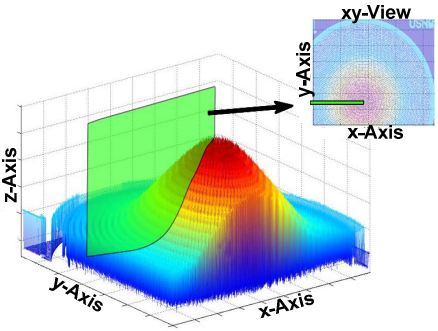

Figure 5-6: White light interferometer measurement of buckling back plate structure with x-z plane for FEM verification.

The measurements show that the basic idea of various tensile pre-stress layers is working for MEMS speakers with buckling back plate systems. Due to tolerances in fabrication processes, in-plane imperfections can occur. These imperfections lead to inhomogeneous buckling shapes. Since the FE model used, is an axis rotational model, in-plane imperfections are not taken into account. As a result, to evaluate the accuracy between the reference back plate system and the FE result, a homogenous buckling device needs to be chosen to extract the x-z plane. In Figure 5-7 the displacements of the axis rotational FE model and the measured reference device are depicted.

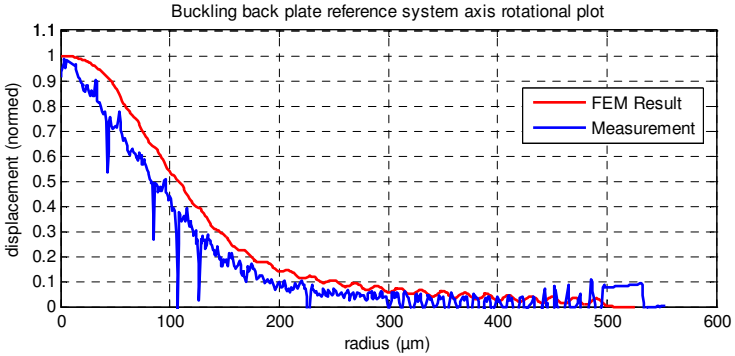

Figure 5-7: FE model result versus measurement of buckling back plate static deformation.

The displacement of Figure 5-7 is normed on the FE result, since this result is used as reference data for parameter variations.
As mentioned before, the back plate is designed acoustically transparent, hence the surface is perforated with holes (see [48]). The white light interferometer beam penetrates the perforation holes directly and diffraction occurs at the hole edges. This results in sporadically disappearing measurement signals with high signal to noise ratio. Since the gap size between membrane and the flat back plate structure is -2.2 µm, the measurement data is cut off below 0 µm level per definition. A zoomed result for x-z plane and y-z plane investigation is displayed in Figure 5-8, where the spider suspension fixing the corrugation rings and the perforation holes can be seen in detail.

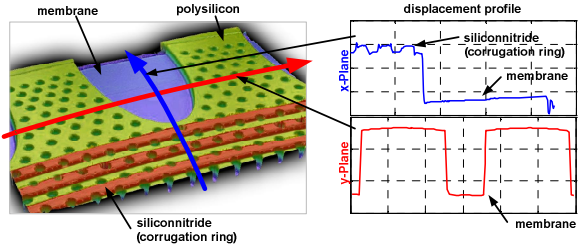

Figure 5-8: Zoomed edge area of white light interferometer measurements on X and Y plane.

5.3 Parameter Variations and Optimization

The FE model includes all important parameters for optimizing the buckling back plate structure, towards volume increase and stiffness. In the first parameter investigation, one by one parameter was changed between +50% and -50%, of its initial value. With this simple method, direct couplings between multiple parameters are not investigated, but the result returns the level of impact for exactly the investigated parameter. Table 5-2 displays all parameter sweeps based on the initial system, in the range of 50% and 150%. In order to keep the complete back plate corrugated, the corrugation length parameter "L_poly" changes the total number of corrugations along the radius too. This implies 103 rings for the 5 µm corrugation length, and 33 rings for the 15 µm corrugation length.

Table 5-2: Parameter variations between 50% and 150%

Parameter	Minimum (50 %)	Initial (100 %)	Maximum (150 %)
H_Beam	300 nm	600 nm	600 nm
H_Poly	165 nm	330 nm	330 nm
H_SiNi	140 nm	280 nm	280 nm
L_Poly (1:1)	5 µm	10 µm	15 µm
SiN4 pre-stress	500 MPa	1000 MPa	1500 MPa
Poly pre-stress	82 MPa	165 MPa	247 MPa

Detailed results and information according to the parameter sweeps can be found in section 5.3.1. Based on the results and possible technology designs, eight test systems were determined for further investigations. Resulting geometry data of these eight systems are listed in Table 5-3.

Table 5-3: Eight sets of buckling back plate design patterns.

Parameter set	**1**	**2**	**3**	**4**	**5**	**6**	**7**	**8**
H_Beam (nm)	600	600	600	1200	600	1200	2200	2200
H_Poly (nm)	330	330	330	330	660	660	660	990
H_SiNi (nm)	280	280	140	280	280	280	280	280
H_PolyGap (nm)	320	320	460	920	320	920	1920	1920
SiN4 pre-stress (MPa)	1000	1000	1000	1000	1000	1000	1000	1000
Poly pre-stress (MPa)	40	80	40	40	40	80	40	120

The displacement of the eight BBP configurations are displayed in Figure 5-9. Where the flat microphone design represents zero micrometer displacement, the initial system about nine micrometer displacement and the optimal configuration “Set 7” about 34 µm.

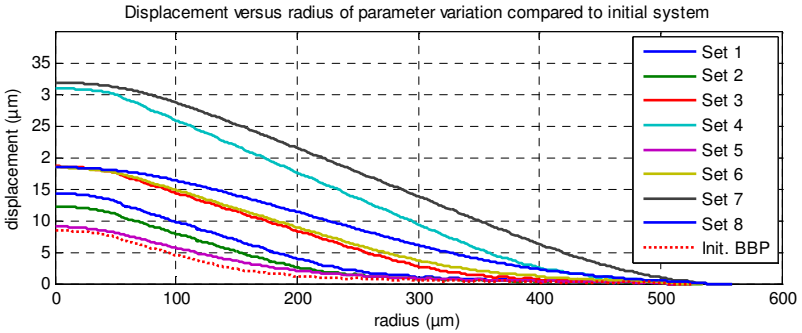

Figure 5-9: Displacement versus radius (buckling shape) of parameter variation compared to initial system.

An automated optimization routine was not implemented, because the fundamental knowledge about manufacturers technology, design processes, and constraints was not available. In addition to this, mechanical couplings of these parameters are also unknown. For this reason the data from Table 5-3 was defined within cooperation and coordination of Infineon Munich, according to the results of Figure 5-10 and Figure 5-11.

5.3.1 Parameter Variation Results

The modular and parameterized FE model was used to investigate the impact of each parameter on the buckling back plate. The evaluation of the parameter variation was focused primary on volume increase and secondary on stiffness increase. The initial system was defined as reference and one by one parameter was changed between 50% and 150%, while keeping the other parameters at the initial value. The relative volume change according to (5.2) is depicted in Figure 5-10, and the relative stiffness change according to (5.2) is depicted in Figure 5-11.

As can be seen, the major parameter for increasing the volume as well as increasing the stiffness is the beam height. This is the main parameter for designing the lever arm for one corrugation ring too. The second important parameters are poly silicon thickness and the intrinsic pre-stress in this layer. The reason for this is obvious, because the softer poly silicon layer represents the mechanical weak point, due to corrugation rings without stiff silicon nitride cover. The volume increase investigation, depicted in Figure 5-10, outlines, that increasing poly silicon thickness and pre-stress, leads to a decrease in buckling – more general: a stiffer and thicker material is stiffer.

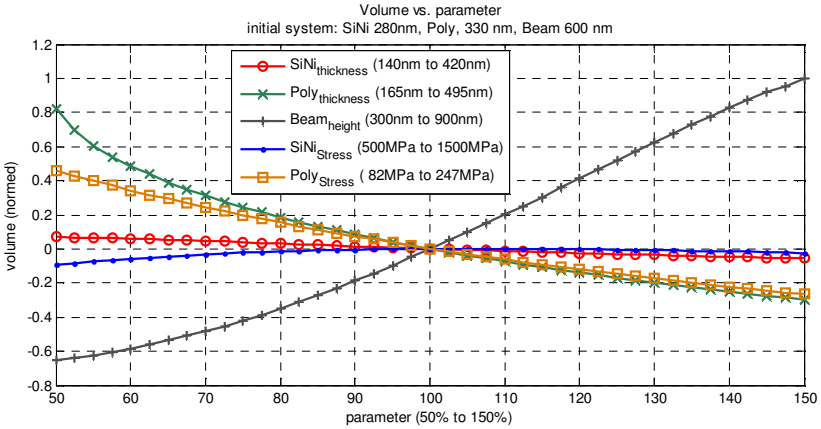

Figure 5-10: Parameter investigation of volume between parameterized system and initial system.

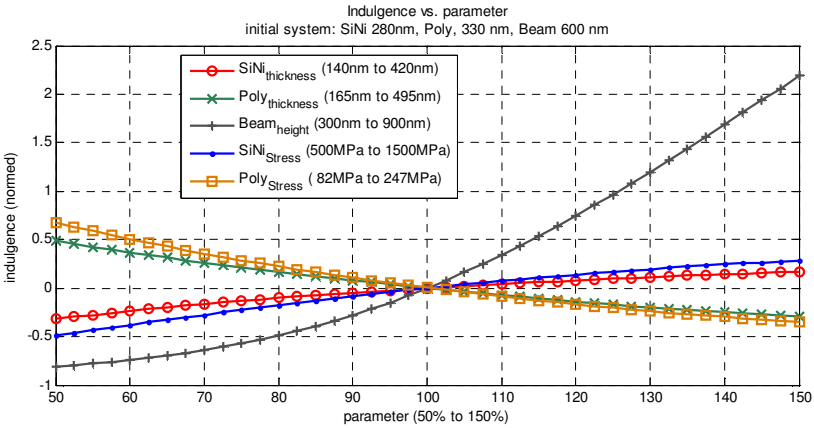

Figure 5-11: Parameter investigation of indulgence between parameterized system and initial system.

The lowest influence on the system can be seen in the silicon nitride thickness and pre-stress value. This is a direct result of the radial separation, from full coating to corrugation rings. The global mechanical strength is lost, due to local weak spots. This effect can be compared to a predetermined breaking point.
Summarized, the beam height was determined as our primary parameter for an increase in volume and global stiffness. Followed by the poly silicon properties, since they define the weak spots at the corrugation rings. Raw data for each parameter sweep can be found in appendix, where the detailed result allocation is listed in Table 5-4.

Table 5-4: Parameter variations between 50% and 150% and corresponding Figures

Parameter	Buckling structure (No Load)	Deformed structure (With Load)	Loaded structure (Δ Volume)	Flexibility vs. radius
SiNi Thickness	Figure C-1	Figure C-2	Figure C-3	Figure C-4
Poly Thickness	Figure C-5	Figure C-6	Figure C-7	Figure C-8
Beam Heigh	Figure C-9	Figure C-10	Figure C-11	Figure C-12
SiNi pre-stress	Figure C-13	Figure C-14	Figure C-15	Figure C-16
Poly pre-stress	Figure C-17	Figure C-18	Figure C-19	Figure C-20

Data for the initial or reference system can be found in Table 5-1, where columns in Table 5-4 have the following relevance: "*Buckling structure*" corresponds with the mechanical structure after the cool down process (no load). "*Deformed structure*" corresponds with the structure loaded with 1 kPa homogeneously (with load). "*Loaded structure*" corresponds with the volume displacement between buckling structure and deformed structure (delta volume). "*Flexibility over radius*" corresponds with the local flexibility information according to (5.1). In this case, the alternating local stiffness of the silicon nitride and poly silicon layers can be seen very well.

If the primary parameter (beam height) is set large and the secondary parameters (poly silicon thickness and intrinsic pre-stress) set low, the resulting buckling system is stiff and shows strong buckling characteristics. Stiff poly silicon with large beam height results in a moderate buckling shape. Table 5-5 sums up volume according to (5.2) and indulgence according to (5.3). Left side is ranked for indulgence decrease and right side is ranked on volume increase.

Table 5-5: Volume increase and indulgence compared to initial system for parameter variation of Table 5-3

Parameter	Volume (%)	Indulgence (%)	Parameter	Volume (%)	Indulgence (%)
Set 7	1035.30	-11.20	**Set 1**	1035.30	-11.20
Set 5	38.20	8.60	**Set 7**	790.90	189.40
Set 8	449.30	21.10	**Set 3**	449.30	21.10
Set 3	299.20	32.50	**Set 5**	339.60	59.50
Set 2	70.10	47.20	**Set 8**	299.20	32.50
Set 6	339.60	59.50	**Set 6**	121.50	82.00
Set 1	121.50	82.00	**Set 4**	70.10	47.20
Set 4	790.90	189.40	**Set 2**	38.20	8.60

5.4 Tradeoff between Volume and Stiffness

As already discussed in previous section, the global stiffness decreases with partially removing the hard silicon nitride layer. The corrugation rings without silicon nitride coating constitute the local weak spots along the radius. From the stiffness point of view, removing the hard SiN4 layer is contra productive, but from volume point of view it is

constructive. Hence, there is a tradeoff between volume and stiffness. Aim for the stiffness versus volume investigation is the optimum lever design for large volume increase including a large total stiffness. Basic idea of the modeling setup was treated already in Table 5-4, while Figure 5-12 displays the simulation path for determining a volume weighted stiffness parameter, referring to the initial system. This method differentiates between a buckling volume without load, and a deformed buckling volume with a load applied.

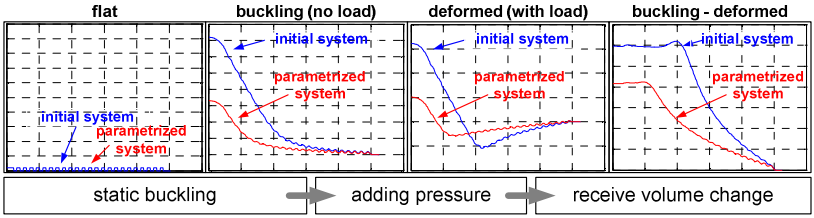

Figure 5-12: Stiffness investigation with volume weighting modeling procedure.

The fist step represents the fabrication step, where the back plate buckles from flat shape to buckling shape. This step can be verified with a white light interferometer measurement, as already depicted in Figure 5-7. These results are investigated on the volume increase level, where the initial system defines the reference volume for comparing the parameterized system volume with

$$\alpha_{\mathrm{V}} = \frac{V\left(u'_{\text{no load}}\right) - V\left(u_{\text{no load}}\right)}{V\left(u_{\text{no load}}\right)} . \tag{5.2}$$

In (5.2) α_{V} denotes the volume optimization factor, u' the parameterized system and u the initial system. The index $_{\text{no load}}$ is relevant to the static buckling back plate shape without external load applied, the index $_{\text{with load}}$ in (5.3) with externally applied pressure on the deformed structure, respectively to determine the volume weighted global stiffness α_{S}, the externally loaded buckling back plate shape is used, where the approximated correlation of (5.1) is suited

$$\alpha_{\mathrm{S}} = \frac{V\left(u'_{\text{no load}}\right) - V\left(u'_{\text{with load}}\right)}{V\left(u_{\text{no load}}\right) - V\left(u_{\text{with load}}\right)} . \tag{5.3}$$

5.5 Multi-Snap-In with Electrostatic Actuation

The flat back plate structure was adapted to the buckling back plate structure with corrugation rings and lever arms. Exactly these weak spots at the leaver arms change the mechanical behavior of the entire structure. The single snap-in point of the flat system, where the total back plate can be represented as a single mechanical spring, is replaced by a multi-snap-in point, caused by multiple corrugation rings. Each of the corrugation rings show different mechanical properties, defined by their length and thickness. A coupled mass spring system with different mechanical snap-in points is the consequence. Figure 5-13 illustrates two different types of buckling back plate systems. The solid line represents our standard initial (reference) system, while the dashed line a system with doubled thickness for poly silicon.

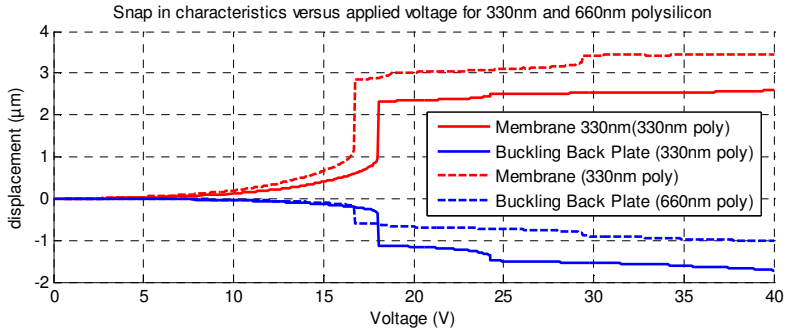

Figure 5-13: Multi snap-in characteristic of two systems, first 330nm poly silicon thickness (solid) and second 660 nm poly silicon thickness (dashed), electrostatically loaded with a linear increasing voltage from zero volt to 40 volt.

Both systems were electrostatically coupled with TRANS126 elements (see chapter 3.5) and a linear increasing voltage up to 40 volt was applied. The blue lines correspond to the back plate center point displacement (top to bottom) and the red lines to the membrane center point displacement (bottom to top). The first and also largest snap-in occurs for the initial system, at about 17 volt. At this point, the membrane is mechanically in contact with the back plate near the edge area. By continually increasing the voltage over the first snap-in level, the membrane and back plate starts to cling in center direction, with

additional snap-in characteristics. The following snap-in points occur with repetitive patterns and decreasing displacement levels, since the system is axis rotational, and no imperfections are included. Increasing the stiffness by doubling the poly thickness, results in reduced maximum buckling. A direct result is a higher electrostatic attracting force and an earlier first snap-in point at 16 volt. Figure 5-13 also displays, that the back plate movement decreases with approximately the same factor as the thickness increases.

The multi snap-in verification utilizes the laser scanning vibrometer as direct method, or measuring the capacity as indirect method. The latter method can be used additionally to check the electrostatic attracting force level, hence this method was applied. Since the back plate and the membrane behaves like a parallel plate type capacitor, the applied voltage results in a gap change and increasing capacity. For this test, the speaker cell was linearly loaded between zero volt and 30 volt. Disadvantage of this method is the global information of the capacity in comparison to the laser vibrometer measurement, where local information can be gained. A detailed description of this measurement method and the setup can be found in [101, 102].

Figure 5-14 compares the measured results with the FE computation. As can be seen the initial capacity before and after the first snap-in matches the computed capacity very well. This implies that the coupled FE model matches with the measured device, including all nonlinearities and parameters set. The slight deviation of the snap-in point are caused by imperfections of fabrication processes. These imperfections result in mechanically local weak spots and shift the snap-in point to a lower voltage or force level. In addition to this, the measured system does not show a release state. This effect was already discovered in [103]. The effect is known as “latching” and is caused by charges in the insulation layer. These charges result in an additional electric field, hence an additional electrostatic force occurs in the system. These charges evacuate very slowly, compared to the mechanical snap-in movement. Measurements (see [103]) have shown, that this effect is also frequency dependent and can last up to days. From measurement and sound generation point of view, this effect must implicitly be taken into account. However, for static FE model verifications is can be neglected.

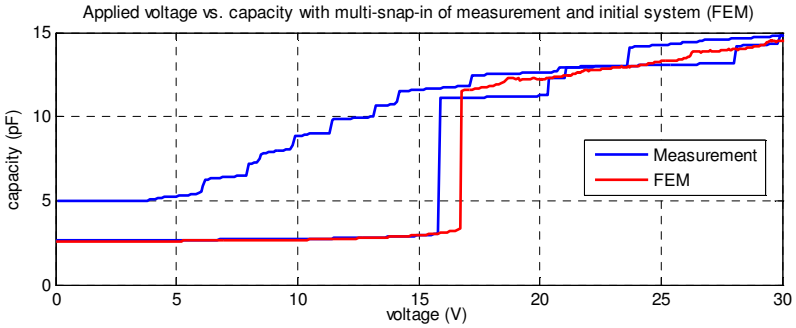

Figure 5-14: Multi snap-in characteristic displayed for capacity versus voltage between FE model result and measurement of fabricated membrane plus lower stator system. Measurement by Infineon Munich.

An analytical model was used to reassess the FEM and measurement results. In this model, the mechanical force is represented by a linear spring, and can be written as

$$F_{\text{me}} = k \cdot (d - u)\,, \tag{5.4}$$

where k is the stiffness, d the initial gap and u the displacement. The electrostatic force derivation was treated before in chapter 3.4.1 in detail, where the direct method (see (3.3)) was used to compute F_{el}. The equilibrium of F_{el} and F_{me} is given up to the snap-in point, where voltage versus gap function is computed. Equating F_{me} with F_{el} and solving for the voltage, results in the snap-in voltage level

$$V(u) = \sqrt{\frac{2k}{\varepsilon_0 A} u^2 (d - u)}\,. \tag{5.5}$$

The analytical model does not include structural nonlinearities and interface forces Therefore the snap-in point occurs exactly at 33% of the available stroke level. Additional information on linear snap-in and multi-snap-in characteristics can be found in [104-106].
The analytical investigation of the first snap-in point was investigated according to (5.5). The result is depicted in Figure 5-15, where the solid line represents the weak system and the dashed line the stiffer system. The stiffer system reduces its buckling by 30% - the FEM result was

used to define the analytical model buckling level. The snap-in point of the 330 nm structure correlates with the measurements and the FE results at about 17 volt. Due to the stiffer system resulting in a reduced buckling, the dashed system snap-in point is about 14 volt and as in the measurements and FEM result below the weak system.

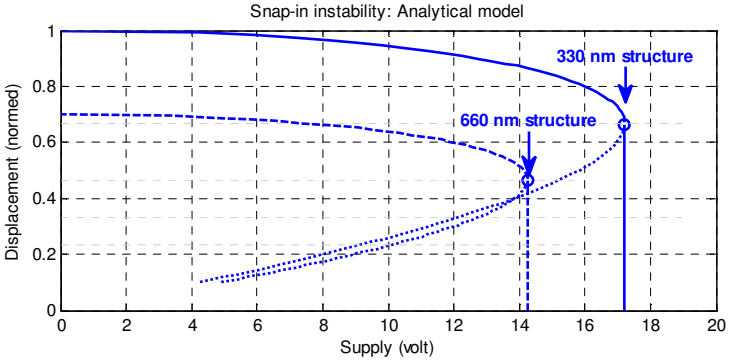

Figure 5-15: Snap-in voltage versus displacement for 330nm and 660nm structure.

5.6 Theoretical Sound Pressure Level Increase

The theoretical sound pressure level, is computed with the volume between the buckling back plate and the membrane. Free field conditions allow the computation of the pressure according to [107] at a distance r by

$$p = -\frac{V\omega^2\rho}{2\pi r} e^{-\frac{j\omega r}{c}} . \tag{5.6}$$

The following SPL results are absolute maximum ratings and referred on the idealized static BBP shape. Idealized in this content means, that the buckling back plate is infinite stiff and the total volume available is used to generate sound. Infinite stiffness is impossible to achieve for the back plate at fabricated devices and a perfectly fitting of the membrane and the back plate too. Therefore, the computed SPL values should just give an idea about the optimization possibilities of an buckling back plate system. Figure 5-16 illustrates the computed SPL for the eight

sets of Table 5-3, compared to the initial system, and the flat microphone design. As expected, the flat design generates the absolute minimum sound pressure level, because of the small volume. The maximum volume increase was reached by "Set 7", with the largest buckling slope (see Figure 5-9). An increase of theoretically +15.43 dB sound pressure level can be achieved with the buckling back plate structure compared to the flat and un-optimized design. Since the computation is based on a single speaker cell, driven in single ended mode, theoretically +48dB can be added for the 8-bit array and additional +6dB for the push-pull or pull-pull driving mode.

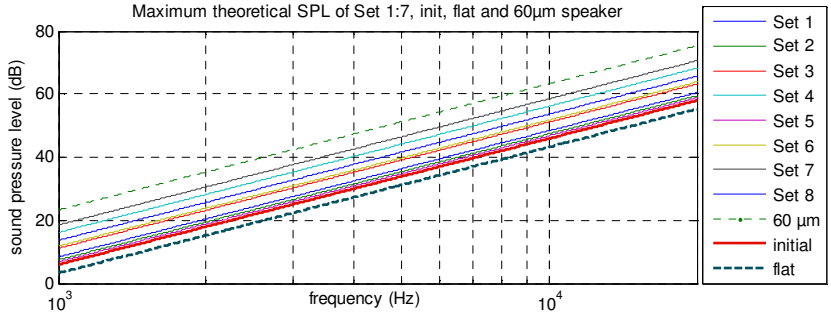

Figure 5-16: Maximum SPL of single speaker cell at 10 mm distance.

"Set 7" defines not the final version of optimized the BBP. Especially in edge areas the slope can be further increased to achieve even higher volumes. Latest fabrication tests have shown buckling back plates with stroke levels of about 60 µm and therefore a three times larger volume compared to "Set 7". The latest buckling back plate design with 60 µm is depicted in Figure 5-17, where the total SPL would increase with +9.5dB for a single cell and with +44.5dB for the 8-bit pull-pull array.

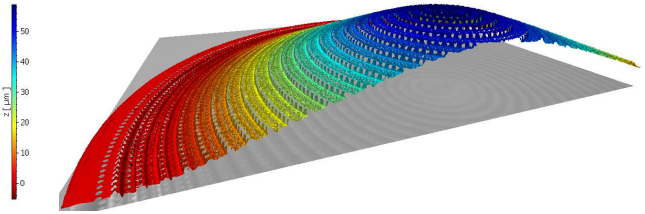

Figure 5-17: White light interferometer measurement of 60 µm BBP.

CHAPTER 6

6 Optimization II: Digital Sound Reconstruction

At the analog sound reconstruction, the audio signal directly controls the membrane movement. A voltage with a frequency between 20 Hz and 20 kHz is applied between the membrane and the stator, as a result the membrane follows the amplitude of the voltage. To vary sound pressure levels in analog mode, the stroke level of the membrane must be adjusted. Large stroke levels result in high sound pressure level (SPL) and low stroke levels in low SPL.

At the digital sound reconstruction (DSR), the active surface correlates with the SPL. To be able to vary the active surface, an array of speaker cells is used. Active membranes are actuated with full stroke level and inactive ones remain at their initial positions. DSR generally will be realized with a big amount of small speaker cells, due to discretization of the analog audio signal and the digital equivalent representation in surface. To achieve a low distorted audio signal, all single speaker cells have to be identically, this is a result of superimposing the pressure over all elements.

6.1 Functional Principle

The size of the array correlates with the resolution in amplitude. If the array has more speaker cells, the resolution from “silence” to “maximum amplitude” is finer. Human auditory has a low-pass characteristic, therefore the recognized sound will be determined

smoother in comparison to the digitalized sound. Steps between increasing or decreasing amplitudes will not be sensed as hard steps, rather than smooth gradients – details can be found in Appendix A.

The input audio signal has to be discretized over time and digitalized according to the bit-groups of the speaker array – information about bit groups can be found in section 6.1.1 in detail. In general, the sampling frequency for digital audio playback is about twice the highest frequency, as described by Nyquist [108]. If not mentioned explicitly, all investigations are using a sampling frequency of 500 kHz, to avoid sampling errors and outline discretization errors in a better way.

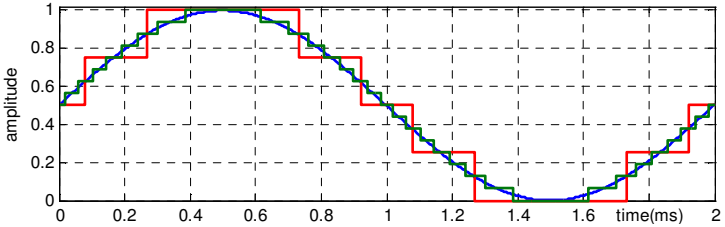

Figure 6-1: Digital sound reconstruction with two bit and four bit for discretization quality comparison.

Figure 6-1 displays a sinusoidal signal, which was quantified with two bits (corresponding to four discretization steps) and four bits (corresponding to 16 discretization steps). A demo pattern for the four-bit array is displayed in Figure 6-2. Left side shows the audio signal and the corresponding digital values and the right side displays the active and inactive membranes. The bit-group pattern is explained in section 6.1.1 in detail.

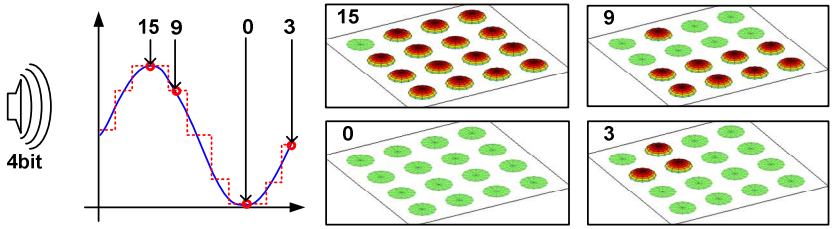

Figure 6-2: DSR of audio signal (left) and active membranes (right).

(The schematically quantification in Figure 6-2 was drawn coarse for better visualization and does not refer to real four bit quantification.) The active bit-pattern of a eight-bit speaker array and an audio frequency of 500 Hz can be seen in Figure 6-3. This pattern will be used to vary the active surface and as a direct consequence the SPL at the point of interest.

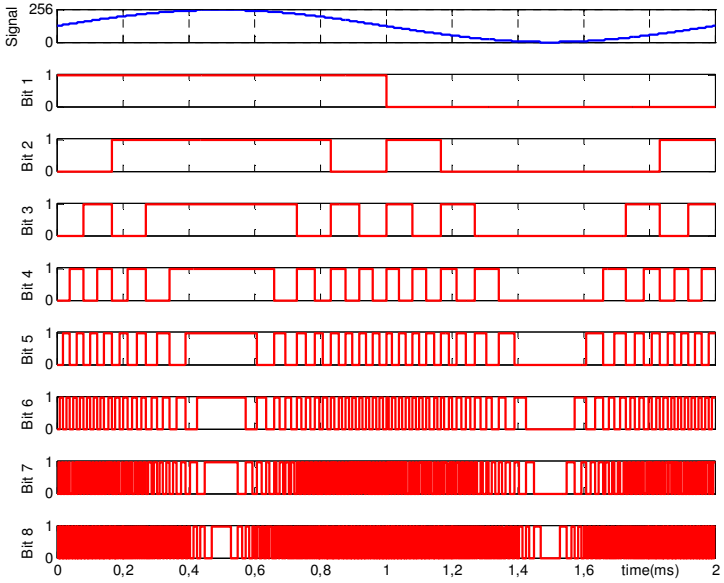

Figure 6-3: Bit pattern of 8-Bit sampling (bit-1... MSB, bit-8...LSB).

As can be seen in Figure 6-3, the LSB changing frequency corresponds with the maximum slope of the digitalized audio signal. Therefore for controlling the LSB membrane, the switching frequency has to be higher, compared to the MSB membranes and is far over the Nyquist frequency.
In Figure 6-4 the importance of the bit-reset is outlined. Since, sound is created by membrane displacement change, the demo bit-pattern (`"167 34 86 255"`) can be interpreted with resetting each bit group immediately (left side) or storing the potential energy of each membrane and transfer it to the next digital value (right side). For the later method, the sound output changes to (`"167 19 46 149"`),

which does not correspond to the original control signal of the bit pattern.

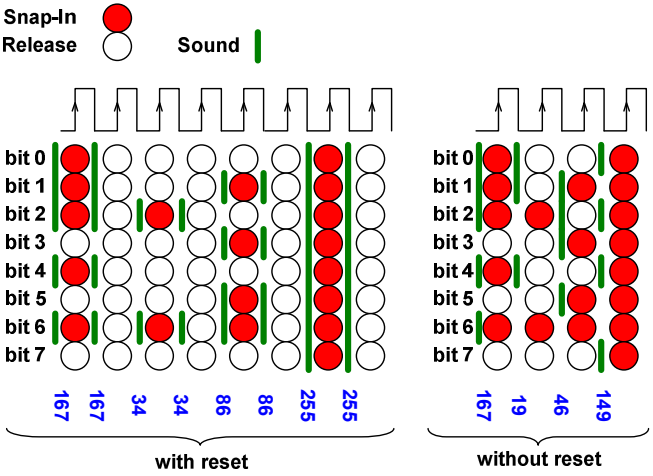

Figure 6-4: Digital sound reconstruction with and without resetting the bits to their initial states.

6.1.1 Speaker Array and Bit Grouping

In the field of digital sound reconstruction usually bit groups are introduced, to easily address the active surface area to the digital audio signal and the output sound pressure level. One example of a bit grouping pattern is depicted in Figure 6-5, where the amount of speaker cells per group increases by the power of two (binary). The smallest area represents the least significant bit LSB and is responsible for the smallest change of amplitude. The biggest group is the most significant bit MSB and is responsible for the biggest change of sound. By introducing these bit groups, the speaker can still be controlled in analogue mode, where all speaker cells gets feed with an analogue audio voltage, hence the movement of each speaker is identically. This establishes the opportunity to mix the analogue driving mode with the surface variation of the digital driving mode, the so called hybrid mode. The big advantage of the hybrid mode is the high quantization depth, because each bit or speaker cell state can be varied from one to zero with analogue mode.

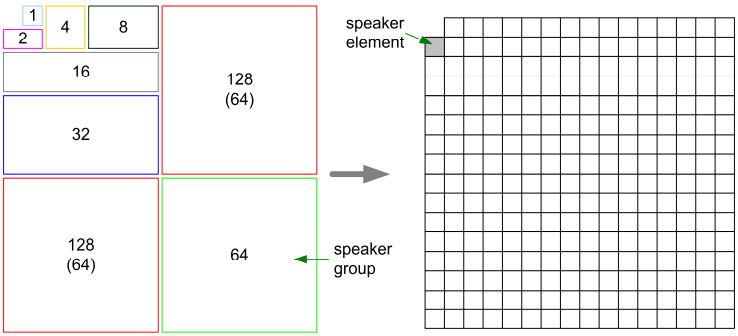

Figure 6-5: Possible bit grouping in an eight-bit speaker array.

Because of the propagation time of the emitted sound waves and the physical dimensions of the MEMS speaker array, THD can occur. The main reason for this THD is the superimposed emitted sound wave. The lowest THD appears in the area of the sweet spot [109], hence the name (see section 6.4.1). This spot is cantered aligned in front of the MEMS speaker array, but the place can be controlled easily by a phase shift or time delay applied on single transducers. The effect of sound wave cancellation and superimposing decreases by decreasing the physical dimensions of the speaker array [110]. The smaller the array the more it can be handled as a point source or single transducer. All simulated and calculated data in this thesis are referred to the sweet spot, if not mentioned explicitly.

6.2 Driving Patterns

As mentioned previously, there are two kind of driving patterns. First the reset mode, where after each digital value all speaker cells get set back to their initial position and second the non-reset mode, where the digital value is generated with the differential signal.

6.2.1 With Reset

The big benefit of this method is the ease of operation, because the digitally sampled audio signal just hast to be parsed directly on the corresponding bit groups. No re-computation of the bit pattern must be implemented for this case. The disadvantage is the additional reset

state of the whole MEMS array, after each step. The bit pattern for this investigation is a linearly increasing SPL slope ("0 1 0 2 0 3 0 4 0 5 0 6 0 7 0 8 0 9 0 10 0 11 0 12 0 13 0 14 0 15 0"). If the up-motion and release movement are identically, the up-motion creates a positive pressure front and the release movement results in an identically pressure front with negative amplitude, hence the total pressure is zero over one step.

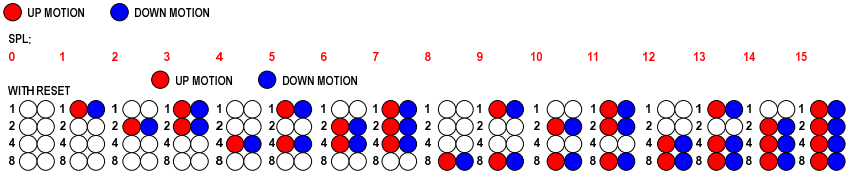

Figure 6-6: Digital sound reconstruction in reset mode.

An example for digital sound reconstruction is given in Figure 6-6. As can be seen, there are four bit groups needed to achieve the maximum output level of 15 with this method. The positive and negative amplitude for each step is displayed in Figure 6-7, where the differential signal for each step is the sum of the up motion and the down motion, hence zero in each case for the reset mode.

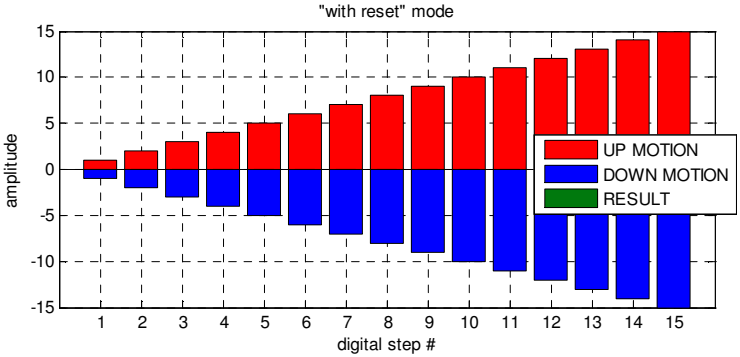

Figure 6-7: Up motion (red) and down motion (blue) of MEMS membrane results in zero SPL in the reset mode of digital sound reconstruction.

This is a direct result of the standard amplitude modulation (AM). The carrier signal with 44 kHz and the audio signal with 500 Hz get multiplied, hence the resulting signal is an amplitude modulated signal. The following assumptions are made for this computations:

- The membrane motion is a sinusoidal piston motion.
- The membrane is able to follow the signal without any delay.
- Each speaker cell creates an identical sound wave.
- All data are computed at the sweet spot.

As a direct consequence the speaker can be seen as an "ideal speaker". In signal theories the addition of two frequencies is also known as DSB modulation (double sideband modulation). The information is located in the two side bands, where the carrier frequency is information less, hence useless data or transmitted energy. An example for this is given in Figure 6-8. More information about signal theories basics can be found in [111].

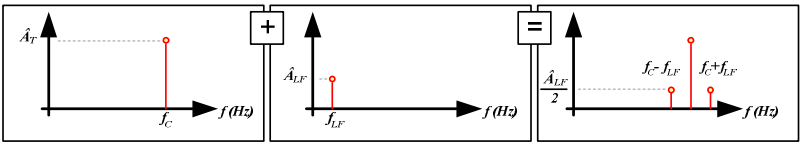

Figure 6-8: Amplitude modulation with addition of carrier frequency and signal, resulting in double sideband modulated signal (DSB).

Simulation data are depicted in Figure 6-9, where a six bit system was driven at 44 kHz carrier frequency and modulated with a 500 Hz audio voltage. Simulation results and signal theories manifest, that there is no sound created in the audio band.

Experiments have shown audible low amplitude signals in this method. The reason is the nonlinear coupling between sinusoidal driving voltage and quadratically distorted membrane displacement. To verify this consideration, the sinusoidal signal was changed to a rectangular one.

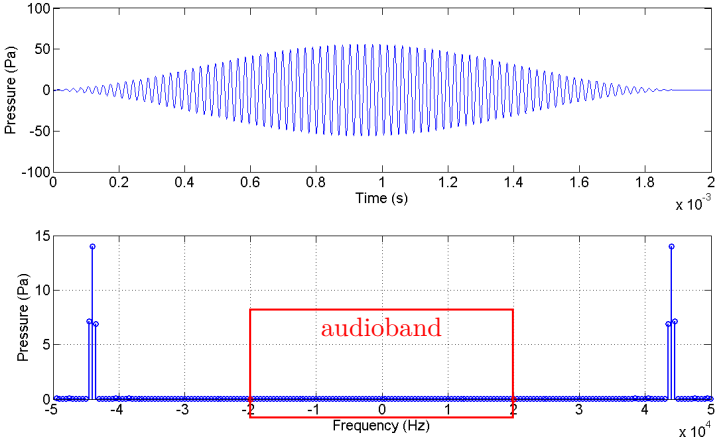

Figure 6-9: 6-Bit 500 Hz sinus modulated on 44 kHz carrier (top) and Fourier analysis (bottom).

The rectangular membrane movement is the worst case scenario for total harmonic distortion viewpoint, because it represents a broadband frequency set. For this test the surface of the positive and negative pulse are equal to achieve no DC bias in the signal. An example for 50% duty cycle is given in Figure 6-10.

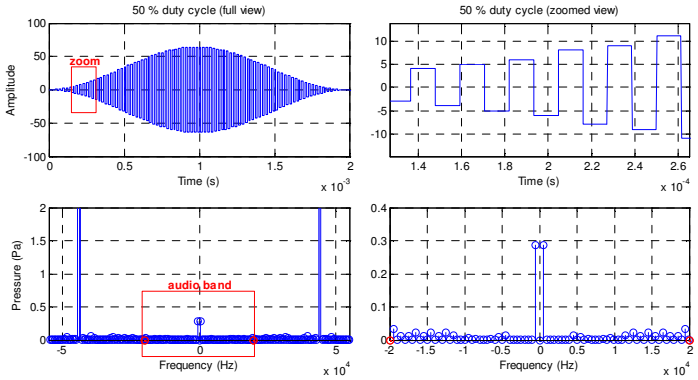

Figure 6-10: 44 kHz rectangular stimulus for 6-bit pattern of 500 Hz sine, with 50 % duty cycle.

Due to the broadband rectangular stimulus, there is an audible signal at 500 Hz. The amplitude is very small compared to the carrier amplitude at 44 kHz. In the next step, the original membrane displacement over time was taken as input parameter for this computation. A laser vibrometer was used to record the displacement data. The resulting pressure is computed as the second time derivative of the recorded displacement as described before in chapter 4.2 (see (4.18)). Figure 6-11 displays the signal analysis of the recorded signal. As in the rectangular shaped stimuli, a small audible peak at 500 Hz and the larger peaks around the 44 kHz carrier occur.

The conclusion for digital sound reconstruction with resetting the membrane in each step is obvious. There is no satisfying possibility to generate sufficient high sound pressure levels at low total harmonic distortion with this driving technology. On the one hand, if the membrane is able to follow a perfect sine wave motion, the acoustic power in audio band decreases to zero. On the other hand, if the motion can be compared with a rectangular motion (like in snap-in and release mode), the total harmonic distortion increases rapidly.

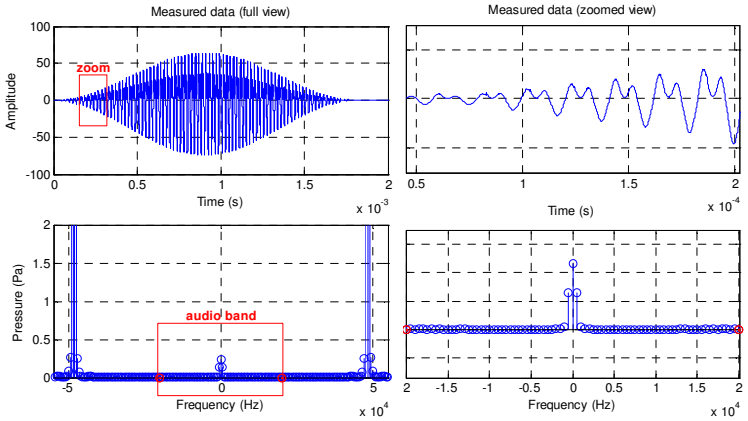

Figure 6-11: Measured membrane movement as input parameter for digital sound reconstruction.

6.2.2 Without Reset

In the first method “reset mode” the membrane was set back to its initial position after each digital bit, which results in a negative and positive sound wave for each cycle. Hence, the total sound pressure over one bit is zero and the radiation frequency is only the carrier frequency with its two side bands. In the second method “without reset mode” the membrane is kept in position until next bit is set; this is achieved with no reset. The potential energy of the set membranes can be carried over to the next bits. As a consequence a pressure offset occurs. This pressure offset can be used to create an audible sound wave. The idea behind this method is simple. The audible sound is not created by the direct movement of the bits, it is created by the stored bits and their carry over. Positive pressure can be created by setting the membranes and negative pressure can be created by releasing the stored or latched membranes. An example for this mode is provided with the same bit pattern as shown in the “reset mode” going from zero to 15 increasing by one. Figure 6-12 displays the membrane movement of each bit group and the resulting carry over bit.

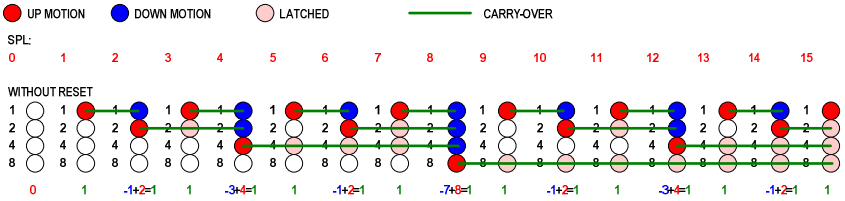

Figure 6-12: Digital sound reconstruction for standard bit pattern without reset after each bit.

Very important for this functional principle is the snap-in and release movement, because they need to be identically to guarantee a wave cancellation. Figure 6-13 displays the positive (red) and negative (blue) sound pulses with its generated bias (green). From this point of view the non-reset mode works for audible sound response.

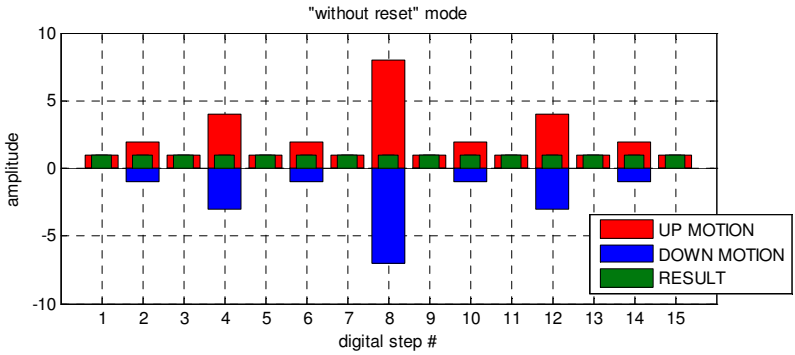

Figure 6-13: Positive (red) and negative (blue) sound pulses generating audible bias pressure (green).

In the next investigation a triangular shaped audible signal with a maximum amplitude of about five bit (in our test pattern a value of 30 peak to peak) and a frequency of 500 Hz was used. The challenge would be easy, if each speaker cell is addressable, but in our case the digital pattern of Figure 6-5 was used to address the speaker cell array binary. Figure 6-14 shows the full switching pattern to check the possibility and feasibility for the DSR without reset method. As can be seen, all eight bits are used to generate the five bit amplitude signal, where each sample corresponds exactly with a change in amplitude. The actual bit-setting depends on the previous bit-settings, because of the carry over of the latched bits. As mentioned before, the LSB (single speaker cell) switches with the highest frequency and the MSB (128 speakers) with the lowest rate. The red bits signalize an up-motion of the membrane, while the blue bits signalize the down-motion.

Another challenge is to locally arrange the large bit groups around the small groups, to increase the size of the sweet spot and decrease the THD in far field as described in [112] or later in section 6.4.

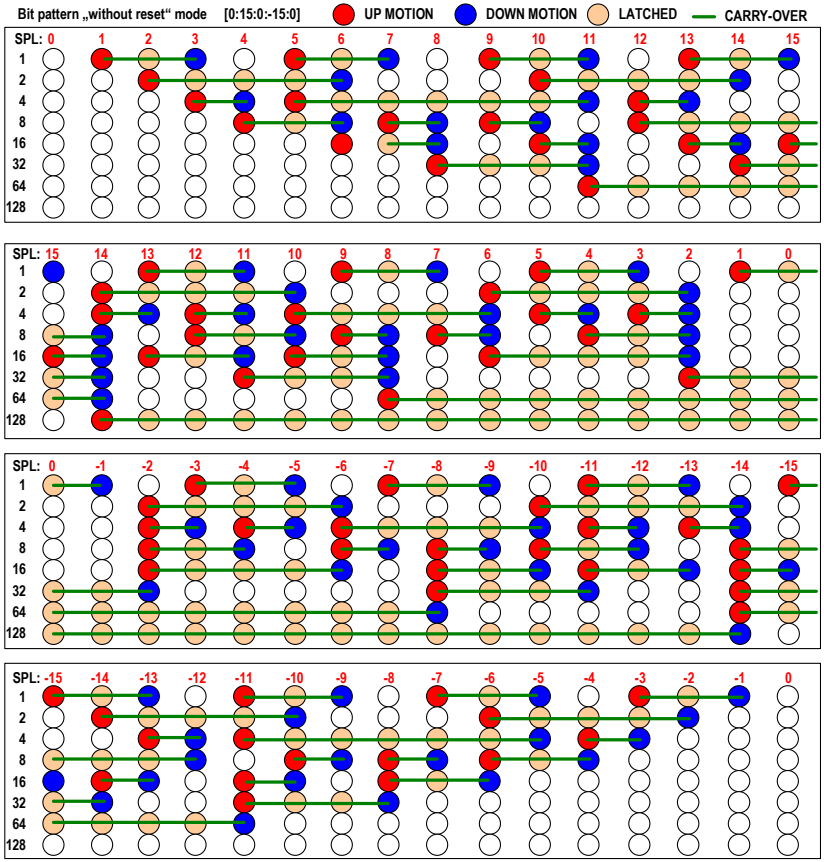

Figure 6-14: Digital pattern for triangular bias pressure signal.

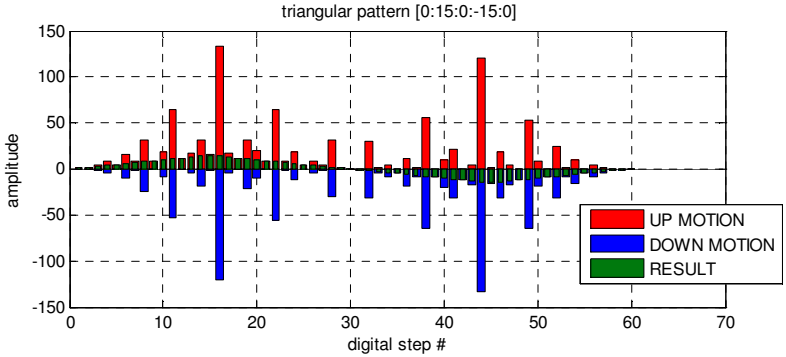

Figure 6-15: Digital sound reconstruction with bias pressure (green) as result of super positioning of positive (red) and negative (blue) membrane movement.

Figure 6-15 displays the positive and negative pressure levels for each digital step. It can be seen, that the full eight bit array is used to create a triangular shaped audible sound with an absolute amplitude of five bit (30 peak to peak). The frequency domain of the positive and negative pressure levels is depicted in Figure 6-16, where the amplitude at 500 Hz increases compared to the previous tests. In the first test, applying the reset method, the audible amplitude at 500 Hz was caused by nonlinearities of the MEMS speaker mechanics and driving voltage. By the help of the reset mode in combination with latching elements, audible SPL can be generated.

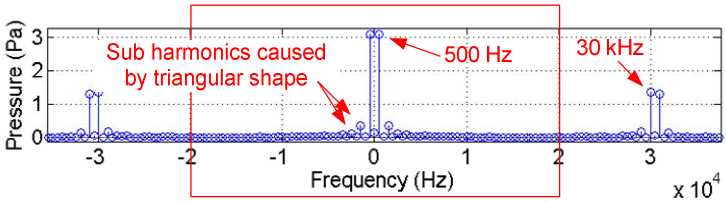

Figure 6-16: FFT of digital sound reconstruction with non resetting mode and latched elements (bias pressure).

In the following sections, simulation results and improvements on SPL and THD are treated in detail.

6.3 DSR Simulation Results

For computing the sound pressure level at the point of interest, the Kirchhoff Helmholtz simulation tool (see chapter 4.4) was used. All investigations were performed with the non-reset method using latched speaker cells, as depicted in Figure 6-14. Latching speaker cells lead to an amount of up-movements or down-movements, depending on the audio signal. Therefore, the speaker array can be fully occupied or latched, if the signal shows high amplitudes in low frequencies. As a result, bit wise grouping patterns are important for increasing digital dynamics. The next challenge for DSR is to find an up-movement and down-movement with low THD to improve the overall distortion of the audio signal.

6.3.1 Amount Cells Available and Quantification

As discussed previously, if the signal shows low frequencies with high amplitude the latched speaker elements limit the acoustical dynamics. To outline this effect, a digitalized sinusoidal signal (left) and the corresponding surface used (right) is displayed in Figure 6-18 in detail.

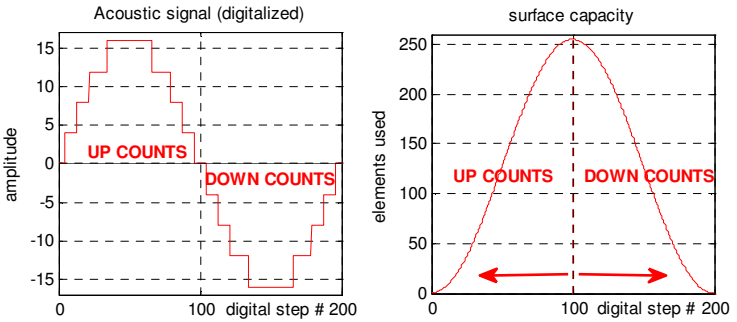

Figure 6-17: Surface capacity (right) of digitally sampled audio signal (left) with up-counts for latched elements and down-counts for released elements.

Generating a positive amplitude leads to new latched elements for each sample. These latched elements can not be used again for positive sound generation. If the sample rate is high compared to the audio signal, the total amount of up-counts increases. As can be seen summing up all up-counts result in the latched surface, while summing

up all down-counts results in the released or available surface. As mentioned before, the worst case scenario is a high sampling frequency and a low audio frequency. Hence, there is a tradeoff between audio quality (high sampling frequency) and SPL (audio signal amplitude). Figure 6-18 displays two audio patterns to outline this effect. The first column indicates the input audio signal, the second column the surface used (of 255 elements) and the third row indicates the output signal (audible pressure). The first signal represents a sinusoidal input pattern, where the amplitude or sampling rate is chosen beneficial. The digital array is able to follow the input signal. The second signal represents a sinusoidal input pattern with higher amplitude compared to signal one. It can be seen, that the complete surface is latched, which results in zero output pressure. Increasing the amount of speaker cells or reducing the sampling frequency can fix this problem.

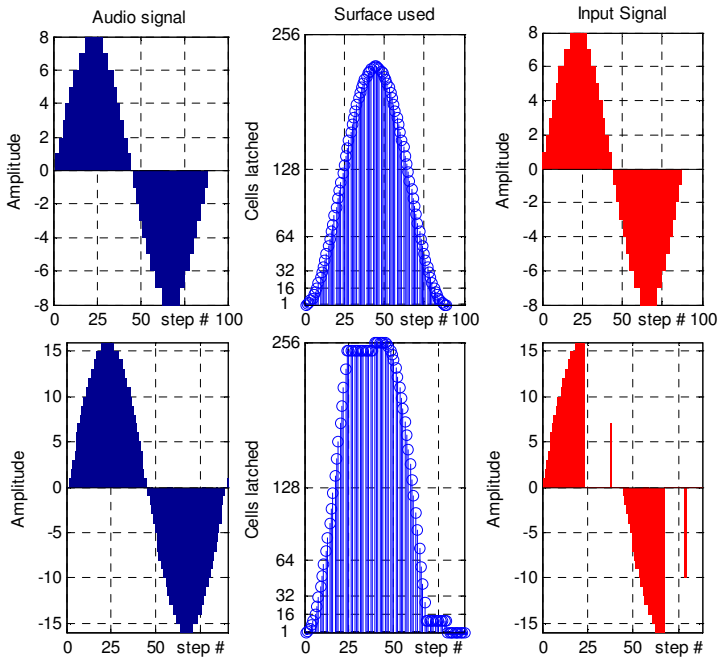

Figure 6-18: Low versus high amplitude sinus (column 1) with latched surface (column 2) and audio output (column 3).

6.3.2 Acceleration Based Speaker System

As already mentioned, the computed sound pressure level is linked to the normal component of the surface acceleration of the MEMS transducer (see (4.18)). Therefore, it is obvious to optimize the acceleration or pressure slope concerning total harmonic distortion and sound pressure level. The idea is to change the standard modeling path from: "*displacement - velocity - acceleration*" to "*acceleration - velocity - displacement*". Audiopixel LTD shows a patent, where they are using a velocity based system [17], which is not totally correct, since the acceleration should be used.

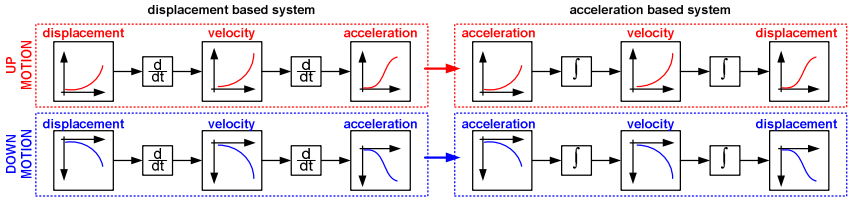

Figure 6-19: Displacement based versus acceleration based speaker system for SPL computation.

Figure 6-19 displays on the left side the displacement based system which starts directly at the membrane motion as the input parameter for the simulation. This motion has to be differentiated two times in order to get the acceleration which is necessary to compute the sound pressure level. On the right side of Figure 6-19, the acceleration based system is depicted. In this system the input parameter is directly the membranes acceleration, but the membrane displacement is needed to investigate mechanical simulation results, hence the acceleration must simply be integrated over time twice.
As described before, the lowest total harmonic distortion is achieved with an sinusoidal shaped sound pressure level. Therefore, an acceleration characteristic of a half sine wave is used in the following investigation. Figure 6-20 displays the sinusoidal shaped acceleration, velocity and corresponding displacement. In this test we are interested in total harmonic distortion, therefore the acceleration amplitude is normed to 1 m/s², which leads to unrealistic displacement results and unrealistic SPL. The switching pattern was computed according the latched element method without reset and wave propagation properties by solving the Kirchhoff Helmholtz integral.

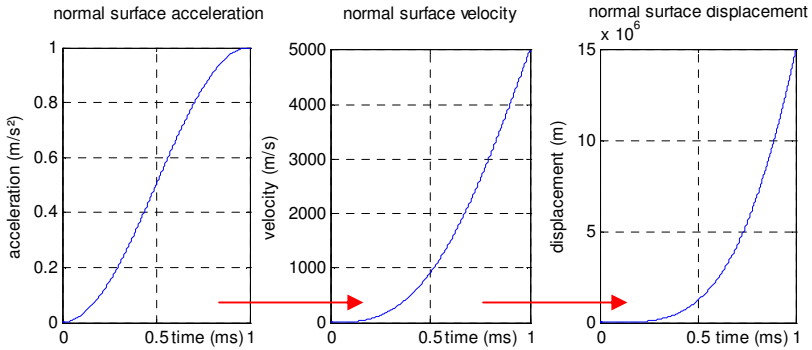

Figure 6-20: MEMS membrane acceleration (left), velocity (center) and displacement (right).

The challenge is to combine the optimized pressure waveform with the latching pattern algorithm. Combining the lathed element method without reset of Figure 6-15 and the acceleration based actuation of Figure 6-20, results in Figure 6-21. It can be seen very clearly, the digital 500 Hz sine pattern with its quantification steps and the distortion peaks at the sampling frequency.

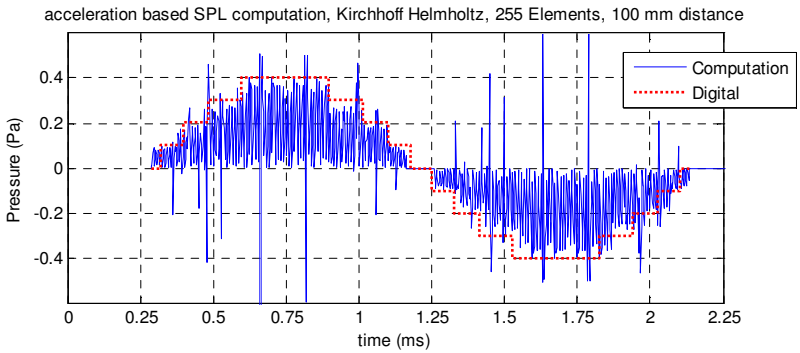

Figure 6-21: Pressure of 255 elements at 100 mm distance, 500 Hz audio signal with 100 kHz sampling.

The three bit acoustic signal can be seen very clearly. Because of the wave propagation delay of each speaker cell, superimposing spikes occur, as investigated by [108] already. This effect increases by the

physical distance between the single speaker cells and decreases with the distance of the point of interest. The frequency spectrum is depicted in Figure 6-22, where the major SPL part can be seen in audible range and around the carrier frequency.

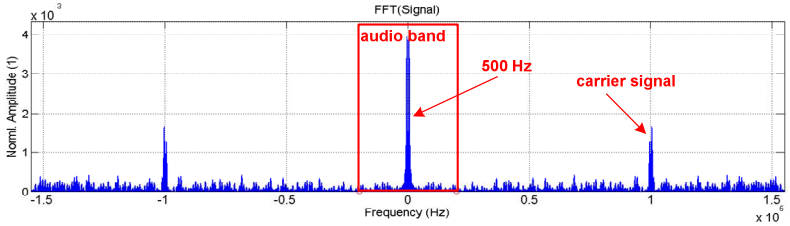

Figure 6-22: Total harmonic distortion at a distance of 100 mm and 255 elements used (ideally optimized).

In the following investigations, the maximum membrane stroke level is limited by the back plate. This represents the snap-in case, where the membrane is forced towards the back plate and stopped abruptly. Therefore, the normal displacement of Figure 6-20 is extended with an abrupt stop and the resulting acceleration is used to compute the sound pressure level at the point of interest. Abruptly stopping the membrane introduces a Dirac impulse in acceleration and decreases the sound quality [113].

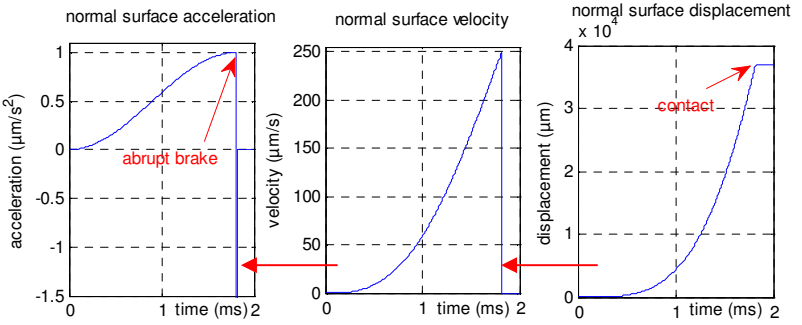

Figure 6-23: MEMS membrane acceleration (left), velocity (center) and displacement (right).

As can be seen in Figure 6-24, the digitally sampled audio signal (red line) shows the same amplitude as in the previous investigation. Stopping the membrane (contact case) leads to a negative acceleration, which has to cancel out with the positive acceleration. As discussed before in the "with reset" mode (see section 6.2.1), the overall sound pressure level cancels out too.

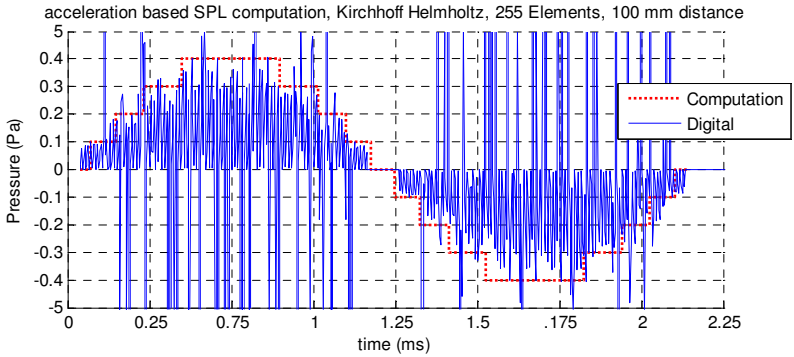

Figure 6-24: Pressure of 255 elements at 100 mm distance driven with contact, 500 Hz audio signal with 100 kHz sampling.

The stopping delay or speed correlates with the damping of the membrane; The faster the membrane stops, the lower the damping and vice versa. From FEM point of view, this effect can be introduced with squeeze film damping and inertial forces, where the latter are small compared to the squeeze film effects. A detailed overview of modeling damping mechanisms is given in [41]. The frequency spectrum is depicted in Figure 6-25, where the 500 Hz signal is superimposed by contact noise.

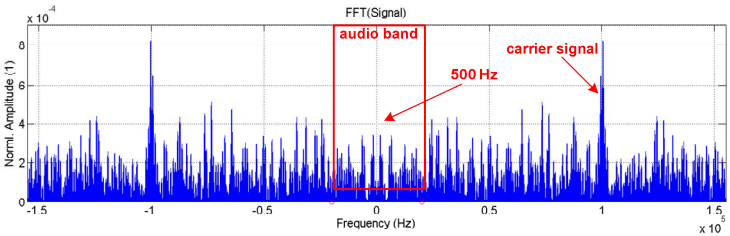

Figure 6-25: THD of DSR signal with contact.

6.4 DSR Optimization Approaches

The following sections give an idea about some optimization approaches from the theoretical point of view.

6.4.1 Bit-Pattern Optimization

Amount of Digital Bits:
As discussed previously, the amount of up-counts is given by the audio frequency and the sampling rate. Since the MEMS speaker used is an eight bit speaker, a theoretically up-count of 255 elements can be performed – the same also holds negatively for down-counts. Increasing the digital array from eight to ten bit enables the possibility of higher sampling frequencies or higher amplitudes of lower frequencies, because of 1023 up- or down-counts.

Eight-Bit Pattern Addressing:
The second main point for optimizing the digital sound reconstruction is the identical behavior of the up-motion and the down-motion to ensure wave cancellation and wave super positioning effects at the sweet spot. The sweet spot describes the focal point between two or more speakers, where the lowest THD of the mixed signal occurs. A detailed discretion about implementing, analyzing and adjusting the sweet spot can be found in [109]. Each digital bit (except the LSB), has its own sweet spot because of its own physical dimensions and acoustic runtime effects. Since all speaker elements of a digital bit are actuated simultaneously, the sweet spot of this bit can not be controlled by user and is given by its physical dimensions and frequency. Nevertheless, the sweet spot can be controlled between the addressable bits as phase shift or delay function. As a consequence, the sweet spot and therefore THD can be improved by addressing more elements. In the conventional eight bit speaker cell, the elements in the array are allocated as displayed in Figure 6-26a.). Each control bit is referenced to a corresponding binary weighted amount of speaker cells. Figure 6-26b.) outlines the optimized pattern. Eight control bits are used to operate the array, but the first two bits define the sector A,B,C or D and the following six control bits refer with the surface are.

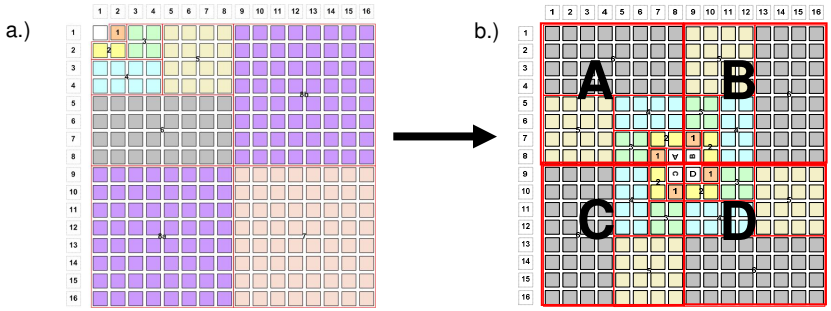

Figure 6-26: Advanced bit grouping example for 16x16 speaker array using eight bit conventional mode and eight bit sector mode (4x6 bit).

Additionally, the LSB elements are located at the center of the array, therefore the distance to the MSB sweet spot is halved. By using the 4x6bit allocation, the flexibility for smaller sound pressure level changes can be improved.

6.4.2 Hybrid Stroke Level Modes:

The MEMS speaker cell is a transducer, which can be operated in digital mode and analogue mode, hence the possibility for a hybrid or mixed mode is obvious. The big benefit of this method is the higher quantification depth compared to the standard digital mode. The quantification depth can be computed by

$$n = x^b , \tag{6.1}$$

where n is the amount of possible quantification steps, x the base and b is the amount of addressable bits available. To give an example; If the membrane position at half stroke level is introduced as additional latched state, the eight bit speaker quantification increases from binary 256 (2^8) to ternary 6561 (3^8). Figure 6-27 displays an quantification example of a sine wave, with binary mode (data bit changes with total bit) and ternary mode (data bit changes with half stroke levels).

Latched elements in hybrid mode must only take full membrane stroke levels and initial stroke levels into account for up- and down-counts, because half states can switch between full and initial state without occupying the bit.

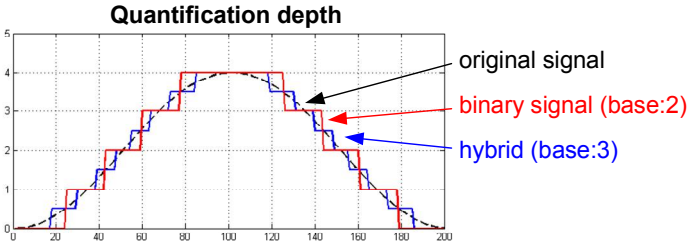

Figure 6-27: Quantification example with base two (binary) and three (hybrid).

6.4.3 Silence-Set-Reset Mode (SSR):

At the SSR mode the displacement change of the moving membranes is controlled. The idea behind this method is to set and reset the latched and free speaker cells so slow, that no audible sound is created. The digital sound reconstruction without reset often uses the small speaker cell areas to create fine increments in sound pressure levels, hence these areas are more often used than the larger ones. The SSR mode requires long set and reset times because of the low displacement change, hence this method is more suitable for larger speaker groups, which are not used very frequently.

While setting or resetting the bit group with SSR method, the group can not be controlled in audio mode, it is occupied. The minimum SSR settling speed depends on the size of the bit group. Larger groups result in higher sound pressure levels, therefore the settling time is slower. In contrast to this, small bit groups can be set faster, because they do not create high sound pressure levels in total. To give an example; 100 Hz or 10 ms, results in 5 $dB_{(A)}$ for 128 speaker elements, while 500 Hz or 2 ms, results in 5 $dB_{(A)}$ for two speaker elements. It can be seen, that two speaker elements can be set five times faster compared to the 128 speaker elements, creating the same SPL. This approach can be combined with the 4x6 bit method, hence the bit groups are smaller in total and the SSR time decreases in total.

Disadvantage of this method is the constant noise created by the moving membranes during the SSR. This method can only be applied in environments, where the ambient noise is high compared to the SSR noise.

6.5 Digital vs. Analog Measurement

As previously described, the reset mode introduces a total reset of each membrane after each digital bit pattern. Using a sinusoidal membrane moving pattern results in audible silence (see Figure 6-9). Therefore, driving the speaker with snap-in characteristics, leads to a highly distorted excitation signal and create audible sound (see Figure 6-10). The same holds for the non-reset mode. In the following investigations, the difference between the reset and non-reset mode, as described in Figure 6-4 is compared. As in previous acoustical measurements, the speaker used is the standard eight bit microphone array inversely operated as speaker. The membrane was loaded with a sinusoidal voltage between 20 V and 5 V (bias at 12.5 V). Due to snap-in characteristics, the membrane movement can be seen as rectangular pattern. In the first test, the eight bit speaker array was loaded simultaneously with a 500 Hz stimulus. The measured microphone voltage is displayed in Figure 6-28, where the snap-in and release peaks can be seen very distinctly.

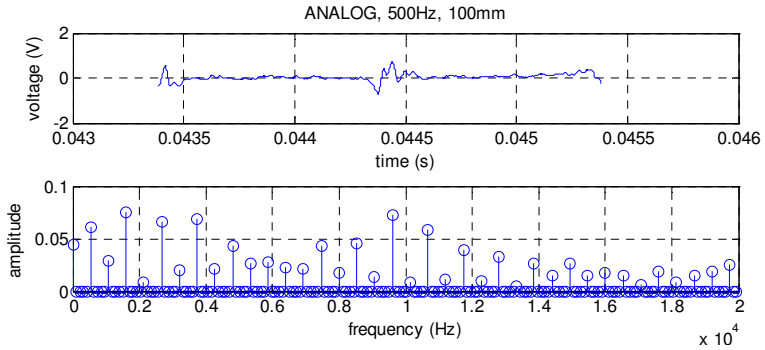

Figure 6-28: Analog sound reconstruction with 500 Hz snap-in driven eight bit speaker array, at 100 mm distance. Measured microphone response (top) and FFT frequency spectrum (bottom).

In the next test, the non-reset method was applied with a 44 kHz stimulus with the same amplitude as in analog case. The digital sound reconstruction was applied on a 500 Hz sinus. The resulting time signal of pressure and frequency spectrum is depicted in Figure 6-29. The peak

at about 500 Hz can be seen in the frequency spectrum, where additionally the higher frequencies are highly developed.

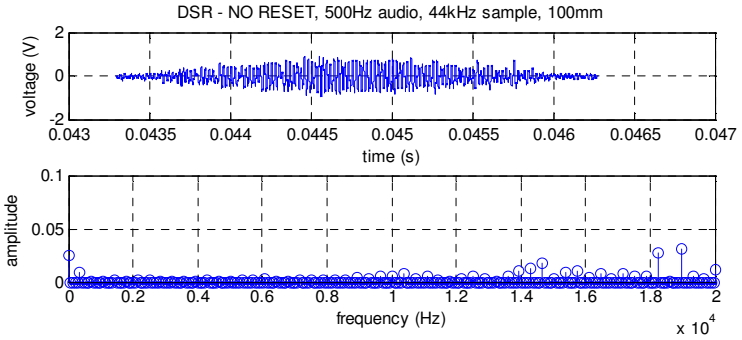

Figure 6-29: DSR with 44 kHz snap-in driven 8-bit speaker array and 500 Hz audio signal without reset (100 mm). Microphone response (top) and FFT frequency spectrum (bottom).

Introducing the reset state after each bit set, brings in higher distortion of the audio signal but increases the sound pressure level. The result is depicted in Figure 6-30. Therefore, we can state that the higher distorted the driving signal, the higher the SPL in audible frequency range.

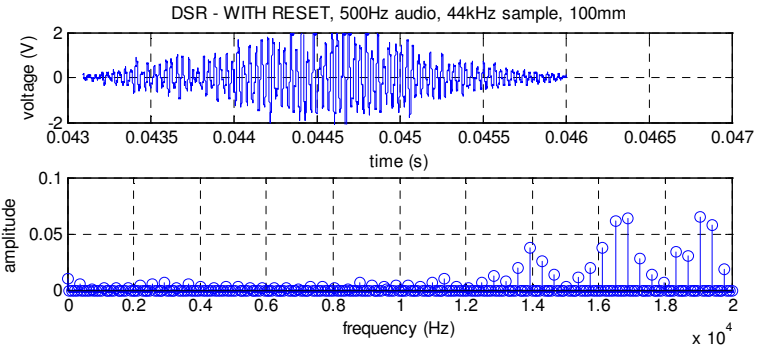

Figure 6-30: DSR with 44 kHz snap-in driven 8-bit speaker array and 500 Hz audio signal with reset (100 mm). Microphone response (top),FFT frequency spectrum (bottom).

CHAPTER 7

7 Summary and Outlook

7.1 Summary

The objective of this work is to model and simulate a MEMS silicon microphone, which is inversely operated as loudspeaker. At the beginning, a model has been developed, which includes and considers all necessary physical parameters and interrelations, to investigate the MEMS speaker towards sound pressure level and total harmonic distortion. As a result, the different operational modes of the speaker were characterized. First, the non snap-in mode, where the driving voltage is low and the membrane stroke level is about a third of the maximum stroke level. Second, the snap-in mode, where the membrane shows mechanical snap-trough characteristics and the full stroke level is used. Because of the fact, that a single transducer is too quiet to generate audible sound pressure levels, an array arrangement was applied. The speaker array opens up the opportunity to apply digital sound reconstruction techniques. Acoustical investigations referring to digital sound reconstruction and sound pressure levels on the full speaker array, were done with the developed Kirchhoff Helmholtz wave field simulation tool. During the modeling process of the single speaker cell, two challenges appeared. The first challenge was the correct implementation of the coupling between the nonlinear electrostatic force and the nonlinear mechanical model, to get an electrostatically actuated

MEMS speaker. The implemented electrostatic force includes both, Coulombs force and the interface force between the insulation layer and air in between the electrodes. Verifications on the electrostatic mechanical interaction were done optically with a laser vibrometer and electrically, reading out the resulting capacity between both electrodes. The correct mechanical movement as the output of the electrostatic mechanical model provides the input parameters for the mechanical acoustical model. In the acoustical model, a determination between the following cases must be done. First, the single transducer or small speaker arrays up to 16 elements and second the full speaker array with its 255 elements. The latter was solely computed with Kirchhoff Helmholtz, because of the computational effort compared to FEM. Single transducer or small arrays were simulated using FEM, where the challenge was on the one hand, the open domain characteristics at the propagation region and on the other hand, the mesh size adaption between nanometer scale in the mechanical acoustic interface and the millimeter scale in the acoustical propagation region. The latter was solved by utilizing Mortar FEM using non-conforming grids. A perfectly matched layer was used to surround the propagation region. By the help of this layer, the impinging sound waves get damped and due to acoustic impedance fitting no reflections between propagation region and damping region occurs. With the assistance of the developed electrostatic-mechanical-acoustic model, two optimization strategies were worked out towards sound pressure level and total harmonic distortion.

The first optimization approach is based on mechanical properties used in the manufacturing process. Since, the speakers back plate is a multi layer structure with various tensile pre-stress, this opens up the opportunity to utilize the stress gradient through the layer. By the help of etching corrugation rings in the back plate structure, the membrane starts to buckle. Hence, stress induced self raising is applied on the structure. As a result, cost economical and flat fabrication results in buckling back plate structures and increase the membrane stroke level possible from two micrometer to 60 micrometer. The major parameters referring buckling height and shape were determined by parameter investigations in the electro-mechanical model.

The second optimization approach is based on acoustics utilizing digital sound reconstruction applied on the eight bit speaker array. On this purpose a digital sound reconstruction demonstrator was developed, which is capable of switching three arbitrary signals to the

dedicated bit groups on the MEMS speaker array. The reset mode is useless for generating sound, except the snap-in case is used to drive the membrane. This is a direct result of amplitude modulation. A further development of the reset mode is presented with the latched mode, where speaker elements were hold in their fully attracted state. The transfer between kinetic energy and potential energy of the membranes between the digital samples, results in an audible sound pressure. The third reconstruction technique is called non-reset mode, where the differential signal between two digital values is emitted as sound, hence it is only useful for pure sinusoidal audio data. Investigations towards sound pressure level and total harmonic distortion were done with the Kirchhoff Helmholtz tool and verified with measurements.

7.2 Outlook

The work described in this thesis contributes to the rapidly growing field of MEMS products, particularly in electro-mechanically actuated transducers. Latest modeling methods are discussed and merged to describe the physical interactions of a parallel plate type electrostatic speaker. Due to its modular based structure, the model can be adapted on other electrostatic speaker structures. The major aim is to develop a speaker system with high sound pressure level and coincidently low total harmonic distortion, where this work presents tools and techniques to investigate on future products. The energy efficient electrostatic speaker can be fabricated in CMOS compatible technology, which opens up the opportunity to fabricate it in parallel with integrated circuits. As a result, smart and energy efficient speaker cells may define a new age of acoustic products.

Particularly on this work, the unsolved questions like “stiffness of the buckling back plate” or the “driving mode at the digital sound reconstruction”, form the fundament of future research. Since only poly silicon and silicon nitride were used in the current speaker system, material analysis makes also a big point in future research.

In the general MEMS speaker question in this thesis, only the electrostatic driving principle was treated. Piezo structures or electro-dynamical driving technologies set up another huge sector for micro-actuators. Prospective investigations may combine various advantages of different driving technologies.

APPENDIX A

A Human Auditory

It is important to understand basics of human auditory and perception, when designing speaker applications. In the following sections a basic overview about the hearing process, ear canal modeling and psychoacoustics is given.

A.1 The Hearing Process: Ear

A brief overview about psychoacoustic effects is given, to understand psychoacoustic effects.

A.1.1 Parts of the Ear

As depicted in Figure A-1, the ear is sectioned in three sections, first the outer ear followed by the middle ear and the inner ear. The outer ear can be separated into the external ear (pinna) and the auditory meatus which is a 2 ccm canal to amplify and focus the audio signal [114]. The dissociation between the outer ear and the middle ear is the eardrum.

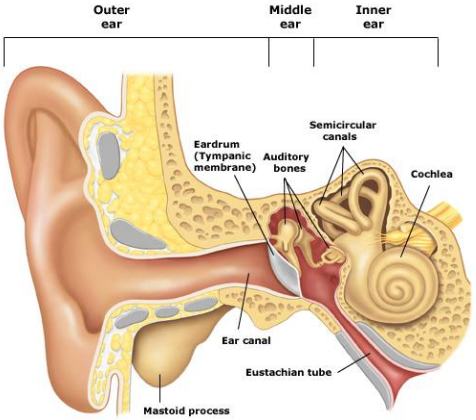

Figure A-1: Cross section of human auditory apparatus [115].

External ear and outer ear:

The main task of the external ear is the localization of sound sources. This is realized with the wrinkled shape of the pinna. These wrinkles induces acoustical resonances, whereby the amplitude depends on the location and direction of the sound source. By analyzing these amplitudes by maxima and minima, the location of the sound source is determined. The working principle can be compared to Yagi antenna systems which are used within EMF localization methods [116].
Additionally, the physical distance between both ears play also a major role for localizing sound sources, especially for low vocal frequencies. At this method the run time delay is used to determine the position and distance of the sound source. Because of the directivity pattern of low frequency sound sources and the large wavelengths, the localization is working more efficient for higher frequencies (starting at 250 Hz - vocals). To give an example: At a common 5.1 home cinema system it is nearly irrelevant, where the subwoofer is located, but it plays a major role to adjust the satellite speakers. This effect is called binaural hearing process and can exclusively be achieved by two fully functional ears. Higher vocal frequencies are sensed via pinna and the auditory meatus, lower vocal frequencies are sensed via skull regions located behind the ear (petrous bone). In tonal threshold audiometry, the hearing threshold level (short HTL) is split up into the fundamental

tone of voice (80 Hz up to 250 Hz), the vocal tones (250 Hz up to 4 kHz) and the consonants (4 kHz up to 8 kHz). In addition to this, the perceived audio path can be separated into the air conduction via eardrum, and the bone conduction via petrous bone.

- *Air condition*: Sound propagation from the external ear in the ear canal up to the eardrum, through the middle ear to the inner ear.
- *Bone condition*: Sound conduction via petrous bone directly to the inner ear. Sensitivity increases for higher sound pressure levels above 75 dB, for this path. Furthermore, low frequency sound (fundamental tones and low frequency sound) is almost fully conducted via this audio path.

The air condition is more sensitive to low pressure fluctuations, but the bone condition is more sensitive for higher sound pressure levels. Additionally, the ambient pressure is only affecting the air condition path. In the field of hearing aids, the DIN EN 60318-5 [117] coupler is the most widespread and commonly coupler used. The construction of this coupler can be seen in Figure A-2, it consists of a cylindrical cavity with a volume of 2000 mm^3 at a tolerance of $\pm$ 70 mm^3. This coupler does not model the ear canal very well, because the real ear canal is smaller in volume and shows another type of cavity. This 2 ccm coupler comes from the time before MRI and can be used as worst case coupler.

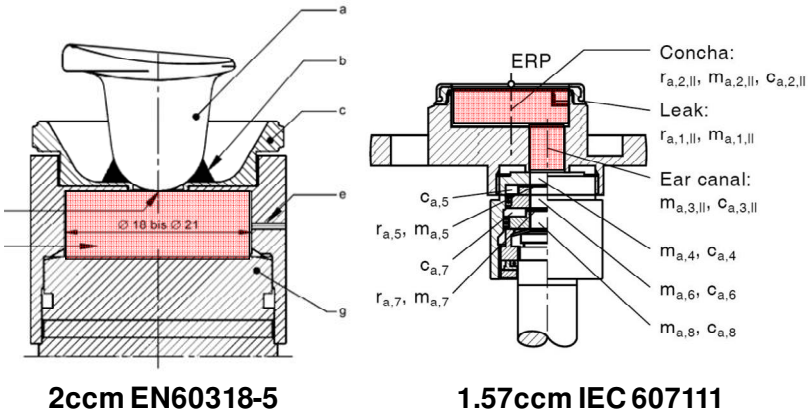

Figure A-2: DIN EN 60318-5 coupler cross section (2 ccm coupler) [117] (left) and IEC 60711 (1.57 ccm coupler) [118] (right)

The 2ccm coupler is too large compared to a real human ear canal. The ear canal model introduced by Brül&Kjaer (also known as the Zwislocki coupler) represents the average human ear with 1.57 ccm, which is more realistic. Data about the smaller and more realistic coupler can be found in [118].

Coupler volume and speaker volume flow:

Volume flow to sound pressure level can be computed by assuming the ideal gas law with

$$pV^{\kappa} = const\,, \tag{A.1}$$

where p is the pressure, V the volume and κ the heat capacity ratio (1.4 for air). Pressure and Volume can be represented by

$$\frac{p}{p_0} = \left(\frac{V_0}{V}\right)^{\kappa}. \tag{A.2}$$

p_0 is the ambient pressure with 101.3 kPa at sea level and 20°C and V the volume flow generated by our speaker or hearing aid. Assuming,

$$p = p_0 \pm p' \tag{A.3}$$

and

$$V = V_0 \pm \Delta V\,, \tag{A.4}$$

gives us

$$\frac{p_0 \pm p'}{p_0} = \left(\frac{V_0}{V_0 \pm \Delta V}\right)^{\kappa}. \tag{A.5}$$

Solving on the alternating pressure level, we receive

$$p' = \kappa \frac{p_0}{V_0} \Delta V\,, \tag{A.6}$$

which can be computed into sound pressure level:

$$SPL = 20 \cdot \log_{10} \frac{p'}{p_{20\mu Pa}}. \tag{A.7}$$

Figure A-3 displays the theoretical SPL, computed according (A.7) as a function of the maximum stroke level of a single speaker cell with 1050 µm diameter. It can be seen, that the smaller and more human like coupler with 1.57 ccm cavity results in a 2.1 dB higher SPL, than the 2 ccm cavity. Sound pressure level correlates linearly with volume flow (2 ccm to 1 cmm results in +6 dB SPL).

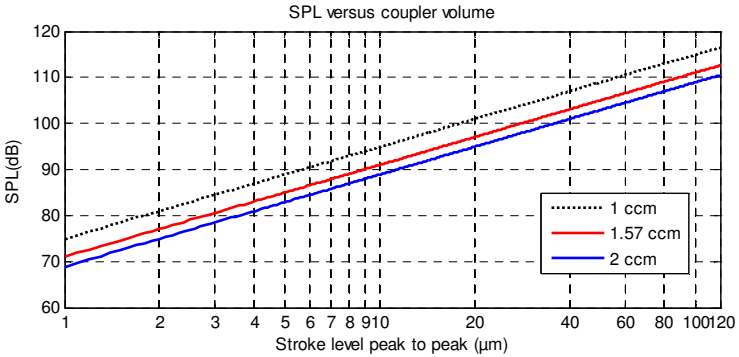

Figure A-3: SPL vs. volume flow as function of maximum stroke (peak/peak) of 1050 µm MEMS membrane

To model the realistic ear canal with its reflections, FEM is used. Fels [98] deals with anatomical investigations and computer tomography pictures of the ear canal right up to geometrically simplifications. To sum up this work, the ear canal can be represented by two cylindrical cavities like they are depicted in Figure A-4.

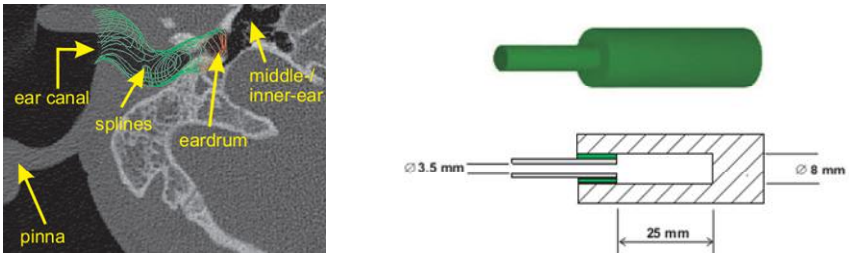

Figure A-4: Computed tomography picture of ear canal (left) and analogue cylindrical cavity model (right) [98].

Middle ear:

The middle ear includes the eardrum (tympanic membrane), the auditory ossicle, which consists of the malleus, incus and stapes. The auditory ossicle is for transferring and amplifying acoustical signals to the inner ear. These three bones amplifies the amplitude of the sound pressure level sensed in the external ear with about eighty to ninety times to the inner ear. The amplification ratio varies for each person. The reason for the amplification is because, until the eardrum, acoustical pressure is propagated in air, the basic hearing system in the inner ear is working with a liquid similar to water. The ratio of acoustic energy transportation from air to liquid is about one percent as can be read in [119]. In order to get rid of wave reflection on the boundary region between middle ear and inner ear, the previous described amplification is necessary. The movement of auditory ossicles can be compared with impedance fittings like they are used in wave reflection termination processes in electronics. This impedance fitting process reduces the wave reflections from about 98 % to 40 %. The resulting pressure in the inner ear region is about 22 times higher, than the sensed pressure on the eardrum, more information about this can be found in [120, 121].

An additional feature of the middle ear is the static pressure compensation between the ambient pressure level and the pressure level in the middle ear. The pressure compensation is the second major task of the middle ear. If a pressure deviation between the middle ear and the ambient pressure takes place, the eardrum starts to bend mechanically inside or outside. This leads to mechanical stress stiffening effects and the dynamic range is reduced. To get rid of acoustically dynamic range losses, pressure compensation can be performed with the Eustachian tube in the middle ear as depicted in Figure A-5. Divers for example need this process to fit ambient pressure with their middle ear pressure – altitude compensation.

High sound pressure levels above 90 dB, results in large stroke movements at the eardrum and a mechanical tension of the two muscles Tympanus and Stapedius which are connected to the ossicles. This muscle tension nonlinearly damps the mechanical oscillation of the eardrum. The contraction of these muscles results in a damping of 10 dB up to 15 dB under 2 kHz for sensed sound pressure. The inertial or initial time for this contraction takes about 200 ms, hence this protection is not useful for bang sound characteristics (very short pulses with high amplitudes). The middle ear can be compared with an

amplifier, which is able to handle offset pressure levels and limit destructive high sound pressure levels

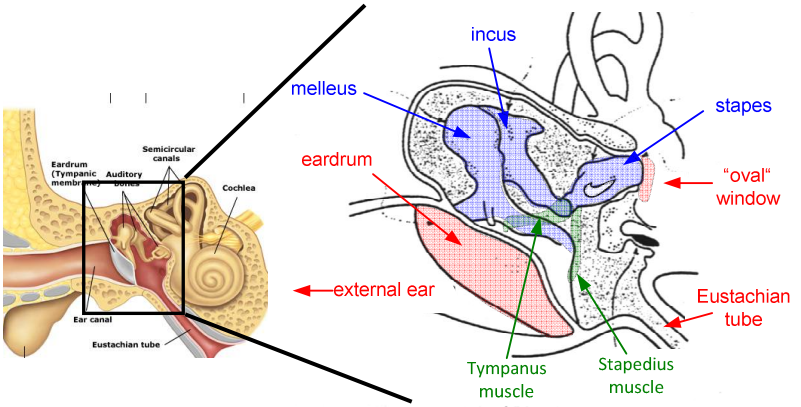

Figure A-5: Middle ear with auditory ossicles, eardrum, oval window and stapes muscles [122].

Figure A-5 displays a slice view of the middle ear with auditory ossicles (marked blue), Tympanus and Stapedius muscle (marked green) for weakening abruptly high sound pressure levels and the link between external ear (eardrum) and inner ear (oval window) (marked red).

Inner ear:

The acoustic signal is amplified by the ossicles as mentioned before and reaches the inner ear through the oval window, where the hearing process starts. The acoustic signal transduction is realized within the Cochlea, a spiral shaped organ with inner hair cells and outer hair cells. The inner ear handles two major tasks, first the neuronal distribution to the specific sensor cells and second, the transformation from the mechanical movement into an electrical nervous signal [121]. As depicted in Figure A-6, the Cochlea is spirally shaped and the slice view shows the inner hair cells and the outer hair cells linked with the tectorial membrane. The mechanical forth and back movement of the tectorial membrane results in an electrical voltage at the hair cells which are handled as nervous signals by brain. The outer hair cells manipulate mechanical oscillations on the tectorial membrane. At the resonance point, oscillations are amplified and next to the resonance position the oscillations are damped mechanically. This effect is known

as cochlear amplifier [121, 123]. The corresponding amplified oscillations on the tectorial membrane, yield to the resulting acoustic sound. The working principle can be compared with Fourier transformation in signal theories.

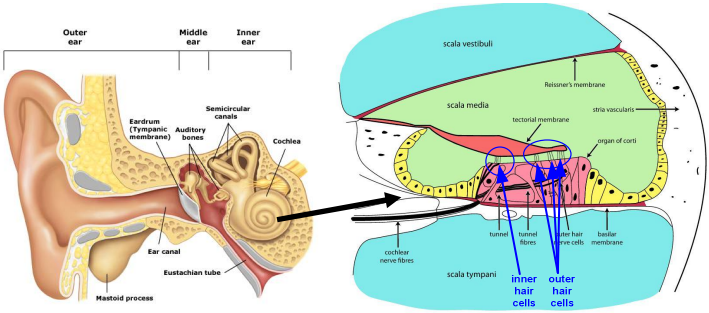

Figure A-6: Cross section of Cochlea (left) [122].

The retransformation out of the structural resonances, into information takes place in Wernicke area (brain area), as described in [124]. The outer hair cells amplify the acoustically stimulated resonances mechanically, the inner hair cells do the transduction between mechanical movement and electrical nervous signal. Hence the inner hair cells are the electro - mechanical transducer elements and the interface to neuronal activity. Each audible frequency band occupies its own nerve fiber. By that way the separation between frequencies can be achieved easily. It has to be mentioned that the audible frequency bands are not linearly rationed over the length of the Cochlea organ and the smallest frequency band is about 3 Hz [125]. In signal theories this effect can be compared with a band pass filter with a gain stage (outer hair cells - cochlea amplifier) and an Fourier transformation (inner hair cells). Important to mention is, that the excitation of a hair cell depends on its prehistory. That implies, if a strong mechanical stimulus occurs past a period of rest or silence, the following nervous pulse will be stronger in amplitude as the same stimulus after a period of noise. Hence, human auditory interprets its sound level based on its historical data. This adaptive gain is very important to counteract an overload in acoustic brain area (Broca and Wernicke area). Exactly that psycho acoustic effect is included in dynamic audio compressions as they are used in modern compression techniques like MP3 or ACC.

As can be seen in Figure A-6 the inner and outer hair cells are connected to the basilar membrane. The information process interacting with the neural fibers is initialized by movements of this membrane. The basilar membrane features a changing geometry over its total length of about 32 mm. On the beginning of the Cochlea, the basilar membrane is slim and thick, and at the end of the cochlea it is wide and thin. As a direct result, the resonant frequency can be seen as a function of stiffness and mass of the basilar membrane.

For low frequencies the mass (at the beginning) and for higher frequencies the stiffness (at the end) is responsible for the amplitude of oscillation [121]. Furthermore, local stiffness varies over the total length starting weak and increasing by factor 100 to stiff [126]. Figure A-7 displays the frequency divisions of the cochlea und the basilar membrane beginning at 20 Hz and ending of 20 kHz. Because of the uniform allocation of the inner and outer hair cells the tonal distribution shows a linear characteristic up to 500 Hz and a logarithmic tonal distribution from 500 Hz to 16 kHz. There are about 3000 hair cells along the membrane, grouped to six heir cells per audible audio band. Below 500 Hz there are approximately 140 frequency bands and between 500 Hz and 16 kHz the remaining 490 frequency bands. The geometrically length for one audio band is about 52 µm, which is the geometric limit for sensing acoustic frequency deviations, from the mechanical resonant frequency point of view. If the place of a mechanical induced oscillation shifts to the neighbor band, at least six equidistant hair cells will be excited.

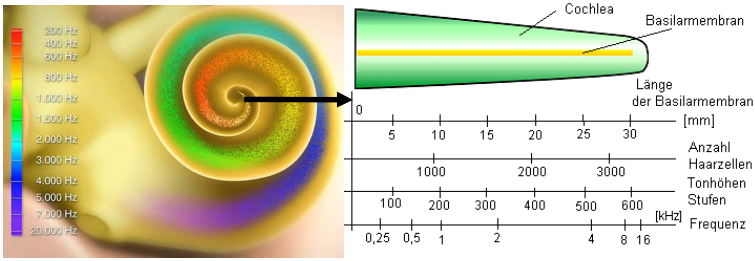

Figure A-7: Cochlea versus resonant frequency distribution over length [120, 126].

Acoustic neurons feature a repetition delay of approximately 250 µs, which corresponds to an frequency of 4 kHz, while human auditory is able to sense frequencies up to 20 kHz. To decode frequencies above

4 kHz, phase shift decoding techniques are used between the six hair cells of each audio band. The brain computes the highest common factor of these six hair cells and determines the correct sensed frequency by this way. More information about hair cell arrangement and corresponding frequency responses can be found in [120, 124, 126].

A.2 Psychoacoustics

This chapter deals with human auditory system as the final receiver in sound recording. It is important to understand the working principle and psychoacoustic effects, to be able to increase the quality of perceived sound or "undistorted" sound. Three main scopes as described in [21, 127-129], were selected. First critical band rate, second level or specific loudness and third temporal masking.

A.2.1 Critical Band Rate

A sound can be inaudible or masked in the presence of an other louder sound. Acoustic masking plays an important role in human auditory in the field of psychoacoustics. Simultaneously masking can be explained on the following example: If a conversation between two individuals takes place and suddenly a second sound source (in the same frequency range) superimposes the conversation (e.g., truck passing by, lawn mower, siren,...), the conversation is disturbed and no information is passed. To continue the conversation and keep the flow of information between both individuals, the voice level has to be adapted on the new ambient sound pressure level. To give an additional example, there is a similar effect while listening to music. Softer instruments become audible, only if the loud instruments pauses or reduces its level, exactly this effect is used in MP3 coding technology also (for more information see [128]). In the field of psychoacoustics the critical band rate scaling is introduced, to separate human auditory into frequency bands which are more related to human perception.

Figure A-8 displays the auditory threshold with a high pressure level stimulus at 300 Hz, resulting in a masked frequency band between approximately 70 Hz and 8 kHz. Additionally two low level sounds at 100 Hz and 700 Hz exists in the audio band. The 700 Hz tonal signal is propagated and can be recorded by a microphone, but for human perception it is inaudible. The 100 Hz tonal signal is audible for human and can be measured by microphone, because it is aligned outside the masker threshold.

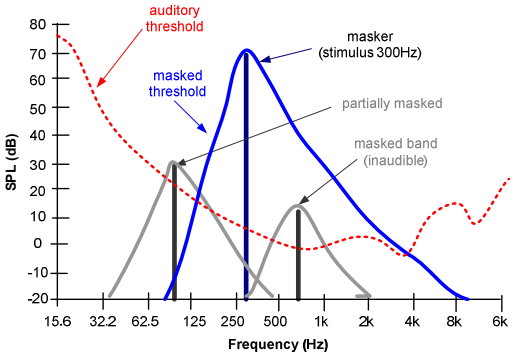

Figure A-8: Example of sound pressure level versus frequency with audible threshold, masker and masked sound.

The audible frequency range is separated into 24 bark bands. These 24 bands have been determined by direct experimental measurements on: (1) the threshold of complex sounds, (2) masking, (3) perception of phase and most often on (4) the loudness of complex sounds. It has to be mentioned that the critical bands must not be linked to the same frequency range over lifetime and person. The subdivision into critical bands seems to be correlated very closely to the cochlear mechanism. A more detailed derivation and determination procedure for these critical band rates can be found in [129]. Figure A-9 displays an example of the critical band rate versus audible frequency range, where each band has its own center frequency and separate bandwidth. For center frequencies up to about 500 Hz, the critical bands are linearly aligned , while for center frequencies above 500 Hz the alignment is logarithmic. This is a direct result of the mechanical setup of the basilar membrane. A single pure tone excites a finite region on the basilar membrane. The basilar membrane is a continuous organ, so it would be impossible for a single point on it to move. Even a single pure tone must excite a finite region, which covers resonant peaks of neighbor frequencies. This is exactly the reason why masking occurs. The effect of masking is linked to sound pressure level as discussed before, hence it has to be treated as nonlinear effect with hysteresis.

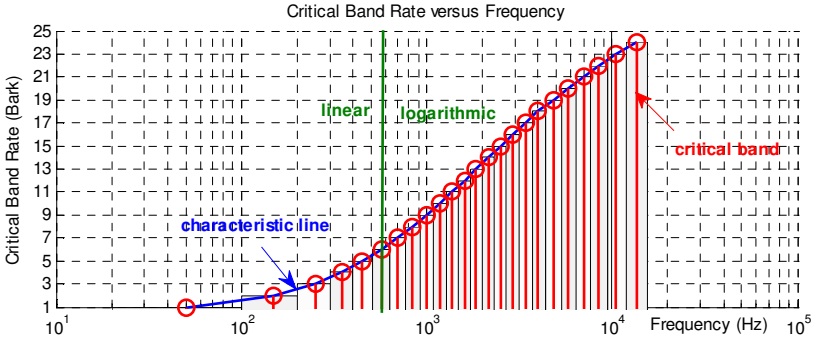

Figure A-9: Frequencies defining the limits of auditory critical bands, characteristic line is an equivalent ear model.

As depicted in Figure A-10, the masked threshold decreases rapidly toward higher frequencies for low and medium masker levels and decreases slowly for high sound pressure levels. The non linear rising slope of the masking threshold is a direct result of the working principle of the inner ear. The outer hair cells, which are for manipulating the mechanical oscillations on the basilar membrane, are more effective for lower oscillation levels and gets saturated for high levels (these saturations results in circulatory disorder of the hair cells, and can result in mortification of the hair cells right up to a permanently hearing defect).

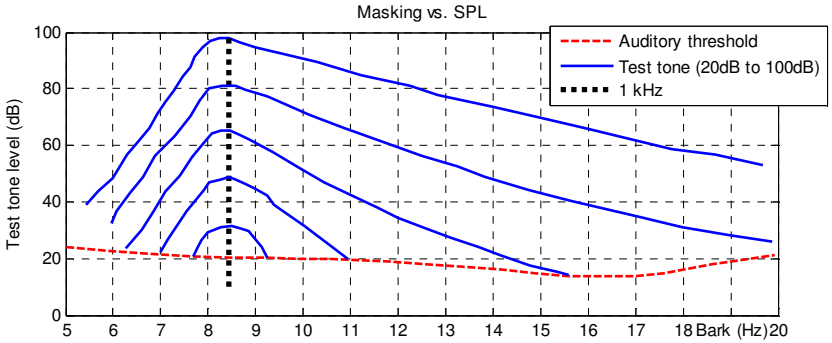

Figure A-10: 1000 Hz pure tone masking frequency versus SPL and resulting masking threshold (raw data: [130]).

The psycho-acoustical tuning curve (inverse function) can be determined by keeping the level of the test tone fixed, while increasing the marker level slowly pending the test tone appears inaudible. More detailed information about various measuring procedures and various models of masking effects referring to basilar membrane characteristics can be found in [127, 129, 131, 132].

A.2.2 Level and Specific Loudness

To describe specific loudness or level, in the field of human auditory, two physical units need to be introduced. First unit is the so called *phon*, which is the psychoacoustic level unit and relates the indeed SPL in dB with the psychoacoustic perception. The nonlinear coherence is depicted in Figure A-11 in detail. Perception starts at 3 phon at 1000 Hz which is the auditory threshold ($\Delta 3$ dB). The non linear relation between pressure level and specific loudness can be seen in Figure A-11.

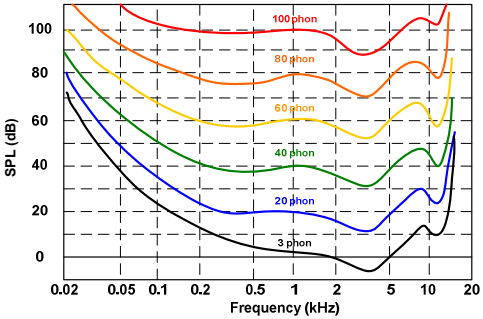

Figure A-11: Psychoacoustic loudness (phon) versus frequency (kHz) versus sound pressure level (dB) [133].

The A-weighted filter is based exactly on the assumption, that not every tonal frequency is perceived with the same intensity. The concrete challenge in this hypothesis is the assumption on perceiving pure tonal signals. Pure tonal signals result in mechanical oscillations on the basilar membrane with a finite expansion, as mentioned before. Hence, masking as well as nonlinear SPL perception must be taken into consideration in order to model human auditory in an accurate way. As a direct result the second unit is introduced, named *sone*. This unit represents the perceived loudness of a sound signal and links the

perceived loudness with the emitted SPL in decibel. One sone is defined as a 1000 Hz pure tonal signal at a sound pressure level of 40 dB. Two sone are perceived exactly twice as loud as one sone and stands for 50 dB (again at 1000 kHz). The loudness versus specific loudness can be found in Table A-1.

Table A-1: Level and specific level: Sone vs. dB scaling

Sone	1/64	1/32	1/16	1/8	1/4	1/2	1	2	4
dB	9	11	14	19	25	32	40	50	60

4	8	16	32	64
60	70	80	90	100

By the help of the specific loudness and the critical band rate, each signal can be represented as a perceived audio signal, like it is handled within human auditory. Figure A-12 displays on the left side, an emitted 1000 Hz pure tone signal, with its masking threshold and two perception marks for one sone (blue) and two sone (green). On the right side, we see the data like it is perceived in human auditory.

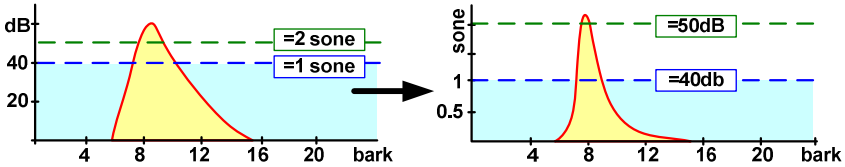

Figure A-12: Loudness signal (left side) versus specific loudness signal (right side).

To sum up; Frequency bands have to be expressed by critical band rate (see bark) and sound pressure level by specific loudness (see sone) to describe human auditory with perception. Furthermore, temporal effects must be taken into account to introduce the time varying specific loudness versus critical band rate pattern, which supplies all the necessary information for evaluating our auditory system.

A.2.3 Temporal Masking

The biggest impact on digital audio broadcast as used in MP3 comes from temporal masking mechanisms, where pre-masking and post-masking effects are used.

Pre-masking is not fully evaluated as described in [127], hence details can only be provided for post-masking.

Post-masking results from the release of the masker tone, because masking does not abruptly stop with switching off the masker, it still stays for a while. The stored kinetic energy at the basilar membrane resonance place must be transferred into potential energy again. Another reason for this effect is the blood flow in the inner and outer hair cells, which is not abruptly stopped. The effect of post-masking depends on the duration, as well as the level of the masker tone. To give an analogy, this effect can be compared with a discharge function of a capacitor. The more energy was stored in the electric field, the longer it takes for the capacitor to reach a level of zero, by switching off the supply. An example for temporal masking is given in Figure A-13, where a 200 ms masking tone was applied on top and a 5 ms tone on bottom side.

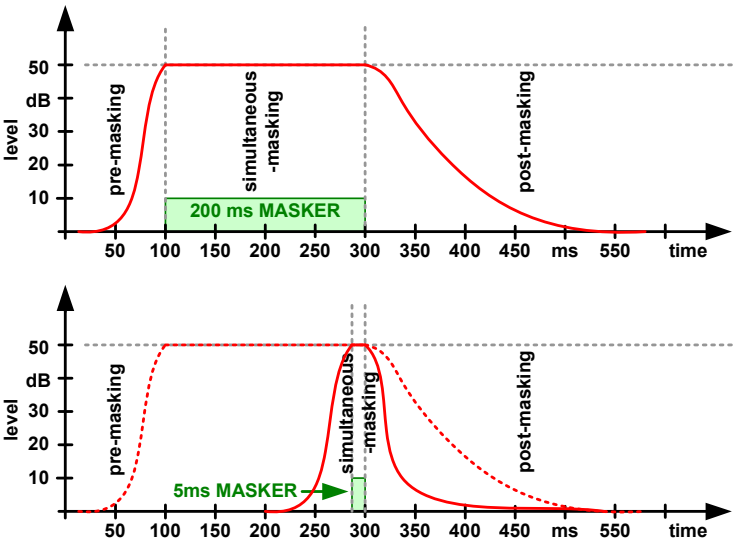

Figure A-13: Temporal masking, pre-masking, simultaneous-masking and post-masking for 200 ms (top) and 5 ms (bottom) simultaneous masking .

The rising-slope characteristic of the pre-masking level for both bursts is the same. However, for the post masking the characteristics changes: A short duration of the masker tone (bottom) leads to a fast decay in threshold, hence the threshold in quiet is reached sooner for shorter

masking periods than for longer masking periods. The 200 ms simultaneous masking signal leads to an approximately 200 ms post masking effect, where the short 5 ms simultaneous masking signals reaches the threshold of audibility past 50 ms. Temporal masking deals with three important facts as described in [132]:

- The hair cells are most sensitive at the beginning of sounds, right past neutral phase.
- The hair cells take a finite time to recover their full sensitivity (temporary paralysation or saturation).
- The magnitude of the perceived sound depends on the duration of the sound.

The basilar membrane in combination with the outer hair cells (cochlea amplifier) describes the psychoacoustic characteristics between physical (radiated) sound and perception. Hence, this acoustical path must be modeled or taken into consideration for designing speakers, especially in in-ear devices or hearing aids.

A nice fact is also, that the brain masks out constantly stimulus of the outer hair cells. The blood flowing around the regions of the inner ear induces sound too. This effect can be amplified and made audible again by listening into a cup or small box (can be compared to the sound of ocean waves). This blood flow noise is filtered out by our brain.

APPENDIX B

B Demonstrator Setup

In the following sections, the hardware and software of the eight channel analog amplifier, called "Demonstrator" is explained. This demonstrator was developed to investigate digital sound reconstruction and the snap-in driving mode.

B.1 Demonstrator Hardware

As already treated in chapter 6, digital sound reconstruction (DSR) requires eight separate analog voltage supplies. Each bit requires its own supply, which is switched on and off, depending on the current DSR status. The demonstrator is able to switch three input signals (A,B and C) with each output (1 to 8), where two of them (A and B) can be amplified up to 27 volt and input C can be connected to an external bias voltage or grounded. This opens up the opportunity, to use two different pre-distorted signals, one for the up motion and one for the down motion of the membrane. Each output has its own gain stage and offset compensation, hence the operator can compensate possible variations between the bit groups at the speaker array. We have to mention, that the acoustic signal part is routed within a separate hardware layer in the printed circuit board (PCB) and shielded additionally. As a result, environmental influences can be damped and signal crossover from the digitally switching parts on the PCB can be reduced and bypassed. Since digital sound reconstruction can imply complex and large switching patterns, the user can pre-

compute them in MATLAB and save them to a SD or MMC card. The demonstrator automatically detects the SD or MMC card and starts to read the text file called *MEMS.txt*. Additional information about this file and procedure can be found in section B.2 – software. A 20x4 character LCD display is used to visualize the user feedback about current runtime or depict additional information. An schematically overview of the demonstrator can be seen in Figure B-1.

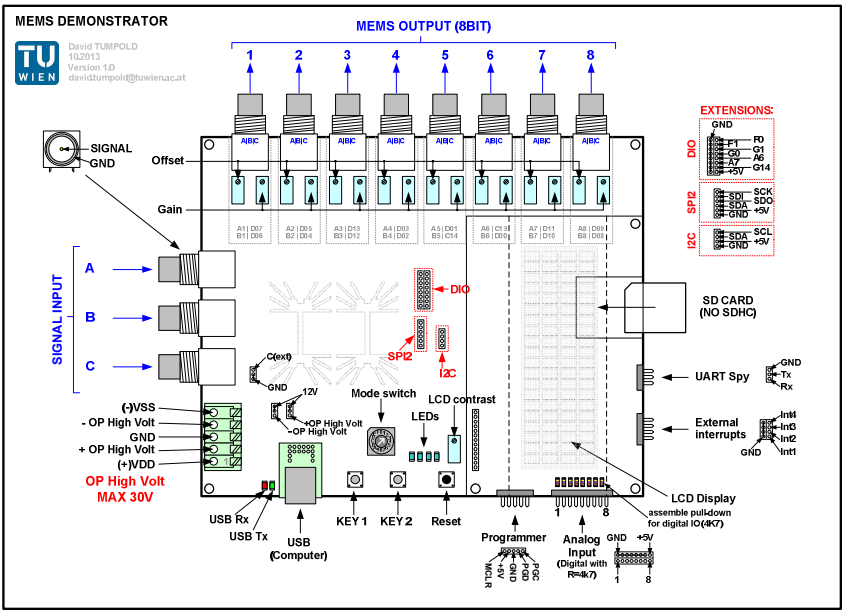

Figure B-1: Schematically overview of hardware components and features of the MEMS demonstrator.

To be able to trigger external devices like wave form generators or oscilloscopes, four external interrupt pins are available. These hardware pins can be used either as trigger output or input. Eight analog inputs can be used to read back the capacitive feedback from the eight bit-groups of the MEMS speaker. A 12-bit analog to digital converter is used to sample the eight pins semi simultaneously. Semi simultaneously in this context means, that the first four pins (1 to 4) and the second four pins (5 to 8) are sampled simultaneously and the controller alternates between them in each sampling period. The demonstrator

can also be used as standalone measurement device, where the eight analog inputs save their values in 12-bit digital raw data (0 to 4095) on the SD or MMC card. All recorded data is stored in *ANALOG.txt* on the storage card or streamed via USB port.

The demonstrator hardware is modular based, this implied extensions using SPI, I2C or UART can be added easily.

B.1.1 Demonstrator Hardware Features

Since we are using operational amplifiers (op-amp) to amplify the input voltage level to the output voltage level, ripples in supply voltage are directly amplified too. In addition, the bias point controlled by the offset compensation using a simple voltage divider, changes too. As a consequence, to minimize the error resulting from the power supply, the ripple must be minimized. Figure B-2 displays the hardware used for generating all voltage levels necessary.

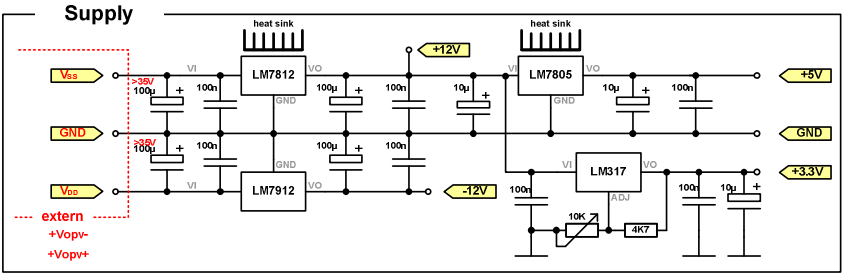

Figure B-2: Demonstrator supply block hardware.

Digital switching parts like the controller (dsPIC) or USB communicator (FTDI) need five volt as supply, the input can go up to 30 volt because of the operational amplifiers. We used linear modules as the commonly used LMxxxx series. They provide low ripple output at large loads and can be used space-saving without large electrical wiring. The advantage of these modules is as mentioned before, the low ripple and high power, where the disadvantage is the loss between the input and output voltage. The higher the difference between input and output, the higher the thermal stress on the device, hence a two stage regulations was applied. In the first stage, the input voltage (up to 30 volt) is controlled to twelve volt and in the second stage from twelve volt to five volt and 3.3 volt. Since the demonstrator is modular based and the total amount of power is therefore unknown, heat sinks were

added to the twelve and five volt controller. In current operation mode, without using additional hardware, driving the MEMS speaker at 30 volt (peak to peak), 200 mA are needed, which results in about 35°C on the heat spot.

In Figure B-3 the signal routing and switching of the three input signals A, B and C (EXT or GND) can be seen. This block is implemented eight times in parallel, since the speaker array is an eight bit speaker.

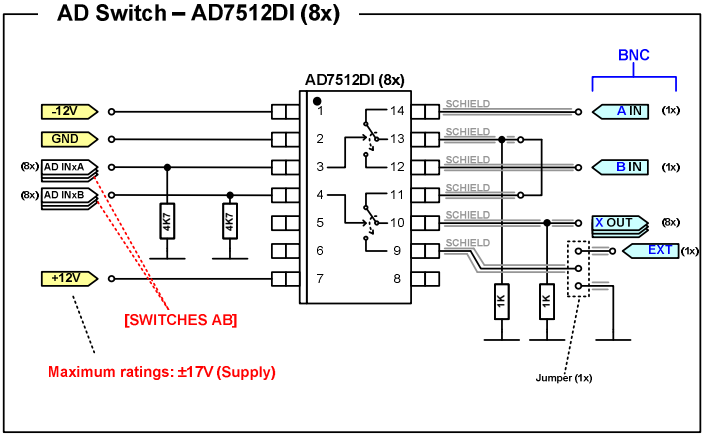

Figure B-3: Signal routing with analog switch.

The important thing to mention at the AD-switch is the shielded routing of the audio signal, which can be seen on the right side. The input signal is in the range of 20 mV to 250 mV for analog audio mode, which represents the worst case due to low input voltage levels. This levels are amplified up to 30 volt, hence crosstalk or environmental effects can affect the signal quality significantly. The control inputs are directly linked witch the signal processor (dsPIC) and pulled down, to define signal C or GND as default.

To amplify the switched signal to the MEMS voltage level, a high speed operational amplifier in non-inverse operation was used. The supply level can be chosen by operator with an external power supply up to 30 volt or switched with two jumpers constant on twelve volt. The latter is a low ripple supply, as described previously, and should be used to investigate non-snap-in moving characteristics or pre-distortion.

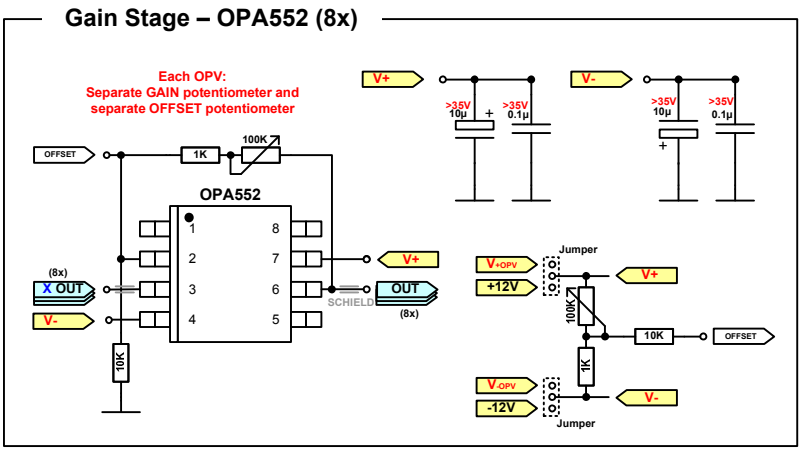

Figure B-4: Gain stage with operational amplifier and adjustable supply voltage.

On the input voltage the offset voltage is added, hence the bias point can be controlled. As in the AD-switch, the gain stage is implemented eight times additionally. Digital sound reconstruction can require sampling times up to 200 kHz as described in section 6.3, the operational amplifier can go up to twelve MHz and the AD-switch was tested at 400 kHz, without losing signal quality on the output.

The SD MMC card interface requires 3.3 volt while the controller (dsPIC) requires five volt. As a result, level shifters were used as depicted in Figure B-5. The low cost alternative solution is a simple voltage divider (five volt to 3.3 volt), but the problem is the parasitic inductivity of the resistors. This inductance acts contrary to the fast rising and falling edges of the digital signals for the SD or MMC card. Since high speed data transfer between the controller and the SD or MMC card are necessary to be able to switch all AD-switches in time, the voltage divider possibility is insufficient. By changing the voltage dividers with the level shifters, the communication bus speed between controller and SD or MMC card increased from 315 kHz to 20 MHz. (20 Mhz is the maximum possible speed derived from the external crystal of the dsPic and correlates to approximately 1.5 Mbit/sec data transfer speed)

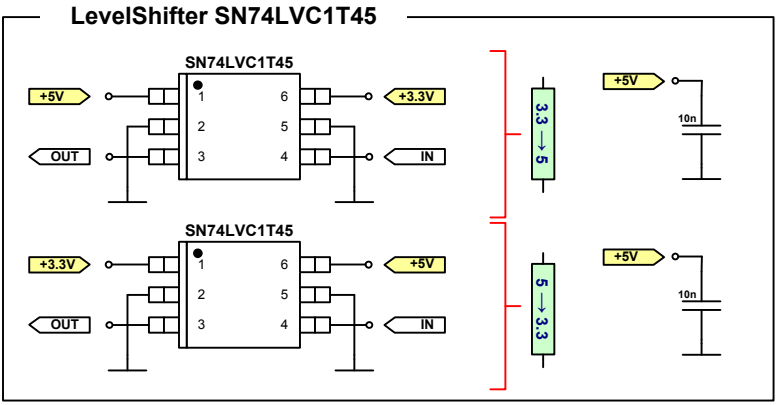

Figure B-5: Level shifter from 3.3 volt to five volt (top) and five volt to 3.3 volt (bottom)

The wiring plan of the SD or MMC socket and the controller (dsPIC) can be seen in Figure B-6 with the level shifters of Figure B-5.

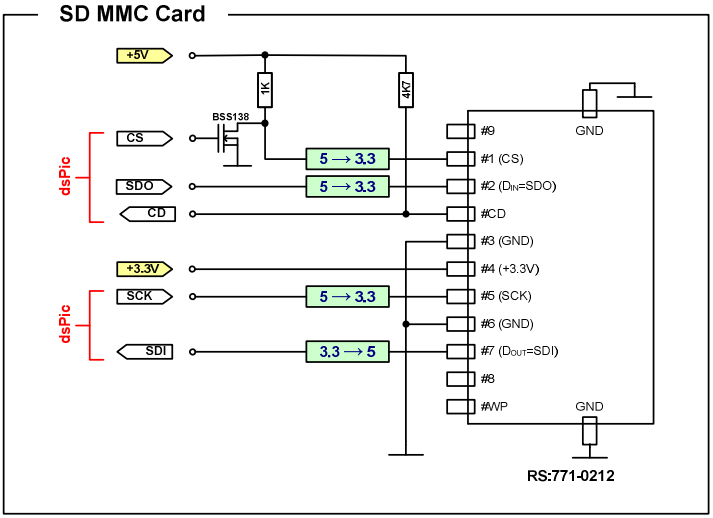

Figure B-6: SD/MMC card connection plan with level shifters.

The heart of the demonstrator is the controller, where a digital signal processor (dsPIC30F6014A) is used. The pin diagram with its peripheral connections are depicted in Figure B-7. The choice on this controller was based on the one hand with the digital signal processor core, where fast and repetitive tasks (switching the AD-switches) can be fulfilled easily and on the other hand due to large possibilities of external peripheral connections. The latter opens up the opportunity of modular extensions for further investigations, while the core supplies large amount of computational power.

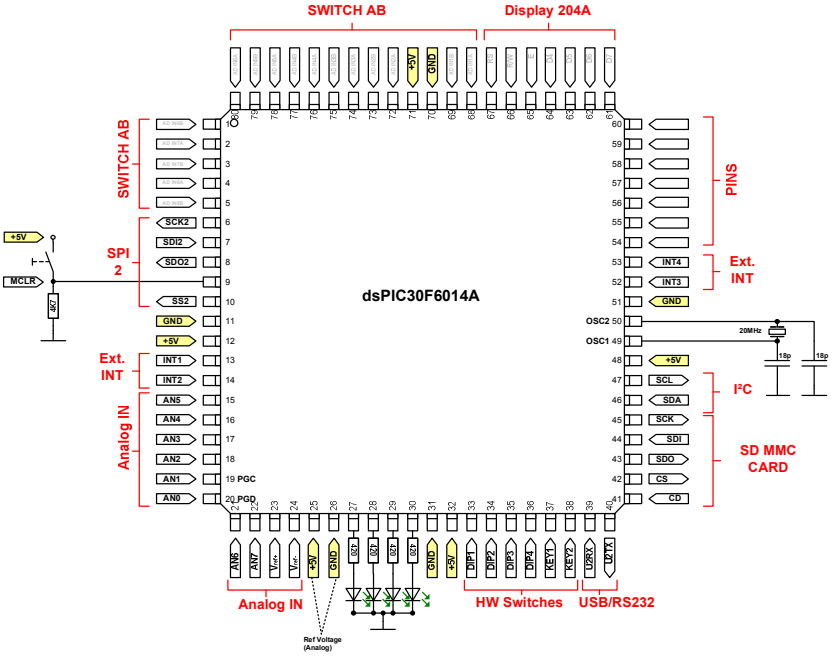

Figure B-7: Digital signal processor with its connections to the peripherals.

NOTE: The reference voltage on the analog to digital converter was connected to the five volt and GND level of the supply voltage. The advantage is, that ripples on the supply cancel out, but the disadvantage is that all recorded data are referred to five volt with twelve bit accuracy, therefore the smallest change in voltage on the input is about 1.2 mV – maybe an external amplification is required.

B.2 Demonstrator Software

The demonstrator software is not treated in detail for each subsequence, because of its scope. Hence, just the major points are discussed as follows. Figure B-8 displays the two main threads used in the demonstrator software.

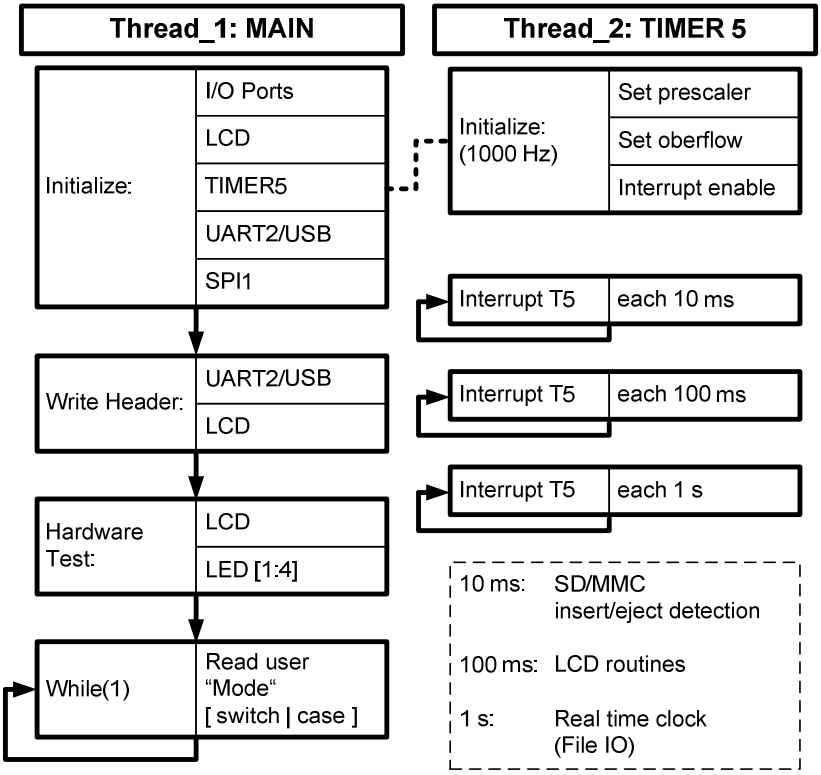

Figure B-8: Demonstrator software threads, main loop (left) and hard beat timer (right).

In the first thread the main routine is executed, starting at an initial sequence, where all input and output pins are defined and set to their initial values. Followed by an initial routine for the LCD controller. After this, the second thread is initialized, which is used as heart beat

timer to synchronize peripheral extensions and the software flow. In the last initialization routines, the universal asynchronous receiver/ transmitter (UART) communication is established, which is necessary to communicate via USB with a computer. The serial parallel interface (SPI) is used to communicate with the SD/MMC card.

The initialization routine is followed by a routine, writing firmware information via USB and on the LCD, to visualize the user the latest firmware used.

Before reading the mode switch position and loading the corresponding program (see section B.2.1), a hardware test is applied on each peripheral used and the four user LEDs flash once, if everything is okay. Finally, the mode switch position decoder is fetched repeatedly, hence the software executes its various modes.

B.2.1 Demonstrator Software Modes

In the following sections a description of all 16 implemented modes is given. Switching from one mode to another can be performed at any runtime, however the first execution depends either on hard beat timer or the SD/MMC routines.

Mode [0]: This mode is visualizes the working principle of the LCD controller and the four user LEDs. It represents an output test.

Mode [1-6]: These modes are not programmed or implemented.

Mode [7]: This mode corresponds to digital sound reconstruction using “latched element” method. The Latched element method of section 6.2.2 is hardcoded for a sampling frequency of 44 kHz and an acoustical frequency of 500 Hz. External interrupt number one (EXT_INT_1) alternates for each 500 Hz switching pattern as trigger pin.

Mode [8]: This mode corresponds to digital sound reconstruction using “with reset” method. The “with reset” method of section 6.2.2 is hardcoded for a sampling frequency of 44 kHz and an acoustical frequency of 500 Hz. External interrupt number one (EXT_INT_1) alternates for each 500 Hz switching pattern as trigger pin. The results can be seen in Figure 6-29.

Mode [9]: This mode corresponds to digital sound reconstruction using "without reset" method. The "without reset" method of section 6.2.1 is hardcoded for a sampling frequency of 44 kHz and an acoustical frequency of 500 Hz. External interrupt number one (EXT_INT_1) alternates for each 500 Hz switching pattern as trigger pin. The results can be seen in Figure 6-30.

Mode [A]: This mode switches input channel A on each output. (ideal to equilibrate all amplifier and gain stages). Analog sound reconstruction can be applied, using this mode. The results can be seen in Figure 6-28.

Mode [B]: This mode switches input channel B on each output. (ideal to equilibrate all amplifier and gain stages). Analog sound reconstruction can be applied, using this mode. The results can be seen in Figure 6-28.

Mode [C]: This mode switches input channel C or ground on each output. (ideal to adjust the bias point or analyze the output on voltage ripples cased by bad power supplies)

Mode [D]: This mode reads the file "MEMS.txt" at the SD/MMC card and streams the switching pattern to the analog switches, hence all eight output are switched corresponding the data on the SD/MMC card. If there is no SD/Card inserted, when switching to this mode, the software waits until a valid card is inserted. This can result in an infinite loop, which can be aborted by restarting the demonstrator, or inserting the card. Once inserted and validated, the software parses each line of the corresponding file. During the file execution the external interrupt number one is high (EXT_INT_1). During the data fetch process the external interrupt pin number four (EXT_INT_4) is high, while during the switching process it (EXT_INT_4) is low. If line number 65000 is reached, the loop stops executing and the file is closed.

Mode [E]: This mode streams eight semi-simultaneously fetched analog values to the SD/MMC card. The "first call" statement is executed once and initializes the internal analog digital converter. After this, the user can choose between three streaming options, by pressing KEY_1. First is the LCD output, where the analog value is displayed on the liquid crystal display with a visualization delay of 500 ms. The

second output is on the UART or USB port using a baudrate of 115.2 kBaut. The third output mode stores the fetched analog data on the SD/MMC card in the file “analog.txt”. Each conversation generates a new line with data in the file (appended data call).Since we implemented a FAT16 and FAT32 file system, the generated file can be read at any computer directly.

Mode [F]: This mode is an input test case, where KEY_1 and KEY_2 function can be tested with highlighting the LEDs.

B.3 Demonstrator

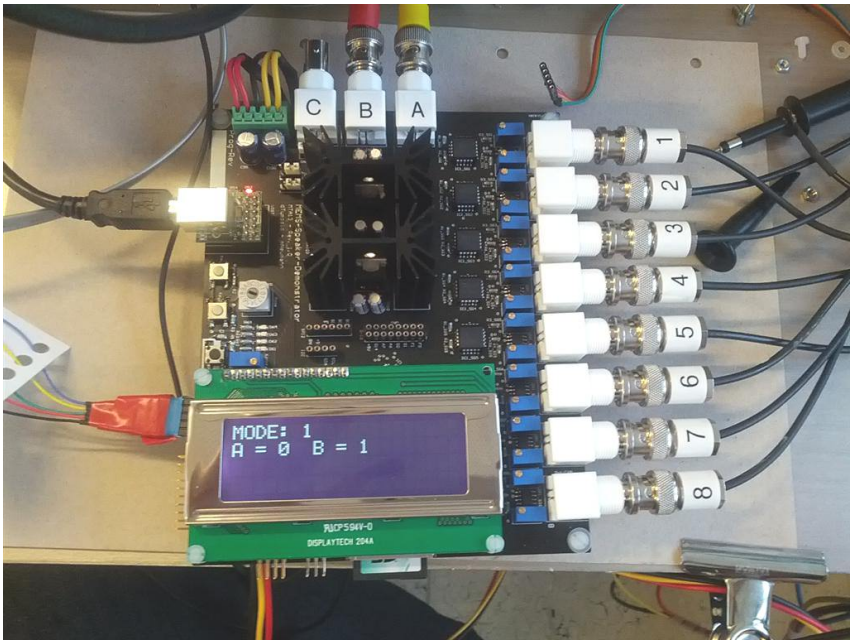

Figure B-9: Demonstrator fully assembled.

APPENDIX C

C BBP – Parameter Details

C.1 SiN4 Thickness Variation

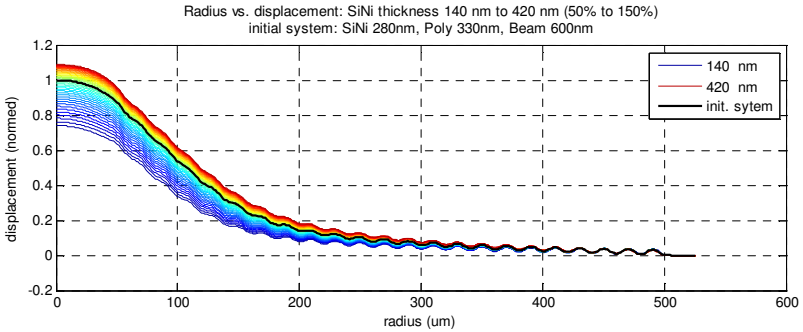

Figure C-1: Parameter sweep results of SiNi thickness versus static buckling shape over radius compared and normed to initial system. Parameter variation starts at 50% (140nm) and increased linearly up to 150% (420nm). No load added

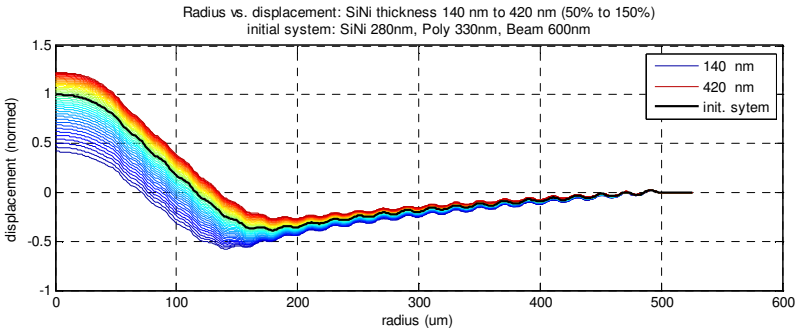

Figure C-2: Parameter sweep results of SiNi thickness versus static buckling shape over radius compared and normed to initial system. Parameter variation starts at 50% (140nm) and increased linearly up to 150% (420nm). Deformed shape is under constant homogeneous pressure load of 1 kPa.

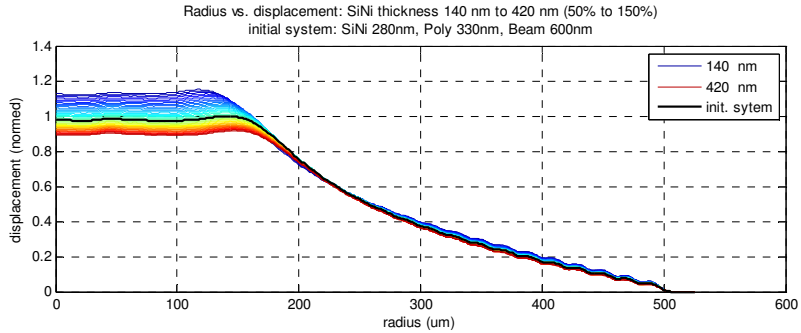

Figure C-3: Parameter sweep results of SiNi thickness versus static buckling shape over radius compared and normed to initial system. Parameter variation starts at 50% (140nm) and increased linearly up to 150% (420nm). Shape displays differential displacement between static deformation and loaded deformation.

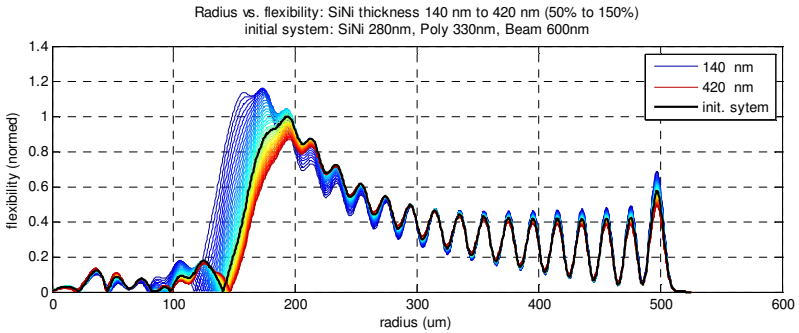

Figure C-4: Parameter sweep results of SiNi thickness versus static buckling shape over radius compared and normed to initial system. Parameter variation starts at 50% (140nm) and increased linearly up to 150% (420nm). Deformed shape displays flexibility over radius with salient point and corrugation rings.

C.2 Poly-Silicon Thickness Variation

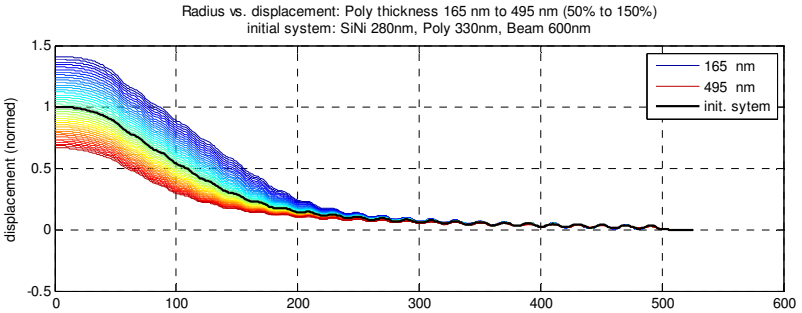

Figure C-5: Parameter sweep results of poly-silicon thickness versus static buckling shape over radius compared and normed to initial system. Parameter variation starts at 50% (165nm) and increased linearly up to 150% (495nm). No load added.

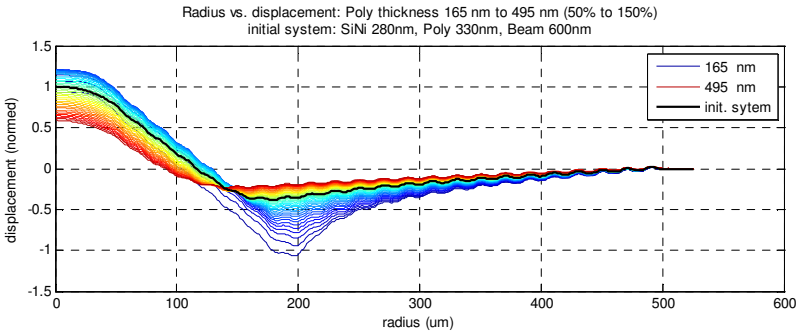

Figure C-6: Parameter sweep results of poly-silicon thickness versus static buckling shape over radius compared and normed to initial system. Parameter variation starts at 50% (165nm) and increased linearly up to 150% (495nm). Deformed shape is under constant homogeneous pressure load of 1 kPa.

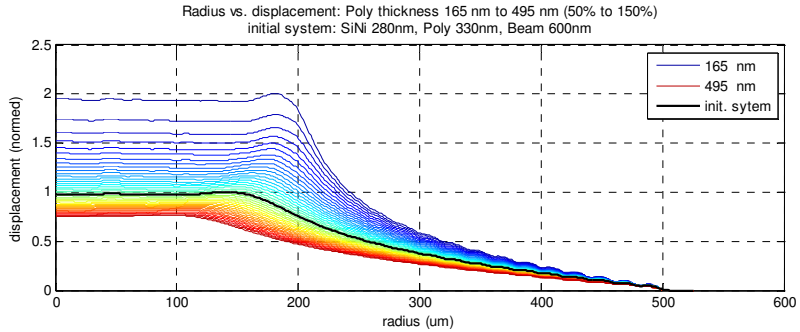

Figure C-7: Parameter sweep results of poly-silicon thickness versus static buckling shape over radius compared and normed to initial system. Parameter variation starts at 50% (165nm) and increased linearly up to 150% (495nm). Shape displays differential displacement between static deformation and loaded deformation.

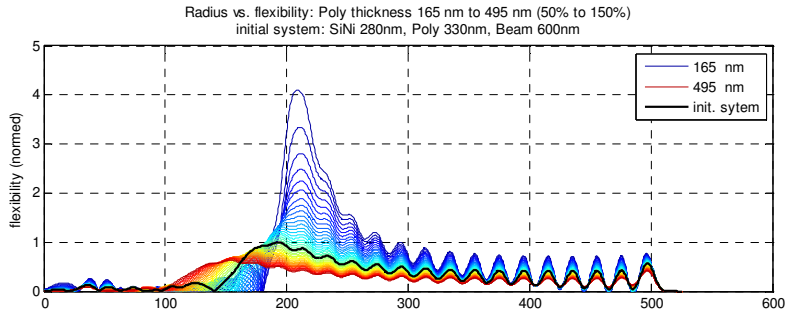

Figure C-8: Parameter sweep results of poly-silicon thickness versus static buckling shape over radius compared and normed to initial system. Parameter variation starts at 50% (165nm) and increased linearly up to 150% (495nm). Deformed shape displays flexibility over radius with salient point and corrugation rings.

C.3 Beam Height Variation

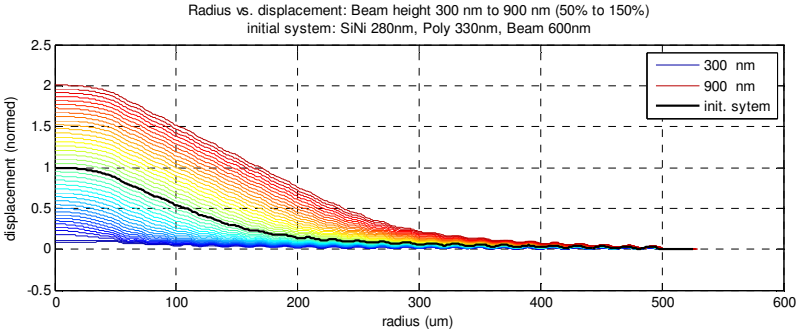

Figure C-9: Parameter sweep results of beam height versus static buckling shape over radius compared and normed to initial system. Parameter variation starts at 50% (300nm) and increased linearly up to 150% (900nm). No load added.

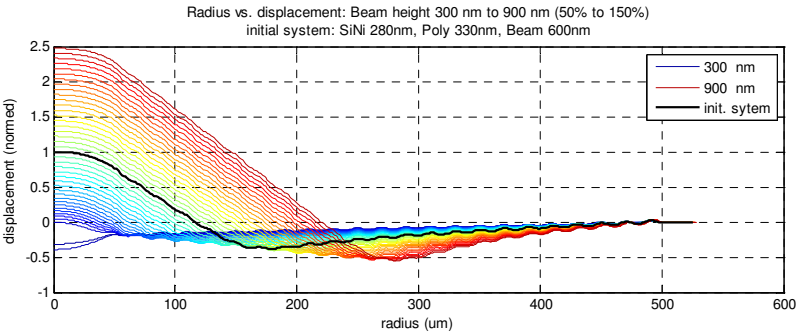

Figure C-10: Parameter sweep results of beam height versus static buckling shape over radius compared and normed to initial system. Parameter variation starts at 50% (300nm) and increased linearly up to 150% (900nm). Deformed shape is under constant homogeneous pressure load of 1 kPa.

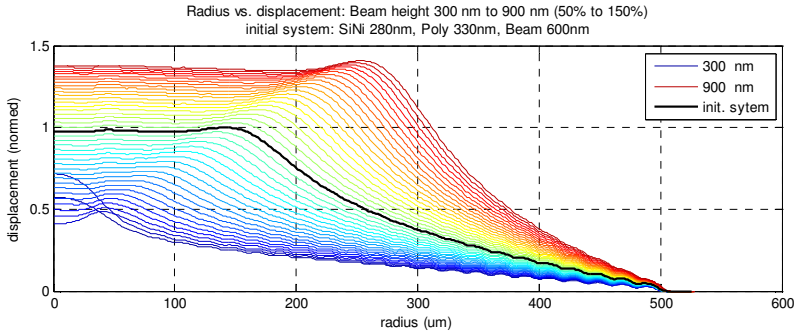

Figure C-11: Parameter sweep results of beam height versus static buckling shape over radius compared and normed to initial system. Parameter variation starts at 50% (300nm) and increased linearly up to 150% (900nm). Shape displays differential displacement between static deformation and loaded deformation.

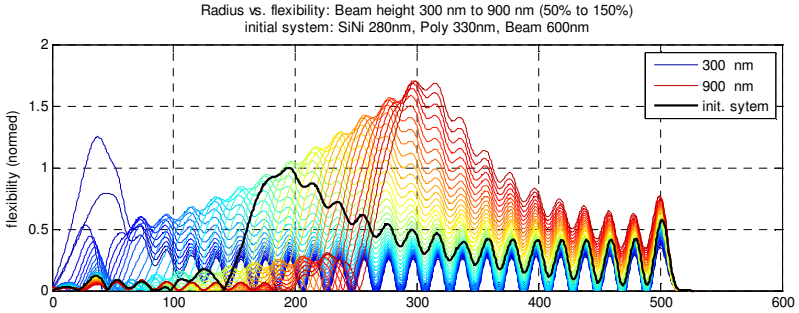

Figure C-12: Parameter sweep results of beam height versus static buckling shape over radius compared and normed to initial system. Parameter variation starts at 50% (300nm) and increased linearly up to 150% (900nm). Deformed shape displays flexibility over radius with salient point and corrugation rings

C.4 SiN4 Pre-Stress Variation

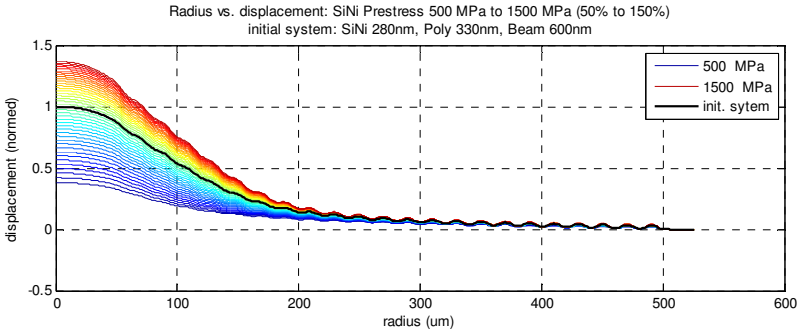

Figure C-13: Parameter sweep results of SiNi pre-stress versus static buckling shape over radius compared and normed to initial system. Parameter variation starts at 50% (500MPa) and increased linearly up to 150% (1500MPa). No load added.

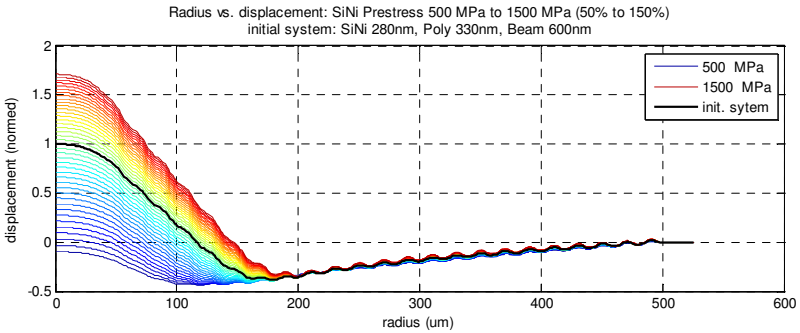

Figure C-14: Parameter sweep results of SiNi pre-stress versus static buckling shape over radius compared and normed to initial system. Parameter variation starts at 50% (500MPa) and increased linearly up to 150% (1500MPa). Deformed shape is under constant homogeneous pressure load of 1 kPa.

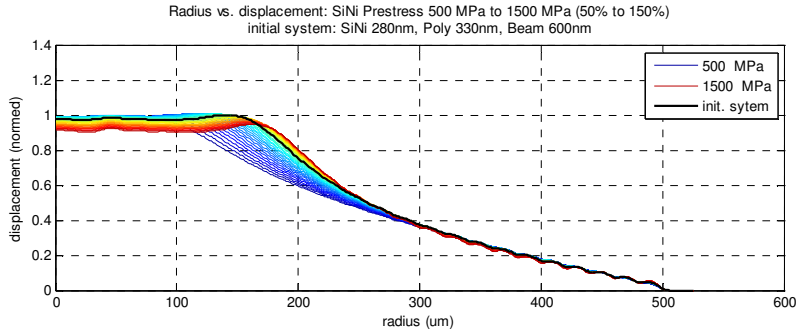

Figure C-15: Parameter sweep results of SiNi pre-stress versus static buckling shape over radius compared and normed to initial system. Parameter variation starts at 50% (500MPa) and increased linearly up to 150% (1500MPa). Shape displays differential displacement between static deformation and loaded deformation

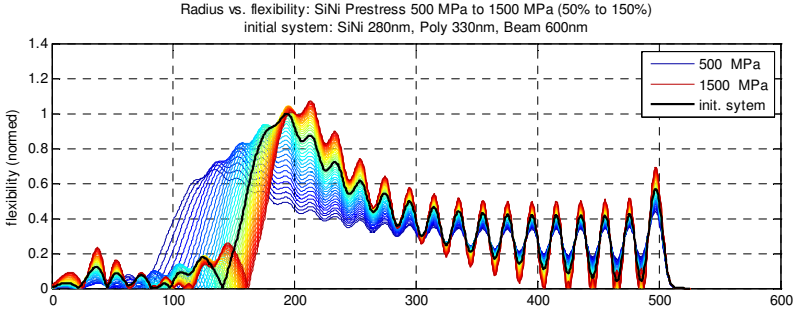

Figure C-16: Parameter sweep results of SiNi pre-stress versus static buckling shape over radius compared and normed to initial system. Parameter variation starts at 50% (500MPa) and increased linearly up to 150% (1500MPa). Deformed shape displays flexibility over radius with salient point and corrugation rings.

C.5 Poly-Silicon Thickness Variation

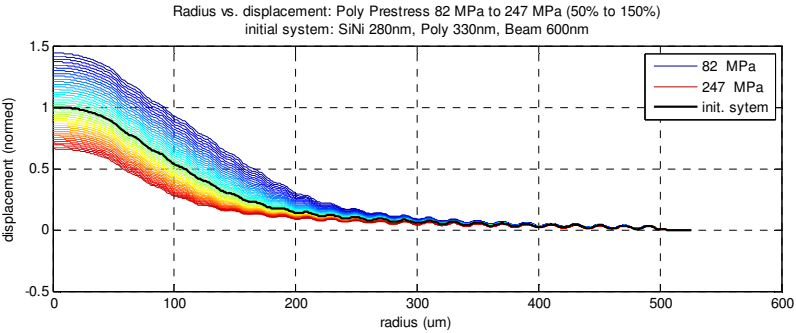

Figure C-17: Parameter sweep results of poly-silicon pre-stress versus static buckling shape over radius compared and normed to initial system. Parameter variation starts at 50% (82MPa) and increased linearly up to 150% (247MPa). No load added.

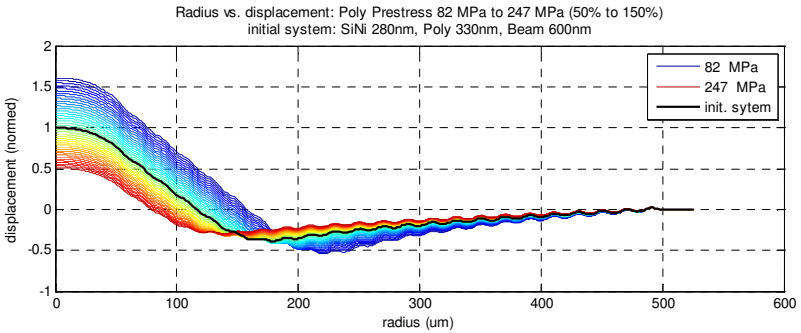

Figure C-18: Parameter sweep results of poly-silicon pre-stress versus static buckling shape over radius compared and normed to initial system. Parameter-variation starts at 50% (82MPa) and increased linearly up to 150% (247MPa). Deformed shape is under constant homogeneous pressure load of 1 kPa.

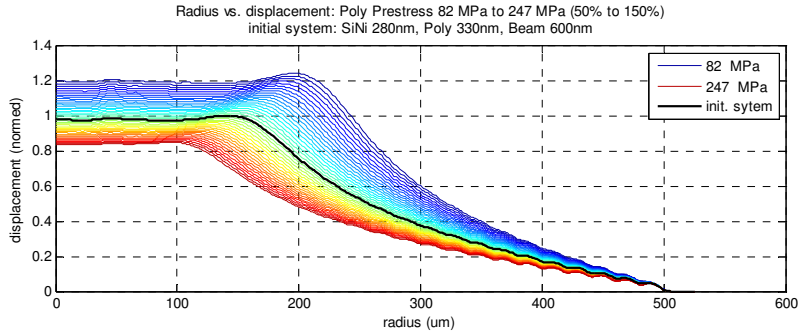

Figure C-19: Parameter sweep results of poly-silicon pre-stress versus static buckling shape over radius compared and normed to initial system. Parameter variation starts at 50% (82MPa) and increased linearly up to 150% (247MPa). Shape displays differential displacement between static deformation and loaded deformation.

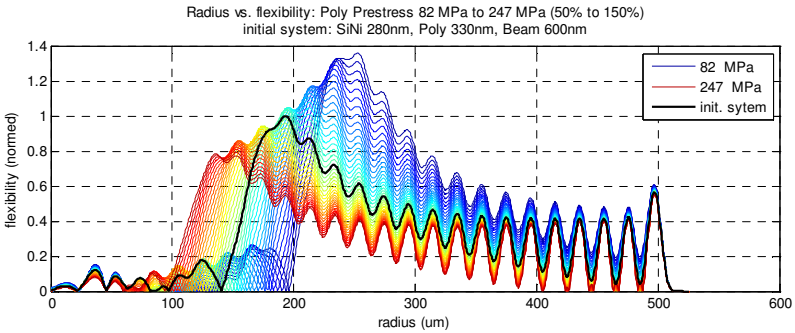

Figure C-20: Parameter sweep results of poly-silicon pre-stress versus static buckling shape over radius compared and normed to initial system. Parameter variation starts at 50% (82MPa) and increased linearly up to 150% (247MPa). Deformed shape displays flexibility over radius with salient point and corrugation rings.

APPENDIX D

D Numerical Integration with Gauss Legendre

As already mentioned in section 4.5.2, numerical integration is applied in many computing applications dealing with integrals

D.1 Solver with Gauss Legendre

The trapezoidal rule interpolates two points a and b of a function $f_{(x)}$ linearly. Both points are numerically weighted equal. The name results in the obtained area between these two points, a trapezoid. Hence, the numerical approximation of

$$F(x) = \int_a^b f(x)\,dx \tag{D.1}$$

complies with

$$F(x) = \int_a^b f(x)\,dx \;\approx\; \frac{h \cdot (f_a - f_b)}{2}. \tag{D.2}$$

An more accurate method is the Simpson rule, which uses three points with different weightings. Start and stop points are weighted equal as the trapezoidal with one, but the third point is weighted by four and aligned in center of a and b. The Simpson rule uses a polynomial function of second order to fit the original function $f(x)$, and is therefore

more accurate than the trapezoidal rule. Equation (D.3) describes the approximation function according to Simpson

$$F(x)=\int_a^b f(x)\,dx \;\approx\; \frac{h\cdot(f_a+4f_{(a-b)/2}+f_b)}{3}. \tag{D.3}$$

In Figure D-1 the difference between trapezoidal rule (left) and Simpson rule (right) is depicted, a polynomial function with order three was used as *f(x)*.

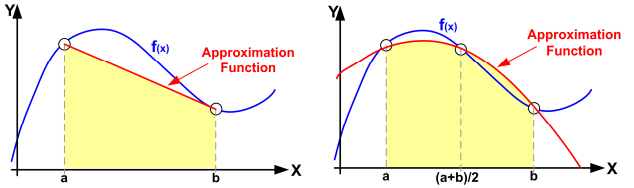

Figure D-1: Numerical integration with two points in trapezoidal rule (left) and three points in Simpson rule (right).

Simpson and trapezoidal rule need equal distances between the sampling points. The idea of Gaussian ansatz is to change the equal distances with optimal ones. With this modification the accuracy of approximated results can be improved on polynomial functions with the order of 2N-1, where N is the number of sampling points. To achieve an accurate result the sampling points have to correlate with the correct weighting factors as described in [134]. Hence, if the function $f_{(x)}$ is substituted by a polynomial function $p_{(x)}$ and a weighting function $\omega_{(x)}$, the result corresponds to the original function (exact computation).

$$F(x)=\int_a^b f(x)\,dx \;=\int_a^b \omega(x)\,p(x)\,dx\,. \tag{D.4}$$

As a result, the overall accuracy is limited by the accuracy of the weighting factor $\omega_{(x)}$, which has to be positive and integrable to fulfill Gaussian integral theorem. Also the polynomial function $p_{(x)}$ must be continuous on computational domain to fulfill the criteria.
The big advantage of Gaussian integral theorem is the accuracy and computational speed in comparison to Simpson or trapezoidal rule. Therefore this ansatz is frequently used in complex analysis of functions. The integral is computed on the domain [-1,+1] which is

called Gauss Legendre and used in FEM also on the mapped reference element [46]. In Figure D-2 the on dimensional case with two sampling points can be seen. In this case N is two, for two sampling points, hence the ideal computational points are aligned at $\pm\sqrt{(1/3)}$ [86].

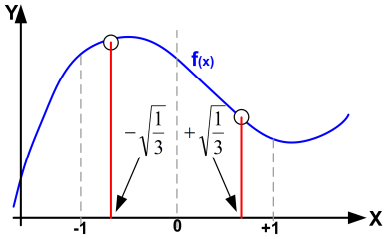

Figure D-2: Two sampling points in one dimensional case for Gauss Legendre.

To get a more generalized form of the Gauss Legendre theorem, the computational domain has to be extended from [-1,+1] to [a,b]. Therefore, a transformation with a scaling factor and an offset correction have to be introduced

Scaling factor: $$\frac{b-a}{2} \tag{D.5}$$

Offset correction: $$\frac{a+b}{2} \tag{D.6}$$

By applying (D.5) and (D.6) in (D.4), we get

$$\int_a^b f(x)\,dx = \frac{b-a}{2}\int_{-1}^{+1} f\left(\frac{b-a}{2}x+\frac{a+b}{2}\right)dx\,. \tag{D.7}$$

In this sense for Gaussian approximation the sampling points x_i and the weighting factors ω_i of (D.4) have to be applied, hence the one dimensional case corresponds to

$$\int_a^b f(x)\,dx \approx \frac{b-a}{2}\sum_{i=1}^{n} \omega_i\, f\left(\frac{b-a}{2}x_i+\frac{a+b}{2}\right). \tag{D.8}$$

For wave field calculations, the surface of an active speaker cell is important. Therefore the Gauss Legendre is extended to the two dimensional case by,

$$F(x,y)=\int_{y_a}^{y_b}\int_{x_a}^{x_b} f_{(x,y)}\,dxdy \;\approx$$
$$\frac{x_b-x_a}{2}\cdot\frac{y_b-y_a}{2}\sum_{j=1}^{n}\sum_{i=1}^{n}\;\omega_i\omega_j\cdot f\left(\frac{x_b-x_a}{2}x_i+\frac{x_a+x_b}{2},\frac{y_b-y_a}{2}y_j+\frac{y_a+y_b}{2}\right). \tag{D.9}$$

Figure D-3 depicts the original Gauss Legendre computational domain with the sampling points located on the surface for N=2.

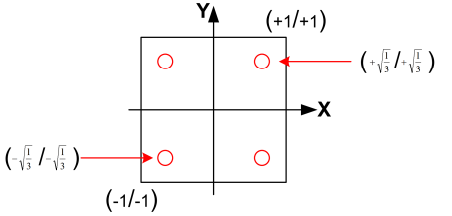

Figure D-3: Four sampling points in two dimensional case for Gauss Legendre in computational domain [-1/+1].

The result must be scaled, therefore it has to be divided by the surface of the computational domain (four) to achieve the correct result.

Bibliography

[1] C.-M. Lee and S.-M. Hwang, "Development of advanced rectangular microspeakers used for wide liquid-crystal display mobile phones," *Journal of Applied Physics,* vol. 109, pp. 07E504-07E504-3, 2011.

[2] I. Shahosseini*, et al.*, "Optimization and microfabrication of high performance silicon-based MEMS microspeaker," in *Sensors, 2013 IEEE*, 2013, pp. 1530-1542.

[3] M. R. Bai*, et al.*, "Optimization of microspeaker diaphragm pattern using combined finite element–lumped parameter models," *Magnetics, IEEE Transactions on,* vol. 44, pp. 2049-2057, 2008.

[4] I. Shahosseini*, et al.*, "Towards high fidelity high efficiency MEMS microspeakers," in *Sensors, 2010 IEEE*, 2010, pp. 2426-2430.

[5] Yuval Cohen, *et al.*, "Apperatus and methods for generating pressure waves," US2010/002900 A1, 2010.

[6] Yuval Cohen, *et al.*, "Digital Speaker Apparatus," US 2010/0316242 A1, 2010.

[7] Yuval Cohen, *et al.*, "Volume and tone control in direct digital speakers," US 2010/0008521 A1, 2010.

[8] C.-M. Lee and S.-M. Hwang, "Optimization of SPL and THD performance of microspeakers considering coupling effects," *Magnetics, IEEE Transactions on,* vol. 47, pp. 934-937, 2011.

[9] Yuval Cohen, *et al.*, "Direct digital speaker apparatus having a desired directivity pattern," US 2010/0166242 A1, 2010.

[10] Yuval Cohen, *et al.*, "Digital speaker apparatus," US 2010/0316242 A1, 2010.

[11] Xu Zhu and P. A. Ciferno, "Ultrathin form factor MEMS microphones and microspeaker," US 6,936,524 B2, 2005.

[12] Kaigham J. Gabriel and X. Zhu, "Process for forming and acoustically connecting structures on substrate," US 7,049,051 B2, 2006.

[13] Brett M. Diamond, *et al.*, "Proof-mass with supporting structure on integrated circuit-MEMS platform," US 7,640,805 B2, 2010.

[14] Brett M. Diamond and Z. Matthew A, "Monolithic MEMS and integrated circuit device having a barrier and method of fabricating the same," US 7,863,714 B2, 2011.

[15] A. Dehé, "Micro electrical mechanical system with bending deflection of backplate structure," Neubiberg (DE) Patent US 20130062710A1, 2013.

[16] H. Kim, *et al.*, "Bi-directional electrostatic microspeaker with two large-deflection flexible membranes actuated by single/dual electrodes," in *Sensors, 2005 IEEE*, 2005, p. 4 pp.

[17] Yuval Cohen, *et al.*, "Electrostatic Parallel Plate Actuators Who's Moving Elements Are Driven Only By Electrostatic Force and Methods Usefull in Conjunction Therewith," US20130076275 A1, 2011.

[18] Markus Lutz, *et al.*, "Methods for trapping charge in a microelectromechanical system and microelectromechanical system employing same," US 7,824,943 B2, 2010.

[19] R. C. Roberts, *et al.*, "Electrostatically driven touch-mode poly-SiC microspeaker," in *Sensors, 2007 IEEE*, 2007, pp. 284-287.

[20] John J. Neumann Jr. and K. J. Gabriel, "CMOS-MEMS mebrane for audio-frequency acoustic actuation," in *Micro Electro Mechanical Systems, 2001. MEMS 2001. The 14th IEEE International Conference*, Interlaken , Switzerland 2001

[21] D. J. M. Robinson, "The human auditory system," ed, 2010.

[22] P. Rangsten, *et al.*, "Electrostatically excited diaphragm driven as a loudspeaker," *Sensors and Actuators A: Physical,* vol. 52, pp. 211-215, 1996.

[23] T. D. Kite, *et al.*, "Parametric array in air: distortion reduction by preprocessing," *Proc. 16th int. cong. acoust,* vol. 2, pp. 1091-1092, 1998.

[24] W. Liu, *et al.*, "Audio distortion correction for a parametric reproduction system," US Patent 8.275.137, 2012.

[25] B. M. Diamond, "Digital Sound Reconstruction Using Arrays of CMOS-MEMS Microspeakers," Master of Scienece, Electrical & Computer Engineering, Carnergie Mellon University, 2002.

[26] B. M. Diamond, *et al.*, "Digital sound reconstruction using arrays of CMOS-MEMS microspeakers," in *TRANSDUCERS, Solid-State Sensors, Actuators and Microsystems, 12th International Conference on, 2003*, 2003, pp. 238-241.

[27] Kaigham J. Gabriel, *et al.*, "Multiple membrane structure and method of manufacture," US 2003/0210799 A1, 2003.

[28] Kaigham J. Gabriel, *et al.*, "Method and apparatus for reconstruction of soundwaves from digital signals," US 7,089,069 B2, 2006.

[29] Kaigham J. Gabriel and X. Zhu, "Multi-metal layer MEMS structure and process for making the same," US 6,943,448 B2, 2005.

[30] H. J. Kim, *et al.*, "High performance piezoelectric microspeakers and thin speaker array system," *ETRI journal,* vol. 31, 2009.

[31] S. C. Ko, *et al.*, "Micromachined piezoelectric membrane acoustic device," *Sensors and Actuators A: Physical,* vol. 103, pp. 130-134, 2003.

[32] S. Yi, *et al.*, "Performance of packaged piezoelectric microspeakers depending on the material properties," in *Micro Electro Mechanical Systems, 2009. MEMS 2009. IEEE 22nd International Conference on*, 2009, pp. 765-768.

[33] S. S. Lee and R. M. White, "Piezoelectric cantilever voltage-to-frequency converter," *Sensors and Actuators A: Physical,* vol. 71, pp. 153-157, 1998.

[34] H. Cho, *et al.*, "Dependence of material properties on piezoelectric microspeakers with AlN thin film," in *Nano/Micro Engineered and Molecular Systems, 2008. NEMS 2008. 3rd IEEE International Conference on*, 2008, pp. 637-640.

[35] Wayne A. Loeb, *et al.*, "MEMS digital-to-acoustic transducer with error cancellation," US 6,829,131 B1, 2004.

[36] M.-C. Cheng, *et al.*, "A silicon microspeaker for hearing instruments," *Journal of Micromechanics and Microengineering,* vol. 14, p. 859, 2004.

[37] M. Harradine, *et al.*, "A micro-machined loudspeaker for the hearing impaired," in *Solid State Sensors and Actuators, 1997. TRANSDUCERS'97 Chicago., 1997 International Conference on*, 1997, pp. 429-432.

[38] S.-S. Je, *et al.*, "A compact and low-cost MEMS loudspeaker for digital hearing aids," *Biomedical Circuits and Systems, IEEE Transactions on,* vol. 3, pp. 348-358, 2009.

[39] J. Rehder, *et al.*, "Balanced membrane micromachined loudspeaker for hearing instrument application," *Journal of Micromechanics and Microengineering,* vol. 11, p. 334, 2001.

[40] C. Glacer, *et al.*, "Reversible acoustical transducers in MEMS technology," in *Design, Test, Integration and Packaging of MEMS/MOEMS (DTIP), 2013 Symposium on*, 2013, pp. 1-4.

[41] A. Sorger, "Simulation von Dämpfungsmechanismen in komplexen Mikrostrukturen," Dipl.-Ing., Fakultät für Elektrotechnik und Informationstechnik, TU Chemnitz, Chemnitz, 2009.

[42] D. Adams, *The Hitch Hikers Guide to the Galaxy.* London: Pan Books LTD, 1979.

[43] R. Beavers, *et al.*, "Simple Electrostatic Transducers for High - Frequency Sounds," *The Journal of the Acoustical Society of America,* vol. 48, p. 126, 1970.

[44] J. A. Hossack, "Medical diagnostic ultrasound system and method for harmonic imaging with an electrostatic transducer," Mountain View (CA) Patent US 6.461.299 B1, 2002.

[45] M. Kaltenbacher, "Simulationsbasierte Entwicklung von Sensoren," *tm-Technisches Messen,* vol. 79, pp. 30-36, 2012.

[46] M. Kaltenbacher, *Numerical Simulation of Mechatronic Sensors and Actuators*, 2nd ed. Berlin Springer 2007.

[47] M. Füldner, "Modellierung und Herstellung kapazitiver Mikrofone in BiCMOS-Technologie," PhD, Universität Erlangen-Nürnberg, München, 2004.

[48] D. Tumpold, *Modeling Methods for CMOS MEMS Speaker using Finite Element Method* vol. 1. Saarbrücken: AV Akademiker Verlag, 2013.

[49] David Tumpold, *et al.*, "Modeling Methods of MEMS Micro-Speaker with Electrostatic Working Principle," presented at the SPIE Microtechnologies, Grenoble, 2013.

[50] David Tumpold, *et al.*, "Modeling of an electrostatically actuated microelectromechanical (MEMS) speaker system," presented at the Conference Proceedings PRIME2013 9th Conference on Ph. D. Research in Microelectronics and Electronics, Villach, 2013.

[51] David Tumpold and M. Kaltenbacher, "Modeling Methods of MEMS Speaker Devices with Electrostatic Driving Principle," presented at the ANSYS Conference & 31. CADFEM Users, Mannheim Germany, 2013.

[52] Becker Wilfried and G. Dietmar, *Mechanik elastischer Körper und Strukturen* vol. 1. Berlin: Springer, 2002.

[53] R. C. Hibbeler, *Technische Mechanik 2. Festigkeitslehre* vol. 5. Louisiana: Pearson Studium, 2005.

[54] H. Parkus, *Mechanik der festen Körper* vol. 2. Wien NewYork: Springer, 2009 (1966).

[55] M. Ohring, *Materials science of thin films*: Academic press, 2001.

[56] H. Czichos*, et al.*, *Springer handbook of materials measurement methods*: Springer, 2006.

[57] G. Irmer, "Skript zur Vorlesung: Theoretische Physik, Kontinuumsmechanik," in *Kontinuumsmechanik*, ed. TU - Freiberg, 2007.

[58] K. J. Bathe, *Finite Elemente Methoden* vol. 1. Berlin: Springer, 1990.

[59] Johannes Wissmann and K.-D. Sarnes, *Finite Elemente in der Strukturmechanik*. Berlin: Springer, 2006.

[60] F. Ihlenburg, "Nichtlineare FEM," in *HAW Hamburg, Dept. M+P*, ed. Hamburg, 2011.

[61] ANSYS, "Modeling and Meshing Guide," vol. 12.0, ed. Canonsburg,PA, 2009, p. 278.

[62] J. T. Metrisin, "Guidelines for Obtaining Contact Convergence," in *ANSYS Conference*, ed. Florida, 2008.

[63] ANSYS, "Introduction to Contact," in *Mechanical Structural Nonlinearities*, ed. Canonsburg,PA, 2010, p. 36.

[64] ANSYS, "Advanced Contact," in *Mechanical Structural Nonlinearities*, ed. Canonsburg,PA, 2010, p. 38.

[65] C. Gebhardt, *Praxisbuch FEM mit ANSYS Workbench*. Muenchen: Hanser, 2011.

[66] S. Imaoka, "Sheldon's ANSYS Tips and Tricks: Understanding Lagrange Multipliers," 2001.

[67] S. Hüeber and B. I. Wohlmuth, "A primal–dual active set strategy for non-linear multibody contact problems," *Computer Methods in Applied Mechanics and Engineering,* vol. 194, pp. 3147-3166, 2005.

[68] S. Hüeber and B. I. Wohlmuth, *Mortar methods for contact problems*: Springer, 2006.

[69] T. A. Laursen, *Computational Contact and Impact Mechanics* vol. 1. Berlin: Springer, 2002.

[70] ANSYS, "ANSYS Structural Analysis Guide," in *Release 9*, ed, 2004.

[71] ANSYS, "Theory Reference for the Mechanical APDL and Mechanical Applications," vol. 12.1, ed. Canonsburg,PA, 2009, p. 1228.

[72] M. Jung and U. Langer, *Methode der finiten Elemente für Ingenieure* vol. 2: Springer Vieweg, 2001.

[73] Robert M. Ferencz and T. J. R. Hughes, *Handbook of Numerical Analysis, Iterative Finite Element Solutions in Nonlinear Solid Mechanics* vol. 6. North-Holland, 1998.

[74] G. Kress, "Strukturanalyse mit FEM," in *ETH Zürich*, ed. Zürich, 2004, p. 138.

[75] G. A. Holzapfel, *Nonlinear Solid Mechanics: A Continuum Approach for Engineering*, 1 ed. vol. 1: Wiley, 2000.

[76] T. Daxner and F. G. Rammerstorfer, "Nichtlineare Finite Elemente Methode," ed. Wien: ILSB, 2012, p. 212.

[77] G. Lehner, *Elektromagnetische Feldtheorie: für Ingenieure und Physiker* vol. 4. Berlin: Springer, 2003.

[78] J. Stock, "Gabriel Lippman dn the capillary electrometer," *Bull. hist. Chem.,* vol. 29, p. 4, 2004.

[79] J.-P. Meyn, *Grundlegende Experimentiertechnik im Physikunterricht* vol. 2. Oldenbourg Oldenbourg Wissenschaftsverlag, 2013.

[80] C. Ostermaier, "Neue Materialien in der CMOS Technologie," Bachalor, Institut für Festkörperelektronik, Technische Universität Wien, 2004.

[81] ANSYS, "Element Reference," vol. 12.0, ed. Canonsburg,PA, 2009, p. 1690.

[82] D. C. Giancoli, *Physik: Lehr- und Übungsbuch (Pearson Studium - Physik)* vol. 3. Slovak Republic: Pearson, 2009.

[83] D. A. Bohn, "Environmental Effects on the Speed of Sound," *J. Audio Eng. Soc.,* vol. 36, 1988.

[84] Gerhard Müller and M. Möser, *Taschenbuch der Technischen Akustik*. Berlin Heidelberg: Springer, 2004.

[85] Richard Courant and D. Hilbert, *Methoden der mathematischen Physik* vol. 2. Berlin: Springer, 2003.

[86] Ilja N. Bronstein*, et al.*, *Taschenbuch der Mathematik* vol. 5: Harri, 2000.

[87] K. Ehrenfried, "Skript zur Vorlesung: Ströemungsakustik I," in *Strömungsakustik*, ed. Technische Universität Berli, 2003.

[88] M. Suri*, et al.*, "Locking effects in the finite element approximation of plate models," *Mathematics of computation,* vol. 64, pp. 461-482, 1995.

[89] S. Triebenbacher, "Nichtkonforme Gitter für die numerische Simulation von Aeroakustik- und Vibroakustikproblemen," PhD, Alpen-Adria-Universität Klagenfurt, Klagenfurt, 2012.

[90] S. Triebenbacher*, et al.*, "Applications of the Mortar Finite Element Method in Vibroacoustics and Flow Induced Noise Computations," *Acta Acustica united with Acustica,* vol. 96, pp. 536-553, 2010.

[91] D. Dreyer*, et al.*, "Effectiveness and robustness of omproved infinite elements for exterior acoustics," *ELSEVIER Computer Methods in Applied Mechanics and Engineering,* vol. 195, pp. 3591-3607, 1 June 2006 2005.

[92] Marcus J. Grote and I. Sim, "Local nonreflecting boundary condition for time-dependent multiple scattering," *Journal of Computational Physics,* vol. 230, pp. 3135-3154, 2011.

[93] Andreas Hüppe and M. Kaltenbacher, "Spectral Finite Elements for Computational Aeroacoustics using Acoustic Perturbation Equation," *Journal of Computational Acoustics,* vol. 20, p. 13, 2012.

[94] J.-P. Berenger, "A Perfectly Matched Layer for the Absorption of Electromagnetic Waves," *Journal of Computational Physics,* vol. 114, pp. 185-200, 1994.

[95] Barbara Kaltenbacher*, et al.*, "A modified and stable version of a perfectly matched layer technique for the 3-d second order

wave equation in time domain with an application to aeroacoustics," *Journal of Computational Physics,* vol. 235, pp. 407-422, 15 Februrary 2013 2013.

[96] G. Reisinger, "Einsatz von stereophonen Aufnahmetechniken für die räumliche Übertragung ausgedehnter Schallquellen mit Hilfe der Wellenfeldsynthese," Dipl.-Ing., Medien Studiengang Ton- und Bildtechnik, university of Applied Scienece Düsseldor, Düsseldorf), 2003.

[97] M. Reisinger, "Neue Konzepte der Tondarstellung bei Wiedergabe mittels Wellenfeldsynthese," Dipl.-Ing., Medien Studiengang Ton- und Bildtechnik, University of Applied Science Düsseldorf, Düsseldorf, 2002.

[98] J. Fels, "From Children to Adults: How Binaural Cues and Ear Canal Impedances Grow," PhD, Elektrotechnik und Informationstechnik, Rheinisch-Westfälische Technische Hochschule, Aachen, 2008.

[99] Christoph Glacer*, et al.*, "Capacitive out of plane large stroke MEMSstructure," presented at the PRIME, Villach, 2013.

[100] John Brueckner*, et al.*, "An integrated experimental and theoretical approach to evaluate Si strengh dependent on the processing history," *ASME,* vol. 10, p. 7, 2009.

[101] D. Tumpold, "MEMS based speaker system," Master Thesis, Applied Mechatronics, Alpen Adria Universität, Klagenfurt, 2011.

[102] C. Glacer, "Reversible akustische Wandler in MEMS Technologie," Dipl.-Ing., Theoretische Elektrotechnik und Mikroelektronik (ITEM), University Bremen, Bremen, 2011.

[103] C.O'Mahony, *et al.*, "Low-voltage micromechanical test structure for measurement of residual charge in dielectrics," *eElectronics Letters,* vol. 41, p. 2, 2005.

[104] K Das and R. C. Batra, "Pull-in and snap-through instabilites in transient deformation of microelectromechanical systems," *Journal of Micromechanics and Mcroengineering,* vol. 19, 05 Feb 2009 2009.

[105] Slava Krylov, *et al.*, "The pull-in behavior of electrostatically actuated bistable microstructures," *Journal of Micromechanics and Microengineering,* vol. 18, p. 20, 2008.

[106] Wen-Ming Zhang, *et al.*, "Stability, Nonlinearity and Reliability of Electrostatically Actuated MEMS Devices," *Sensors,* vol. 7, pp. 760-796, 31 May 2007 2007.

[107] M. Möser, *Technische Akustik*: Springer, 2009.

[108] Fotios Kontomichos, *et al.* (2011). *Alternative Encoding Techniques for Digital Loudspeaker Arrays*

[109] S. Merchel and S. Groth, "Analysis and Implementation of a Stereophonic Play Back System for Adjusting the “Sweet Spot” to the Listener’s Position," in *Audio Engineering Society Convention 126*, 2009.

[110] W. Fuchs. (2005), Eine Frage der Schweere. *SAC Logandrive SL3 Vol, 1.*

[111] P. Seibt, *Algorithmic information theory: mathematics of digital information processing* vol. 1. Berlin Heidelberg: Springer, 2006.

[112] Brett M. Diamond, *et al.*, "Digital sound reconstruction using arrays of CMOS-MEMS microspeakers," in *Micro Electro*

Mechanical Systems, 2002. The Fifteenth IEEE International Conference, Las Vegas, NV , USA 2002.

[113] D. C. v. Grünigen, *Digitale Signalverarbeitung* vol. 3. Leipzig: Carl Hanser, 2004.

[114] W. D. Keidel, *Kurzgefasstes Lehrbuch Der Physiologie* vol. 2. Stuttgart: Georg-Thieme Verlag, 1970.

[115] H. O. Associates. (2013, 16.12.2013). *Ears, Hearing & Balance Disorders.* Available: http://www.hunterdonent.com/ears_hearing_balance

[116] J. Ash and L. Potter, "Sensor network localization via received signal strength measurements with directional antennas," in *Proceedings of the 2004 Allerton Conference on Communication, Control, and Computing*, 2004, pp. 1861-1870.

[117] DIN, "Akustik - Simulatoren des menschlichen Kopfes und Ohres," in *Teil 5: 2ccm Kuppler zur Messung von mittels Ohreinsätzen angekoppelten Hörgeräten und Ohrhörern* vol. DIN EN 60318-5, ed. Berlin: DIN Deutsches Institut für Normung e.V., 2009, p. 16.

[118] DIN, "Occluded-ear simulator for the measurement of earphones coupled to the ear by ear inserts," in *IEC 60711* vol. IEC 60711, ed: International Electrotechnical Commission, January 1981.

[119] R. Guski. (1996, 22.02 Time: 12:00). *Wahrnehmen* Available: http://eco.psy.ruhr-uni-bochum.de/ecopsy/download/Guski-Lehrbuch/Kap_4_2.html

[120] U. Wuppertal. (2012, 15.02 Time: 18:00). *Ansteugende Frequenzabstände.* Available: http://www.dasp.uni-wuppertal.de/ars_auditus/psychoak/psych81.htm

[121] U. Reichel, "Perzeptive Phonetik," LMU München, München9.Juli.2008 2008.

[122] Oari. (2004, 15.02 Time: 12:00). *Cochlea*. Available: http://commons.wikimedia.org

[123] G. Friedrich and W. Biegenzahn, *Phoniatrie, Einführung in die medizinischen, psychologischen und linguistischen Grundlagen von Stimme und Sprache*. Bern Göttingen Toronto Seatle: Hans Huber, 1995.

[124] R. Carter, *Das Gehirn: Anatomie, Sinneswahrnehmung, Gedächtnis, Bewusstsein, Störungen*. München: Dorling Kindersley Verlag, 2010.

[125] M. C. Liberman*, et al.*, "Prestin is required for electromotility of the outer hair cell and for the cochlear amplifier," *Nature,* vol. 419, pp. 300-304, 2002.

[126] R. Greisbach, "Grundlagen der Phonetik II," in *JWG-Universität* ed. Frankfurt am Main, 2005.

[127] E. Z. Hugo Fastl, *Psychoacoustics, Facts and Models*. Berlin: Springer, 2007.

[128] A. M. Mayer, "Researches in Acoustics," *London, Edinburgh and Dublin Philosophical Magazine,* vol. 37, pp. 259–288, 1984.

[129] E. Zwicker, "Subdivision of the Audible Frequency Range into Critcal Bands (Frequenzgruppen)," *The Journal of the Acoustical Siciety of America,* vol. 33, 1960.

[130] J. Hassall and K. Zaveri, *Acoustic noise measurements*: Brüel & Kjaer Naerum, 1979.

[131] T. Z. Eberhard Zwicker, "Audio Engineering and Psychoacoustics: Matching Signals to the Final Receiver, the

Human Auditory System," *J. Audio Eng. Soc.,* vol. 39, pp. 115--126, 1991.

[132] D. J. M. Robinson and M. J. Hawksford, "Time-Domain Auditory Model for the Assessment of High-Quality Coded Audio," *J. Audio Eng. Soc.,* 1999.

[133] J.Blauert, "Akustik 2," in *Vorlesungsscript* ed. Ruhr-Universität Bochum, 2005.

[134] Gauß-Quadratur. (15.12.2010). *http://www.exp.univie.ac.at/sc/integration/integration.html*.